Copyright

by

Kueifu Lai

2018

The Dissertation Committee for Kueifu Lai Certifies that this is the approved version of the following dissertation:

Surface Wave Manipulation with Polar Dielectric Thin Films and Topological Photonic System

Committee:

Chih-Kang Shih, Supervisor

Gennady Shvets, Co-Supervisor

Ernst-Ludwig Florin

Gregory Fiete

Mikhail Belkin

Surface Wave Manipulation with Polar Dielectric Thin Films and Topological Photonic System

by

Kueifu Lai

Dissertation

Presented to the Faculty of the Graduate School of
The University of Texas at Austin
in Partial Fulfillment
of the Requirements
for the Degree of

Doctor of Philosophy

The University of Texas at Austin
May 2018

Dedicated to my family.

Acknowledgements

First and foremost, I would like to sincerely thank Prof. Gennady Shvets. This dissertation could not be completed without his guidance and support for the challenging research works. I would to thank Prof. Chih-Kang Shih for being my supervisor and helping me through the graduation process. Thanks to my thesis committee for feedback and support. Thanks to Prof. Ernst-Ludwig Florin for kindly serving as my committee member in both qualifier and defense. Thanks to Prof. Gregory Fiete for providing helpful discussions. Thanks to Prof. Mikhail Belkin for offering generous support.

Thanks to Dr. Jongwon Lee and Nishant Nookala in Belkin' group in ECE department. Thanks to Prof. Steven Anlage and Xiao Bo in University of Maryland. Thanks to Prof. Baile Zhang and Dr. Fei Gao in Nanyang Technological University in Singapore. Thanks to Prof. Pierto Musucemi and Nicholas Sudar in University of California, Los Angeles. Thanks to Gabriel Ferro in University Claude Bernard Lyon I.Thanks to all staffs at Accelerator Test Facility in Brookhaven National Laboratory and Argonne Wakefield Accelerator facility in Argonne National Laboratory for their generous offering of state-of-art engineering support.

I would like to forward my gratitude to group members under meat-sizzling hot sun in Austin. Thanks to Simeon Trendafilov for helping me learning COMSOL and his placid upholding. Thanks to Vladimir Khudik for his energetic discussion. Thanks to Alexander Khanikaev for being always supportive and welcoming. Thanks to Kamil Boratay Alici for training me on instruments. Thanks to Zhiyuan Fan for helping me with numerical simulation and sharing in-depth opinions. Thanks to Shourya Dutta Gupta for his vibrant and contagious style of doing research. Thanks to Feng Lu for showing me the long-

forgotten knowledge to use AFM. Thanks to Burton Neuner for providing invaluable help even after his graduation. Thanks to Nima Dabidian, Nihal Arju, and David Purtseladze for their fond companion in PMA (RLM). Thanks to Tzuhsuan Ma for his insightful discussion and being an amazing colleague. Thanks to Glen Kelp for sharing non-physics experience and being an awesome roommate for a year. Thanks to Xi Zhang for beneficial advices toward as well as after the graduation. Thanks to Yang Yu, Tianhong Wang, Panpan Ruan, Tao Wang, Chun-Ju Yang who arrived later but become invaluable estate of the group.

I would like to also express my appreciation to group members in bone-chilling cold winter in Ithaca. Thanks to Maxim Shcherbakov for bringing help and old memory back in NTU. Thanks to Ben Hopkins for every warm invite to happy hour in Big Red Barn. Thanks to Steven He Huang for sharing his experience of post-graduation. Thanks to Ran Gladstone, Minwoo Jung, Alice Huang, Yue Yu, and Yandong Li for joining even when the group is restarting from ground-zero. Thanks to undergraduate researchers, Yuchen Han, Dalila Robledo de Basabe, Robert Delgado, Junlan Lu, Nicholas DiNapoli, Joy Li, and Fengyu Liu, for their arduous effort and determined sailing to academia.

There are many friends who I must thank while wandering on the UT campus. Ping-Chun Li for his hopeless support, Wei-Jin Zheng for his euphemistic rejection, Ren-Tsung Wu for the cross-platform notices, Chi-Chun Fang for being a considering roommate.

Finally, I would like to sincerely thank my family though my appreciation is beyond the words. I am deeply indebted to my parents who endure my wayward decisions with selfless support. I am a lucky layman who has the privilege to be companied by my wife, Chia-Lin Chou. Her patience and encouragement empower me to move onward in journey.

Surface Wave Manipulation with Polar Dielectric Thin Films and Topological Photonic System

Kueifu Lai, Ph.D.

The University of Texas at Austin, 2018

Supervisor: Chih-Kang Shih

Co-Supervisor: Gennady Shvets

Different from the well-studied wave propagation in the bulk where a plane wave extending to infinite is often conceived, the surface wave exists in the boundary defined by domains of distinct medium is well-confined with exponentially decaying tails away from this interface. This tightly-localized nature grants us enormous capability to manipulate the wave transport by tailoring the property of the interfaces and further enables various functionalities for practical applications. In this dissertation, a charged particle accelerator based on the surface phonon polaritons on the polar dielectric (silicon carbide) thin film is demonstrated to withstand high energy laser power and holds the promise of ultra-high accelerating gradiant. The framework of wave propagation is then expanded beyond the homogenized medium to crystals with discrete periodicity which is referred as photonic crystals. The Bloch wave construct predicts that the topological insulator, a novel phenomenon in solid state physics, can be emulated by exquisite design of photonic system. Consequently, the edge states between two topologically distinct photonic crystals exhibit robust and defect-immune wave transport which facilitates wide variety of applications. In particular, the RF delay line, polarized wave sorting, and two-beam accelerator based on the photonic topological insulator are investigated.

Table of Contents

Table of Contents viii

List of Tables xi

List of Figures xii

Chapter 1 Introduction 1

- 1.1 Introduction 1
- 1.2 Organization of this dissertation 2

Chapter 2 Electromagnetic Surface Waves 6

- 2.1 Guides Surface Waves at Single Interface 6
- 2.2 Guided Waves at Metal-Dielectric-Metal Interface 11

Chapter 3 Surface wave accelerator based on silicon carbide (SWABSiC) 14

- 3.1 Introduction 14
- 3.2 Beam-Driven Excitation with Density Modulated Electron Beam 17
- 3.3 Experiments in Accelerator Test Facility 20
  - 3.3.1 New Sample Fabrication and Holder Assembly 20
  - 3.3.2 Beamline 2 Configuration at ATF in BNL 22
  - 3.3.3 Installation in Interaction Chamber on Beamline 2 24
  - 3.3.4 Hot Testing SWABSiC at ATF in BNL 25
- 3.4 Summary and Comment 30

Chapter 4 Photonic Topological Insulator 31

- 4.1 Photonic Crystals 31
  - 4.1.1 Photonic Crystals and Bloch Waves 31
  - 4.1.2 Surface States in Photonic Crystals 34
- 4.2 Topological Photonics 37
  - 4.2.1 Brief Introduction to Topological Insulator 37
  - 4.2.2 QSH effect on Photonic Graphene 39

Chapter 5 Quantum Sin Hall Photonic Topological Insulator 41

- 5.1 Introduction to QSH PTI Platform 41

5.1.1 Brief Recap of QSH PTI Design 41
5.1.2 Topological Spin Chern Index and Topologically Protected Edge Waves 44
5.1.3 Toward experimental realization 45
5.2 Experimental Realization of QSH-PTI 46
5.2.1 Design and Fabrication of QSH-PTI Platform 46
5.2.2 Automated Test Station for RF Characterization 48
5.2.3 Simulation, Data Processing and Analysis 50
5.3 Verification of Topologically Protected Edge Waves 52
5.3.1 Verification of Fabricated Platform 52
5.3.2 Measuring the Topologically Protected Edge Waves 53
5.3.3 Robust Wave Propagation of TPEWs 56
5.4 Comparison to Topologically Trivial Waveguides 59
Chapter 6 Quantum Valley Hall Photonic Topological Insulator 61
6.1 Introduction to QVH PTI Platform 61
6.1.1 Brief Recap of QVH PTI Design 61
6.1.2 Topological Valley Chern Index and Topologically Protected Edge Waves 64
6.2 Experimental Realization of VSH PTI 67
6.2.1 Fabrication and Experimental Results of VSH PTI Platform 67
6.3 Summary and Comment 74
Chapter 7 Selective Mode Excitation on PTI Platforms 75
7.1 General Idea of Mode Excitation 75
7.2 Unidirectional Excitation on QSH PTI Platform 76
7.2.1 Excitation of Circular Polarized TPEWs 76
7.2.2 Experimental Result and Discussion 77
7.3 Unidirectional Excitation on QVH PTI Platform 82
7.3.1 Excitation of Valley-Polarized TPEWs 82
7.3.2 Experimental Result and Discussion 82
7.4 Summary and Comment 84

Chapter 8 Applications Based on PTI Platform 85
8.1 Compact Broadband RF Delay Line..85
8.1.1 Reflection-less Compact RF Delay Line 85
8.1.2 Experimental and Theoretical Demonstrations..........................86
8.1.3 Summary and Comment 90
8.2 Valley-Spin Sorting Platform 91
8.2.1 Introduction to Valley Wave Sorting Platform..........................91
8.2.2 Framework of Implemented Topological Indices......................91
8.2.3 Experimental Realization of the Sorting Platform.....................96
8.2.4 Summary and Comment 100
8.3 PTI as Two-Beam Accelerator...102
8.3.1 Concept of a Two-Beam Accelerator 102
8.3.2 Transition Radiation in Photonic Bandgap 105
8.3.3 Toward Experimental Realization 107
8.3.4 Summary and Comment 114
Chapter 9 Summary and Outlook 115
9.1 Dissertation Summary of Scientific Results 115
9.2 Outlook for Future Research...117
References..118
Vita 122

List of Tables

Table 5.1 Dimensions of the finalized design of QSH-PTI unit cell in this study47

Table 5.2 Input parameters of the LabView program for measuring QSH-PTI49

Table 6.1 Dimensions of the finalized design of QSH PTI unit cell in this study. 67

Table 8.1 Dimensions of QSH PTI platform unit cells as a TBA...................109

List of Figures

Figure 2.1 The coordinates for a surface wave propagating toward +X direction on an interface between two media with different permittivity. 6

Figure 2.2 The coordinates for a surface wave propagating toward +X direction on two interfaces of metal-dielectric-metal layered structure...............11

Figure 3.1 Cherenkov Radiation of SPhPs on SWABSiC. a) Schematic of electron passing through SWABSiC waveguide. b) Transverse dispersion curves of the accelerating (solid line) and deflecting (dashed line) modes that are synchronous with the electron bunches moving with $v = c$ (blue), and $v = 0.9c$ (red) velocities in the X-direction. Courtesy of Tianhong Wang. 17

Figure 3.2 Density modulated electron bunch simulation. a) 2-D profile of electron density modulation. b) Longitudinal field component along the bunch length. c) Beam energy plot. Courtesy of Tianhong Wang. 18

Figure 3.3 Energy profile simulation of transmitted electron. a) Density modulation with $\lambda L = 11.4\mu m$. b) Density modulation with $\lambda L = 10.3\mu m$ Courtesy of Tianhong Wang. 19

Figure 3.4 Newly fabricated piece of SWABSiC structure. a) Image of silicon brick with silicon carbide deposited on top. Two triangular patches are made of SU-8 photoresist. b) Schematic of the sample piece, yellow patches: gap spacer, cyan layer: silicon carbide thin film, gray brick: silicon substrate, red line: path of profilometer measurement. Inset: depth along the cutline showing the thickness of the spin-coated spacer............20

Figure 3.5 SWABSiC sample assembly. a) Schematic of sample holder. b) Schematic of sample assembly. Inset: photo of fully-assembled parts.21

Figure 3.6 Schematic and photos of beamline 2 configuration at ATF. Electron beam propagates from right to the left. Red arrow: a HeNe laser used for beamline alignment. Note that IPOP6 and IPOP7 are disabled........23

Figure 3.7 Photo and schematic of chamber installation of SWABSiC experiment. 24

Figure 3.8 Full set of measurement taken at laser power 3mJ. The energy profile below each spectrometer image is the pixel sum of the vertical direction. 25

Figure 3.9 Model optimizing for measurement without structure. a) spectrometer images for laser on/off. b) energy profile. c) optimized spectrum by the model. Model out puts of only d) normalization. e) energy drift. f) energy drift...26

Figure 3.10 Result of phenomenological model optimizing. Energy spread parameter extracted from a) without structure and b) with structure c) Power dependent energy spread parameter. Blue star: without structure, red diamond: with structure, dashed line: linear fit of the scatter points.28

Figure 4.1 Examples of photonic crystals with periodicity a0in different dimensions. a) a stack of slabs as 1D PCs. b) a wire or uniaxial medium as 2D PCs. c) a cubic lattice of bricks as 3D PCs. Red and blue domains are the media of different refractive index.......................................31

Figure 4.2 Schematic of Bloch wave decomposition in the solution of a 1-D photonic crystal. Purple: full solution, blue: plane wave, red: local field for the case of a) using an arbitrary reciprocal vector $\mathrm{k1}$. b) using reciprocal vector $\mathrm{k2}$ with the relation $\mathrm{k2} - \mathrm{k1} = \mathrm{G}$, where G is the reciprocal lattice vector. 33

Figure 4.3 Conceptual illustration of a surface wave at the boundary between two dissimilar 1-D PCs made of the same material. Red curve: intensity of the EM waves, Gray dashed curve: exponential decaying envelope of a surface wave, indigo region in the inset: medium with high refractive index........ 35

Figure 4.4 Examples of crystal defects in PCs of different dimensions. Green region: site of crystal defect where the possible imperfections are the discrepancy of physical dimension, material properties or even topology. 36

Figure 4.5 Classical image of electron transport in the case of quantum Hall effect. 38

Figure 5.1 The fabrication of a QSH-PTI platform. a) Schematic of the platform layout totaling 45×20 periods of PCs. Part of the top metal plate is removed to reveal the cylinders attached to the bottom plate (green, $\Delta\mathrm{em} > 0$) and to the top plate (purple, $\Delta\mathrm{em} < 0$), leaving a gap to the other plate. b) Finalized geometric parameters of the unit cell of the QSH-PTI. See Table 5.1 for values of the parameters. c) Picture of fabricated structure made of aluminum. 46

Figure 5.2 RF test station for probing QSH-PTI platform. Schematic of the setup. PC is used to control both VNA and stage. A: transmitting antenna stuck into the platform, B: receiving antenna place outside of the edge of platform. Insets are the picture of VNA and linear translation stage respectively. 48

Figure 5.3 Bulk modes measurement and simulation verification. a) Schematic of the setup for testing the platform containing one kind of QSH-PTI (all rods attached to the bottom plate). A: launching port at 5 periods from the edge, B: receiving port placed outside of the structure. b) Calculated photonic band structure of the QSH-PTI. c) Measured transmission spectra S212 through the bulk PTI. Cyan: bulk modes, gray region: complete PBG. 52

Figure 5.4 Experimentally measured TPEWs. a) Schematic of platform layout of the platform containing topologically non-trivial interface between two dissimilar QSH-PTI domains. A: launching port, B: receiving port. b) Calculated photonic band structure with topologically non-trivial interface. Cyan: bulk modes, red curve: edge states inside the PBG, gray region: complete PBG. c) Measured transmission spectra S212 through the bulk PTI. Black: bulk modes, red: edge states. 54

Figure 5.5 Edge scan measurement of TPEWs. a) A straight path of wave propagation. b) Color map consists of 257 transmission spectra taken at the edge of the structure to show the localized spatial confinement of the edge modes. White dashed line: spectral position at mid-gap frequency, red dashed line: the spectral region of the topologically non-trivial PBG hosting the TPEWs. Inset: the line cut at the mid-gap frequency to show the confinement of the wave at the interface ($y = 0$). 55

Figure 5.6 Edge scan measurement of TPEWs propagating along a detoured path. a) A detour path of wave propagation. Red circle: sharp corner of a severe defect. b) Color map consists of 257 transmission spectra taken at the edge of the structure to show the localized spatial confinement of the edge modes. White dashed line: spectral position at mid-gap frequency, red dashed line: the spectral region of the topologically non-trivial PBG hosting the TPEWs. Inset: the line cut at the mid-gap frequency to show the confinement of the wave at the interface ($y = 0$). 57

Figure 5.7 Robust test of TPEWs propagating along a detour path. a) Comparison of measured transmission spectra between the straight (red curve) and the detour (green curve) interfaces b) Simulated energy density at$f = 6.08$ GHz showing the TPSW flowing around the defect without scattering. 58

Figure 5.8 Experimentally measured TTGWs. a) Schematic of platform layout of the platform containing topologically trivial interface between two dissimilar QSH-PTI domains. A: launching port, B: receiving port. Note that one row of rods is removed to create a defect waveguide for TTGWs. b) Calculated photonic band structure with topologically trivial interface. Cyan: bulk modes, orange curve: defect modes inside the PBG, gray region: complete PBG. c) Measured transmission spectra $S212$ through the bulk PTI. Black: bulk modes, orange: defect modes. 59

Figure 5.9 Robust test of TTGWs propagating along a detoured path. a) A detour path of wave propagation. Red circle: sharp corner of a severe defect. b) Comparison of measured transmission spectra between the straight (orange curve) and the detour (blue curve) path. c) Simulated energy density at $\mathrm{f} = 2.95\ \mathrm{GHz}$ showing the TTGW resonant tunneling through the defect. 60

Figure 6.1 Deformation of the unperturbed unit cell of photonic graphene to the broken in-plane inversion symmetry. 61

Figure 6.2 PBS of QVH PTI unit cells with various perturbation strength. Field profiles of the relevant bands at K(K’) point for a) $|\mathrm{EZ}|$ component of TM modes and b) $|\mathrm{HZ}|$ component of TE modes at $\theta = 0°, 30°, 60°$. Color plot: strength of field component; black arrow: Poynting flux.64

Figure 6.3 Dispersion relation of the TPEWs at QVH/QVH ($\Delta P > 0, \Delta P < 0$) interface. a) The geometry of the topological interface (black dashed line) between two QVH PTIs. The boundary condition of supercell simulation is periodic in X-direction. b) Calculated PBS of the TPEWs. Red curves: TE polarization, blue curves: TM polarization. 65

Figure 6.4 Realistic design of QVH PTI. a) tripod-like shape metallic cylinder breaking in-plane symmetry. b) Side-view of the metallic tripod suspended between two parallel metallic plates leaving two symmetric gaps between the cylinder and two plates. This preserves the symmetry which is used for tailoring spin DOF in Chapter 5. c) PBS of the QVH PTI. Red curves: topologically non-trivial modes. 67

Figure 6.5 The experimental set-up for measuring kink states. a) The zigzag domain wall is indicated with a dashed line. The inset is a zoomed-in photo. The upper metallic plate of the parallel-plate waveguide is removed for illustration. b) Measured Hz2transmittance. Grey/red curves are for straight/zigzag domain walls, respectively. Purple curve is for a straight domain wall when the bandgap in the upper domain closes. c) Measured Ez2 transmittance. Grey/blue curves are for straight/zigzag domain walls, respectively. Purple curve is for a straight domain wall when the bandgap in the upper domain closes. Courtesy of Fei Gao...............68

Figure 6.6 The edge scan of the QVH/QVH interface. a) the configuration of the spatial edge scan along the transversal direction respect to the exit of a straight topological interface. b) Ez and Hz components of transmitted TE (red) and TM (blue) respectively. The decaying tails away from the interface are apparent in both cases. Courtesy of Fei Gao................69

Figure 6.7 Defect test of TPEWs transport on QVH PTI platform. a) Location of the defect (a square cylinder) at the interface. b) Measured reflectance of TE and TM modes respectively. Black curves are the reflectance from the zigzag domain wall. Green curves are for the case when a square metallic rod replaces one tripod at the domain wall, as shown in a. Error bars represent the standard deviation of multiple measurements. Courtesy of Fei Gao. 70

Figure 6.8 Topologically protected refraction of TE-polarized TPEW into an empty waveguide region. a) Measurement of $Hz2$ reflectance for zigzag (grey) and armchair (purple) terminations. Error bars represent the standard deviation of multiple measurements. b) The iso-frequency analysis on the out-coupling of the TE polarization. Red circle: dispersion of TE modes in the parallel-plate waveguide, black dot: K' valley. c) The spatial scan at $f = 6.12GHz$ indicating the refraction of TE states through the zigzag (left) and armchair (right) termination. The white bars indicate the position of phase-arrayed dipoles. The insets are the experimentally measured field patterns. Courtesy of Fei Gao..........71

Figure 6.9 Topologically protected refraction of TM-polarized TPEW into an empty waveguide region. a) Measurement of E_{z2} reflectance for zigzag (grey) and armchair (purple) terminations. Error bars represent the standard deviation of multiple measurements. b) The iso-frequency analysis on the out-coupling of the TM polarization. Blue circle: dispersion of TM modes in the parallel-plate waveguide, black dot: K' valley. c) The spatial scan at $f = 6.12\mathrm{GHz}$ indicating the refraction of TM states through the zigzag (left) and armchair (right) termination. The white bars indicate the position of phase-arrayed dipoles. The insets are the experimentally measured field patterns. Courtesy of Fei Gao....72

Figure 7.1 Experimental setup for unidirectionally excite TPEWs on QSH PTI platform. a) Schematic of source feeding and location of antennas. The topological interface is denoted by the red dashed line. (b) Photograph of setup described in a). Inset: Arrangement of the two loop coils which are in the air gap of a cylinder at the interface.......................................77

Figure 7.2 Transmission amplitude on the a) left side and b) right side of the PTI platform as a function of the frequency while the phase difference ϕ of the two launching loop antennas is varied from 0 to 2π. The probe is positioned at the center of the edge. The BMW bulk band gap extends from 5.80 to 6.47 GHz, as shown by the dashed vertical lines.........78

Figure 7.3 CST simulation results for transmission amplitude on the left and right sides of the QSH PTI structure while both the phase difference ϕ and the driving amplitude (parameterized by angle $\theta \in 0,2\pi$) of the two loop antennas are varied. Results are shown for a) left side and b) right side at $6.08\mathrm{GHz}$..80

Figure 7.4 Unidirectional excitation of TPEWs on QVH PTI platforms. a) Schematic of a similar signal feeding setup as in the Figure 5.2. b) Photo of sample for unidirectional excitation calibration. Blue stars represent the phase array source. Red and black dots indicate minimum and reference probe positions. Blue cones are electromagnetic absorbers82

Figure 7.5 Photos of reflectance measurement setup in Chapter 6. a) Photo of zigzag termination. b) Photo of armchair termination. Blue stars represent the phase array source. Black dot indicates probing positions. Blue cones are electromagnetic absorbers 83

Figure 8.1 Photonic delay line applications based on QSH PTI. Top half: the relative phases extracted from the transmission spectra of straight path and defect path; bottom half: the time delays of delay line application on the platforms of (a) TPEWs and (b) TTGWs..................................86

Figure 8.2 Schematic of full-size time delay simulation. a) straight path as the baseline for calculating time delay. b) various paths of wave propagation. Cyan line: path with one detour (the same as in experimental measurement), gray dashed line: path with one elongated detour, yellow dashed line: path with two detours. Color: energy density of spin-up (rightward propagating) wave. The launching probe locates at the leftmost edge of the structure..87

Figure 8.3 Calculated time delays of various configurations in Figure 8.2. 88

Figure 8.4 Transmission spectrum of TTGWs on path with double detours. The scale is normalized to the highest peak of resonance tunneling. Insets: the profile of energy density at transmission peaks. Red arrow: the FP resonance peak, grey arrows: extra transmission peaks of cross-talking in the waveguide. 89

Figure 8.5 Stacking two TTGWs delay line for the spectral position indicated by the red arrow in Figure 8.4. The platform consists of one bus waveguide and with of a) one detour, b) two detours. Note that the elapsed time of the straight path is not subtracted in this figure. Blue circle: calculated elapsed time, red curve: curve fitting of a Lorentz function. The number representing the area of shaded area below the curve, which is effectively the integrated DBP over the spectral range of interest. ..90

Figure 8.6 Designs of photonic crystal with non-trivial topology. a) QSH PTI. b) QVH PTI. c) Schematic unit cell of QVH PTI illustrating rotation angle θ between the tip of tripod (red dashed line) and negative y-direction (red solid line). The symmetry-breaking perturbation is maximized at $\theta = 0° \ \Delta P > 0, 60° \ \Delta P < 0$. d) dand e) Calculated photonic band structures of d) QSH PTI and e) QVH PTI at $\theta = 0°$. Red curves: topologically non-trivial modes; black curves: dispersion of bulk modes; gray shaded area shows a complete photonic bandgap centered at $f0 = 6.08 \mathrm{GHz}$ with 7% bandwidth. 93

Figure 8.7 TPEWs with valley-spin locking propagation. Photonic band diagrams of a heterogeneous interface between: a) QSH/QVH PTIs ($\Delta\mathrm{SOC} > 0, \Delta\mathrm{P} > 0$) b) QSH/QVH PTIs ($\Delta\mathrm{SOC} > 0, \Delta\mathrm{P} < 0$). The band structure is calculated with a supercell with periodicity $a0$ along X-direction and 15 cells on each side of the domain wall. Red solid curves: positive index TPEW; red dashed curves: negative index TPEW; black dots: bulk modes; edge modes are denoted with positive/negative ($+ -$) indices and up/down ($\uparrow\downarrow$) spins. Inset: Ezcomponent for two kinds of QSH/QVH interfaces in supercell simulation (only 10 cells are shown); blue double circles: locations of low Ez value at the vicinity of domain wall for preferential mode excitation. 94

Figure 8.8 Demonstration of valley wave sorting on a valley-spin locked platform. a) Schematic of radio frequency test station. The launching antenna (Port A) sticks into the structure through a drilled hole located $a0$ from leftmost edge on the bottom plate. The receiving antenna is mounted on a translation stage to scan along the outer edges of the platform at Port B or Port C. The transmitted signal through channel A-B or A-C is measured by a vector network analyzer. Inset: the fabricated platform with top plate removed to reveal the layout of PCs. b) Schematic and picture of Port A indicating preferential mode excitation using different launching locations. Red double circle: positive-preferred excitation; purple double circle: negative-preferred excitation. 97

Figure 8.9 Energy routing of the platform with positive-preferred excitation. Schematic of valley-polarized waves routing a) with QVH PTI at $\theta = 0°$ $(\Delta p > 0)$. b) with QVH PTI at $\theta = 60°$ $(\Delta p < 0)$. Green: QSH PTI with $\Delta SOC > 0$, blue: QSH PTI with $\Delta SOC > 0$, yellow: QVH PTI with $\Delta P > 0$, red: QVH PTI with $\Delta P > 0$. Red and purple arrows: positive and negative index waves..98

Figure 8.10 Transmission measurements of the valley sorting platform with c) positive-preferred excitation and d) negative-preferred excitation. Blue star (green circle) shows the summation of experimentally measured $S212$ through A-B (A-C) channel. Numerical simulation of the transmission through A-B (blue dashed curve) and A-C (green dashed curve) channels agrees well to experimental observations. The tripods are rotated gradually from $\theta = 0°$ to $\theta = 60°$ (from $\Delta P > 0$ to $\Delta P > 0$) with $10°$ per step. Insets: energy density plots of full-size simulation at $\theta = 0°$ to $\theta = 60°$ showing the energy is in fact routed according to the topology swapping of two QSH/QVH interfaces. 99

Figure 8.11 Conceptual schematic of a two-beam accelerator (TBA) based on a compact photonic structure that avoids reflections due to topological protection of the interface-guided electromagnetic waves. (a) The concept: a high-current low energy driving beam is slowed down in the lower portion of the accelerating structure, while the low-current high-energy main beam is accelerated in the upper portion of the structure. The power flow between the decelerating and accelerating portions of the structure occurs along the sharply bent interface between two PTIs of the type shown in Figure 5.6b...103

Figure 8.12 Simulated results of transition radiation in a PBG. a) The layout of the PTI accelerating platform with a straight interface between $\Delta\mathrm{SOC} > 0$ (green) and $\Delta\mathrm{SOC} < 0$ (purple) domains of PCs. b) Calculated result of radiated power with semi-analytical model. Orange (blue) scatters: TPEWs power integrated over the top (bottom) edge of the structure as shown in a). 106

Figure 8.13 Drawings of 6-way cross vacuum chamber with in AWA. This chamber designated to be used for testing the transition radiation on PTI platform. a) Orientation of the accelerating structure in the chamber. The chamber is rendered transparent to show how the structure (indicated by the origin) is fixed to the actuator on the top flange. b) The drawing showing the actuator retraction of the 3-inch (76.2mm) distance of travel. The electron beam is passing through the center of the chamber (concentric to the PTI structure). c) The $10\mathrm{mm}$ secure clearance between structure and the wall of chamber after the actuator fully retracted. Half of the chamber is removed to show the clearance...................................108

Figure 8.14 Schematic drawing of QSH PTI platform. a) The layout and the geometric parameters of the platform for testing transition radiation in PBG. Purple: rods attached to top plate, green: rods attached to bottom plate, blue arrow: electron beam, red arrow: TPEWs. b) The orientation of the assembled PTI accelerating structure with cable holder and counter weight. c) The aperture of the sample for electrons passage.110

Figure 8.15 Technical drawings of fixture parts. a) Cable holder. b) Fixture extension. c) Fixture joint. Note that the sketches are not to the real scale..111

Figure 8.16 Schematic of parts assembling. a) fully-assembled PTI accelerating structure with fixture to the actuator. b) washers (highlighted blue) for tweaking the pitch alignment. c) probes held by the cable holder. Orange: loop antennas..112

Figure 8.17 Fabricated PTI accelerating structure. The balance of is checked by hanging the assembly mid-air with a twist-tie wire (black wire in the through hole). Note that the fixture extension piece is neglected in this balance test since it is symmetric to the actuator axis thus it doesn’t shift the center of gravity. 113

Chapter 1 Introduction

1.1 INTRODUCTION

The intriguing phenomenon of light-matter interaction has long been fueling up interest of fundamental research. Numerous discoveries based on studying and explaining these phenomenon lead to the theory of electromagnetism, which is undoubtfully one of the most successful theoretical constructs of physical science. Depending on the scope of problems, the governing formula of the electromagnetism, Maxwell's equations, can be specialized into a set of master equations under specific assumptions to better tackle the problem with ease. For example, the electromagnetic wave equation describing waves propagating in the vacuum or a medium can be derived under the assumptions of charge-free and current-free in Maxwell’s equations. In this dissertation, the author will discuss a special class of solutions to the electromagnetic wave equation, which is the surface wave in electrodynamics. Different from the well-known propagating wave solutions in a bulk medium, surface wave is a propagating mode guided at the boundary between two different media. The most distinctive signature of this type of modes is the localized energy distribution at the boundary with exponentially decaying tails extending away from the interface.

Due to the nature of light-matter interaction derived from Maxwell’s equations, surface waves also largely depend on the properties of materials forming the boundary as the same as the propagating waves in the bulk medium. In this thesis, two of the most extensively studied examples of surface waves in the past two decades, namely surface plasmon polariton (SPP) at boundary between a dielectric material and a metal [1,2,3,4] and edge states in photonic crystals [5] are scrutinized with both numerical simulations and experimental examinations. Aside from these two famous instances, surface waves are also shown to exist at interfaces consisting of various types of materials, such as distinct dielectric constant [6,7], anisotropic materials [8,9], chiral materials [10], gyrotropic materials [11], and interfaces between linear and nonlinear media [12].

During my PhD research, I have investigated several surface wave platforms based on different operating principle that demonstrate functionalities with great potential to be utilized in several future applications, such as reflection-free broadband radio frequency (RF) delay line, polarized wave sorting and dispatching, RF signal de/multiplexing, and charged particle accelerator. The result and discussion of these relevant research projects are included in this dissertation.

1.2 ORGANIZATION OF THIS DISSERTATION

This thesis is structured as follows: Chapter 1 introduces the general concept of surface waves in electrodynamics and focuses on a specific scope of this dissertation. The content of the remaining chapters is outlined as a lookup guide for readers. In Chapter 2, an introductory background of surface waves is briefly reviewed. Moreover, an analytical construct of electromagnetic wave equation in Maxwell's equations with a focus on the surface waves at the metal-dielectric interface as well as metal-dielectric-metal interface are presented to establish common ground for the following chapters.

In Chapter 3, one kind of dielectric material, namely the polar dielectrics, is considered instead of metal to form a boundary with non-polar dielectric materials. To meet the explicit requirement of hosting surface waves at the interface, polar dielectric materials are shown to have negative dielectric permittivity due to the surface phonon polariton resonance in *reststrahlen* band. A specific application of such a surface wave, surface wave accelerator based on silicon carbide (SWABSiC), is proposed based on its all-dielectric design and commercially available high-power CO_2 laser. While the preliminary sample verifications and benchtop test have been covered in the previous work, this chapter focuses on the electron beam test with the SWABSiC. Specifically, a new method of exciting surface wave on the polar/non-polar interface with density modulated electron beam is used in the experiments. This research project is in collaboration with Professor Pietro Musumeci's group in University of California, Los Angles and Accelerator Test Facility in Brookhaven National Laboratory (ATF BNL).

The rest of the thesis is devoted to a newly advent field, Topological Photonics, which evolves along the way of persuading photonic analogue of the topological insulator in condensed matter physics. While featuring multiple novel phenomenon and great future potential, the concept of topological photonics can be readily interpreted with Maxwell's equations and is, in fact, in close connection with the surface waves in homogenized media as discussed in Chapter 2 and 3.

Serving as an introductory chapter, Chapter 4 first presents a basic review of the photonic crystals, a system comprised of optical structures with discrete periodicity demonstrating collective behavior of electromagnetic waves. The surface wave is then rephrased in the language of Bloch wave to pave the way to the more abstract concept. The second part of chapter brings up the concept of topology and its role in the photonic crystals. A fruitful example of exploiting the topological properties of the photonic crystals, namely the photonic topological insulators (PTIs), is recently proposed and realized in the practical systems by researcher around the globe. The field of PTIs draws a lot of attention due to the capability to support a topologically protected edge waves at the domain wall between two topologically distinct domains. The signature property of TPEWs is the robust and defect-immune wave propagation if the symmetry of the system is preserved. Such kind of waves is evidently categorized as the surface wave in photonics systems since it exists only at the boundary and have exponential decaying tails into the bulks. This chapter will concisely summarize the general principles of designing the PTIs and give a thorough study of a specific platform in the following chapters.

In Chapter 5, a specific design encompassing three independent degrees of freedom is studied in this thesis. Using the principles covered in the previous chapters, an unperturbed photonic unit cell is considered as the most basic building block of the PTI platforms. To construct spin DOF, a specific kind of symmetry-breaking perturbation, *i.e.* mirror symmetry in z-axis, is imposed onto the unperturbed design building block. The resulting spin photonic crystal is then shown to emulate quantum spin Hall (QSH) effect from effective Hamiltonian analysis and is referred as QSH PTI. Furthermore, this platform is demonstrated numerically and experimentally to support TPEWs at the domain wall between QSH PTIs with opposite signs of perturbations. The robust and defect-immune wave transport is exhibited by comparing to EM wave on a topologically trivial system.

In Chapter 6, another kind of perturbation breaking in-plane inversion symmetry further extends the unperturbed building block to grant the system with nontrivial lattice topology. Specifically, this perturbed unit cell emulates quantum valley Hall (QVH) effect and thus is referred as the QSH PTI in this thesis. Similarly, a boundary between two QVH PTIs with opposite topology is shown to support TPEWs with valley DOFs in numerical simulations. With the collaboration with Professor Baile Zhang's group at Nanyang Technological University in Singapore, the experimental realization is demonstrated to be in good agreement with theoretical simulation.

In Chapter 7, a general methodology of preferential mode excitation based on antenna theory is introduced. In addition to theory, a phenomenological model is presented to bridge the discrepancy from theoretical inception to practical realization. An example with Professor Steven Anlage's group at University of Maryland focuses on unidirectional excitation QSH PTIs platform using two loop antennas is presented in this chapter. Furthermore, another example of preferential excitation is mentioned in the collaborated QVH PTIs project to showcase the wide application of this methodology.

In Chapter 8, several applications based on TPEWs platforms have been proposed and demonstrated theoretically as well as experimentally. First, a compact broadband RF delay line with suppressed cross-talking is realized on the QSH PTI platform. The advantage of using such a platform of topologically protected wave transport is strengthen compared to the topologically trivial platform. Second, a hybrid platform implements two independent binary DOFs (spin and valley) and thus is evidently able to grant more functionalities compared to platform with only one binary DOF. In addition, a method of preferential mode excitation using a simple linear dipole antenna is also presented. Third, another potential application of PTIs is investigated. The concept of two beam accelerator (TBA) scheme is adapted to a platform of QSH PTI. A semi-analytical model developed by a group member, Yang Yu, is briefly presented in this chapter to explain the preferential mode excitation. The sample design and current results of the ongoing experiment in collaboration with Argonne Wakefield Accelerator (AWA) Facility in Argonne National Laboratory are covered in detail for future reference.

Finally, Chapter 9 summarizes the main results of the proceeding chapters and wraps up the thesis with concluding remarks. Furthermore, several potential directions of the relevant projects are outlined for future researchers’ information.

Chapter 2 Electromagnetic Surface Waves

2.1 GUIDES SURFACE WAVES AT SINGLE INTERFACE

The Maxwell's equations in a linear, homogeneous and isotopic medium where there is no free charge and no free current take the following form. MKS unit will be used throughout this dissertation.

$$\nabla \cdot \mathbf{E} = 0 \qquad \nabla \cdot \mathbf{B} = 0$$
$$\nabla \times \mathbf{E} = -\frac{\partial}{\partial t}\mathbf{B} \qquad \nabla \times \mathbf{B} = \mu\varepsilon\frac{\partial}{\partial t}\mathbf{E} \tag{2.1.1}$$

In which ε is the electric permittivity and μ is the magnetic permeability of the medium.

With the focus on the guided wave at the boundary, it is intuitive to derive the formula of surface wave by solving the wave equations under the presumption that the transverse distribution of the field decays exponentially away from the interface. To begin with, we can define a cartesian coordinate system with a surface wave located at the boundary between two media as shown in the in Figure 2.1, where ε_1 and ε_2 is the dielectric constant of material 1 and 2 respectively.

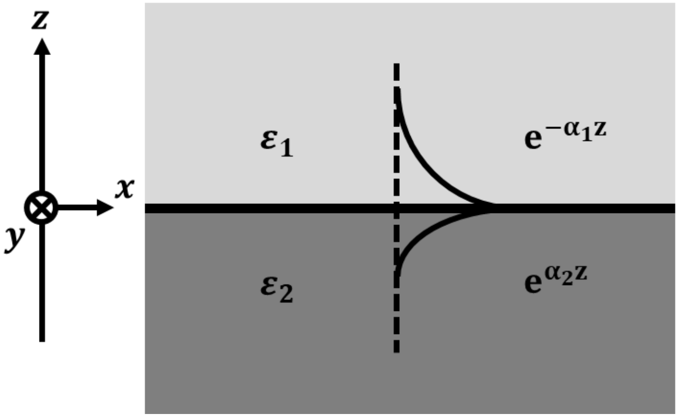

Figure 2.1 The coordinates for a surface wave propagating toward +X direction on an interface between two media with different permittivity.

Without losing the generality, we choose this wave with propagating constant k travels toward +X direction with the exponential decaying tails in +Z and -Z direction with decay constant α_1 and α_2 respectively. We can omit the harmonic time dependent factor $e^{-i\omega t}$, where ω is the angular frequency and i is the imaginary unit, and further suppress the dispersion implicitly into the expression, *i.e.* $\varepsilon(\omega) = \varepsilon$. Next, we consider a transverse magnetic (TM) wave with $E_y = 0$ and the components of electric field in material 1 take the general form.

$$\begin{aligned} E_x &= A \cdot e^{ik_x x - \alpha_1 z} \\ E_y &= 0 \\ E_z &= B \cdot e^{ik_x x - \alpha_1 z} \end{aligned} \tag{2.1.2}$$

where A and B are constants. Next, combining two curl equations from (2.1.1) yields the following equation.

$$\nabla \times \nabla \times \mathbf{E} = \varepsilon_r \frac{\omega^2}{c^2} \frac{\partial^2 \mathbf{E}}{\partial t^2} \tag{2.1.3}$$

in which $\varepsilon_r = \varepsilon/\varepsilon_0$ is the dielectric constant of the medium, $c = 1/\sqrt{\mu_0 \varepsilon_0}$ is the speed of light in vacuum, μ_0 and ε_0 are magnetic permeability and electric permittivity of vacuum respectively. For the sake of simplicity, we limit the discussion to the case that the dielectric constant is mostly real, *i.e.* $|\mathrm{Re}[\varepsilon_r]| \gg |\mathrm{Im}[\varepsilon_r]|$ and nonmagnetic $\mu \approx \mu_0$. The cartesian components of (2.1.3) can be explicitly written down.

$$\left(-\frac{\partial^2 E_x}{\partial z^2} + \frac{\partial^2 E_z}{\partial x \partial z}\right)\hat{x} + \left(\frac{\partial^2 E_x}{\partial x \partial z} - \frac{\partial^2 E_z}{\partial x^2}\right)\hat{z} = \varepsilon_r \frac{\omega^2}{c^2}(E_x \hat{x} + E_z \hat{z}) \tag{2.1.4}$$

Inserting (2.1.2) into (2.1.4), we can obtain equations for the fields above the surface.

$$\begin{aligned} -\alpha_1{}^2 A - ik_x \alpha_1 B &= \varepsilon_1 \frac{\omega^2}{c^2} A = \varepsilon_1 k_0{}^2 A \\ -ik_x \alpha_1 A + k_x{}^2 B &= \varepsilon_1 \frac{\omega^2}{c^2} B = \varepsilon_1 k_0{}^2 B \end{aligned} \tag{2.1.5}$$

where $k_0 = \omega/c = 2\pi/\lambda$ is the vacuum wavevector and λ is the wavelength in vacuum. Applying charge free condition $\nabla \cdot \mathbf{E} = 0$ to (2.1.2) yields the relation: $ikA - \alpha_1 B = 0$ which can be substituted into (2.1.5). And the resulting dispersion relation, namely the relation between wavevector and frequency of the wave, can be expressed without arbitrary constants A and B as following equation for the surface wave in material 1.

$$-{\alpha_1}^2 + {k_x}^2 = \varepsilon_1 {k_0}^2 \tag{2.1.6}$$

Likewise, the electric field components of the guided wave in the region below surface take the general form.

$$\begin{aligned} E_x &= C \cdot e^{ik_x x + \alpha_2 z} \\ E_y &= 0 \\ E_z &= D \cdot e^{ik_x x + \alpha_2 z} \end{aligned} \tag{2.1.7}$$

where C and D are constants. Note that the sign of the decay factor is reversed due to the region of interest is below the surface ($z < 0$). Applying similar treatment to (2.1.7), we can obtain the dispersion relation of surface wave in material 2.

$$-{\alpha_2}^2 + {k_x}^2 = \varepsilon_2 {k_0}^2 \tag{2.1.8}$$

These two relations need to be related by matching the boundary conditions of tangential electric field and normal electric displacement across the interfaces.

$$\varepsilon_2 \alpha_1 = -\varepsilon_1 \alpha_2 \tag{2.1.9}$$

Inserting (2.1.9) into (2.1.6) and (2.1.8), one can obtain equations of the wavevector and dispersion relation in medium 1 and 2.

$$k_x = \sqrt{\frac{\varepsilon_1 \cdot \varepsilon_2}{\varepsilon_1 + \varepsilon_2}} k_0; \ \alpha_1 = \sqrt{\frac{-{\varepsilon_1}^2}{\varepsilon_1 + \varepsilon_2}} k_0; \ \alpha_2 = \sqrt{\frac{-{\varepsilon_2}^2}{\varepsilon_1 + \varepsilon_2}} k_0 \tag{2.1.10}$$

Bear in mind that the premise of this derivation is a bonded surface wave traveling along the interface which implies $\mathrm{Re}[k_x] > 0, \mathrm{Re}[\alpha_1] > 0, \mathrm{Re}[\alpha_2] > 0$. Therefore, the surface wave exists only when $\varepsilon_1 + \varepsilon_2 < 0$ and $\varepsilon_1 \cdot \varepsilon_2 < 0$. The simplest example satisfying this condition is an interface between air with dielectric constant $\varepsilon_D \approx 1$ and a metal with $\varepsilon_M < -\varepsilon_D < 0$. In this case, the negative dielectric constant of metal can be supported by the electron plasma oscillation of the metal at high frequency based on the Drude model with $\varepsilon_M = \left(1 - \frac{\omega_p{}^2}{\omega^2}\right)$ where $\omega_p = \frac{nq^2}{\varepsilon_0 m}$ is the plasma frequency and n, q, m is the density, charge, and mass of the electron in the metal respectively. Therefore, surface waves at the interface between dielectric and metal are referred as surface plasmon polaritons (SPPs) owing to the coupling between electromagnetic waves and oscillations of the electron plasma in conductors.

On the other hand, the dielectric constant of the metal is a large imaginary number at much lower frequency, *i.e.* $\omega \ll 1/\tau$, where τ is the mean electron collision time in the Drude model. The dispersion relation approximates to a simple form: $k_x \approx k_0$ and the field of the wave extends a great distance into the dielectric material. For example, the electric field of a 6 GHz surface wave on the boundary of aluminum 6061 extends 100 meters into the air whereas the skin depth is only $1.25\ \mu m$ into the metal. Hence, these surface waves at low frequency limit can be described as the surface currents which are merely AC currents on good conductors.

It is also worth mentioning that the discussion in this section can be applied to transverse electric (TE) waves with cartesian components of magnetic field instead of the electric fields in (2.1.2) and similarly in the double curl equation (2.1.4). However, the boundary conditions at the interface, namely the continuity of tangential magnetic field strength, will require the following relation.

$$\alpha_1 + \alpha_2 = 0 \qquad (2.1.11)$$

The assumption for a bounded surface wave at the interface, namely $\mathrm{Re}[\alpha_1] > 0$ and $\mathrm{Re}[\alpha_2] > 0$, implies that the only solution is trivial: $\alpha_1 = \alpha_2 = 0$. Thus, there is no surface wave exists with TE polarization at the boundary between dielectric and metal. In other words, surface plasmon polariton only exist for TM polarization.

In addition, an important is that the wavevector of the SPPs is large than the wavevector of free-space photons, namely $k_x > k_0$, which implies that a plane wave impinging from the air side is not capable of exciting SPPs on a metal surface. Based on the same argument, travelling SPPs bounded on a smooth metal surface cannot radiate photons into the air due to this momentum mismatch. It is, however, possible to alleviate this limitation and launch the SPPs using photons with the help of extra momentum from periodic patterning of the surface or high index coupling medium. Aside from photons, SPPs can be launched by firing electrons into the metal. The electrons transfer energy to the bulk plasma during the scattering process and thus create collective oscillation at the surface.

One thing to keep in mind is that the above-mentioned surface plasmon polariton modes are not the only type of guided solutions to Maxwell's equations of the interface separating two media. Depending on the properties of the materials, for examples, the radiative modes between air and either ground or water is known as Norton ground wave [7]. On the other hand, the non-radiative mode or transmission line mode is called Zenneck wave [6]. There is also a solution at the interface with dissimilar symmetry of crystal media, which is known as D'yankonov wave [8]. The discussion of these solutions, however, is beyond the scope of this dissertation and the readers of interest will be advised to consult the referred literatures for further details.

2.2 GUIDED WAVES AT METAL-DIELECTRIC-METAL INTERFACE

With the understanding of the surface waves on single interface in the previous section, we are now ready to expand our scope to the surface waves supported on a layered metal-dielectric-metal structure consisting of two interfaces as shown in Figure 2.2.

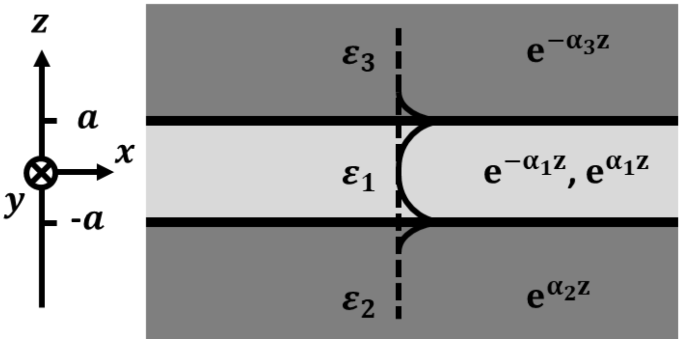

Figure 2.2 The coordinates for a surface wave propagating toward +X direction on two interfaces of metal-dielectric-metal layered structure.

The dielectric layer in the middle is from $z = -a$ to $z = +a$ while the thickness of metals is set to infinite for the simplicity of discussion. With the same focus on a traveling surface wave bonded at the layered structure, we again assume the wavevector k_x along +X direction and exponentially attenuating tails away from the interfaces with the decay constants α_j where $j = 1,2,3$. For $z > a$, the cartesian components of the TM surface wave takes the form

$$\begin{aligned} E_x &= A_1 \cdot e^{ik_x x - \alpha_3 z} \\ E_y &= 0 \\ E_z &= A_2 \cdot e^{ik_x x - \alpha_3 z} \end{aligned} \tag{2.2.1}$$

while for $z < -a$ we have

$$\begin{aligned} E_x &= B_1 \cdot e^{ik_x x + \alpha_2 z} \\ E_y &= 0 \\ E_z &= B_2 \cdot e^{ik_x x + \alpha_2 z} \end{aligned} \tag{2.2.2}$$

in the dielectric region $-a < z < a$

$$
\begin{aligned}
E_x &= C_1 \cdot e^{ik_x x + \alpha_1 z} + D_1 \cdot e^{ik_x x - \alpha_1 z} \\
E_y &= 0 \\
E_z &= C_2 \cdot e^{ik_x x + \alpha_1 z} + D_2 \cdot e^{ik_x x - \alpha_1 z}
\end{aligned}
\qquad (2.2.3)
$$

where $A_1, A_2, B_1, B_2, C_1, C_2, D_1, D_2$ are constants which can be related by matching the boundary conditions of the dielectric-metal interfaces at $z = -a$ and $z = a$.

$$
\begin{aligned}
A_1 \cdot e^{-\alpha_3 a} &= C_1 \cdot e^{\alpha_1 a} + D_1 \cdot e^{-\alpha_1 a} \\
A_2 \cdot e^{-\alpha_3 a} &= C_2 \cdot e^{\alpha_1 a} + D_2 \cdot e^{-\alpha_1 a}
\end{aligned}
\qquad (2.2.4)
$$

at $z = a$ and

$$
\begin{aligned}
B_1 \cdot e^{\alpha_2 a} &= C_1 \cdot e^{-\alpha_1 a} + D_1 \cdot e^{\alpha_1 a} \\
B_2 \cdot e^{\alpha_2 a} &= C_2 \cdot e^{-\alpha_1 a} + D_2 \cdot e^{\alpha_1 a}
\end{aligned}
\qquad (2.2.5)
$$

at $z = -a$. Next, we can apply equation (2.1.4) and the charge free condition $\nabla \cdot \mathbf{E} = 0$ to the field components to acquire the dispersion relations in three regions.

$$\alpha_j{}^2 = k_x{}^2 - k_0{}^2 \cdot \varepsilon_j \qquad (2.2.6)$$

for $j = 1,2,3$. Eliminating constants and solving this linear equation results in an implicit expression for the dispersion relation.

$$e^{-4\alpha_1 a} = \frac{\alpha_1/\varepsilon_1 + \alpha_2/\varepsilon_2}{\alpha_1/\varepsilon_1 - \alpha_2/\varepsilon_2} \cdot \frac{\alpha_1/\varepsilon_1 + \alpha_3/\varepsilon_3}{\alpha_1/\varepsilon_1 - \alpha_3/\varepsilon_3} \qquad (2.2.7)$$

In the limiting case of infinite separation between two metals (a → ∞), the left-hand side of (2.2.7) vanishes and the remaining right-hand side can be reduced into two equations resembling (2.1.9) which means the surface waves on this multi-layer system can be treated as two uncoupled SPP modes on the interfaces at $z = -a$ and $z = a$ individually. This again shows the localized nature of SPPs that no coupling could take place unless two modes are brought close together in the near field region ($a \sim \lambda$) where two exponentially decaying tails interact and start hybridizing into new modes.

To connect to the following chapter, we then focus our interest on a special case where the media of the substrate (region2) and the superstrate (region3) in the metal-dielectric-metal layered structure are of the same kind of metal, *i.e.* $\varepsilon_2 = \varepsilon_3$ and $\alpha_2 = \alpha_3$. In this case, the dispersion relation (2.2.7) can be simplified.

$$e^{-4\alpha_1 a} = \left(\frac{\alpha_1/\varepsilon_1 + \alpha_2/\varepsilon_2}{\alpha_1/\varepsilon_1 - \alpha_2/\varepsilon_2} \right)^2 \tag{2.2.8}$$

Taking the square root of (2.2.8) and solving resulting positive and negative roots gives rise to a pair of dispersion relations describing two hybridized modes in region 1.

$$\tanh(\alpha_1 a) = -\frac{\alpha_2 \varepsilon_1}{\alpha_1 \varepsilon_2} \tag{2.2.9a}$$

$$\tanh(\alpha_1 a) = -\frac{\alpha_1 \varepsilon_2}{\alpha_2 \varepsilon_1} \tag{2.2.9b}$$

It can be shown that the (2.2.9a) describes the modes of antisymmetric $E_x(z)$ component with respect to the middle of the dielectric layer ($z = 0$) whereas $E_z(z), H_y(z)$ are symmetric. On the other hand, (2.2.9b) describes the modes of symmetric $E_x(z)$ component while $E_z(z), H_y(z)$ are antisymmetric [13].

Chapter 3 Surface wave accelerator based on silicon carbide (SWABSiC)

3.1 INTRODUCTION

Charged particle accelerators are the foundation rocks of experimental high energy physics and can be utilized as practical applications, such as radiocarbon dating, synchrotron light source, and ion implanters in semiconductor industry. As technology develops along the advance of scientific research, pursuing higher accelerating gradient within compact footprint becomes a core mission of researchers. However, conventional accelerators, metal cavities driven by travelling microwave, are naturally limited by the electric breakdown and available peak power. Advanced accelerators entirely made of dielectric waveguides are proposed to mitigate this limitation and at the same time conserve institutional funds and space. Recently, one of such advanced accelerators which exploits the optical response of silicon carbide in the spectral range of commercially available high-power CO_2 laser is proposed and fabricated [14,15]. The surface wave accelerator based on silicon carbide (SWABSiC) utilizes a polar semiconductor, silicon carbide, that supports surface phonon polaritons (SPhPs) at SiC-vacuum interfaces in the *reststrahlen* band, where the dielectric permittivity of SiC, $\varepsilon_{\mathrm{SiC}}$, is negative according to the following formula:

$$\varepsilon_{\mathrm{SiC}} = \varepsilon_{\infty} \frac{\omega^2 - \omega_{\mathrm{L}}{}^2 + \mathrm{i}\gamma\omega}{\omega^2 - \omega_{\mathrm{T}}{}^2 + \mathrm{i}\gamma\omega} \tag{3.1.1}$$

Here $\varepsilon_{\mathrm{SiC}} = 6.7$ is the high-frequency dielectric constant, $\omega_{\mathrm{L}} = 970\mathrm{cm}$ ($\lambda_{\mathrm{L}} = 1/\omega_{\mathrm{L}} = 10.31\mu\mathrm{m}$), $\omega_{\mathrm{T}} = 794\mathrm{cm}$ ($\lambda_{\mathrm{T}} = 1/\omega_{\mathrm{T}} = 12.59\mu\mathrm{m}$) are the normalized frequencies of the longitudinal and transverse optical phonon frequencies, and $\gamma = 4.75\mathrm{cm}^{-1}$ stands for the damping constant [16]. The *reststrahlen* band is defined by $\omega_{\mathrm{L}} < \omega < \omega_{\mathrm{T}}$ which leads to $\mathrm{Re}[\varepsilon_{\mathrm{SiC}}] < 0$. It is important to notice that negative dielectric permittivity of SiC-vacuum interface plays an essential role in supporting the SPhPs modes on the interfaces. As described in the Chapter 2.2, two of such well-localized surface waves are free to couple to each other in near-field region when two SiC-vacuum interfaces are closely placed together with a subwavelength separation. In the case of the metal-dielectric-metal configuration, two individual SPhPs hybridized into two guided modes, classified according to the symmetry of the magnetic field component $\mathrm{H_y(z)}$ respect to the midplane of the accelerating channel in the vacuum gap, can interact with charged particle and therefore are referred as antisymmetric accelerating (longitudinal) and symmetric deflecting (transverse) surface modes.

The benchtop tests (cold test) of SWABSiC, including external-beam FTIR spectroscopy, numerical calculations, and data analysis, were performed and covered by the former group member, Burton Neuner, in his publication and dissertation. With these well-established results, the next step is to further examine the accelerating structure with relativistic electron bunches (hot test) which is the main body of this chapter. The most important aspect of the hot test is to power up the structure with high-power CO_2 laser pulses and synchronize the relativistic electron beam with longitudinal field component of the launched accelerating mode in the vacuum gap. Executing this challenging task requires years of effort on implementing hardware and software which cannot not be accomplished solely by a single group without any collective efforts. Our group collaborates with Accelerator Test Facility (ATF) in Brookhaven National Laboratory (BNL), where the state-of-art instrumentations and engineering supports are generously offered, to carry out the electron beam test of SWABSiC. During his PhD program, the author has made 4 on-site visits to ATF in BNL (Sep. 2014, Mar. 2016, Apr. 2017, and Feb. 2018). The results of the hot tests are analyzed and summarized in this chapter.

In this work, analytic theory was derived by Serguei Kalmykov, analytic method of Green's function was derived by Simeon Trendafilov and Vladimir Khudik, numerical simulation using Green's function was done by Tianhong Wang, GPT simulation was perform by University of California, Los Angeles collaborator Nick Sudar, and silicon carbide thin film growth was performed by University Claude Bernard Lyon I collaborator Gabriel Ferro. Two ATF runs prior to the author's visits were attended by Kamil Alici. Sample fabrication, metrology, and structure assembly machining were conducted by the author. Electron bunch test and data analysis were performed by the author with great help from staffs at ATF in BNL.

3.2 BEAM-DRIVEN EXCITATION WITH DENSITY MODULATED ELECTRON BEAM

One of the most promising incentives to choose SiC over other polar dielectric materials is the availability to access the negative permittivity in *reststrahlen* band with commercial high-power CO_2 lasers. However, the excitation method is not limited to direct laser pumping. In fact, a source of harmonic field modulations with the momentum matched to the surface modes in the correct configuration could be capable of powering up the SWABSiC. In particular, our group recently proposed a beam-driven scheme to excite the accelerating structure. This section is modified from the publication [17].

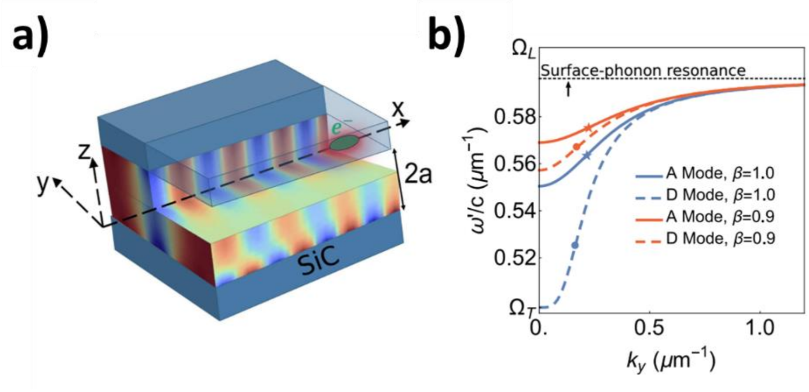

Figure 3.1 Cherenkov Radiation of SPhPs on SWABSiC. a) Schematic of electron passing through SWABSiC waveguide. b) Transverse dispersion curves of the accelerating (solid line) and deflecting (dashed line) modes that are synchronous with the electron bunches moving with $v = c$ (blue), and $v = 0.9c$ (red) velocities in the X-direction. Courtesy of Tianhong Wang.

Cherenkov radiation (CR) [18,19,20] is produced by a fast electron moving through a homogeneous medium with a velocity above the light threshold. Likewise, a single relativistic charge is shown to launch CR of SPhPs on SWABSiC (Figure 3.1).

To coherently excite the surface modes with CR, a periodic modulation in electron density is applied onto a driver bunch. In this study, a 51MeV electron beam with 300pC charge and 5ps duration propagating in positive X-direction is considered. The physical dimensions of the bunch are chosen to pass a flat aperture, 1-cm long accelerating channel of fabricated SWABSiC. Moderate density modulation with spatial periodicity of $\lambda_L = 11.4\mu m$ (as shown in Figure 3.2a) along X-direction is predicted to coherently produce surface waves. In Figure 3.2b, the increasing amplitude of oscillatory field can be readily interpreted as following, when driver bunch entering the accelerating channel, the leading part starts creating CR which is then gaining energy from the latter part of driver bunch. Electrons ride on these wakes can be either accelerated (red dots) or decelerated (blue dots) depending on relative phase of surface mode as shown in Figure 3.2c.

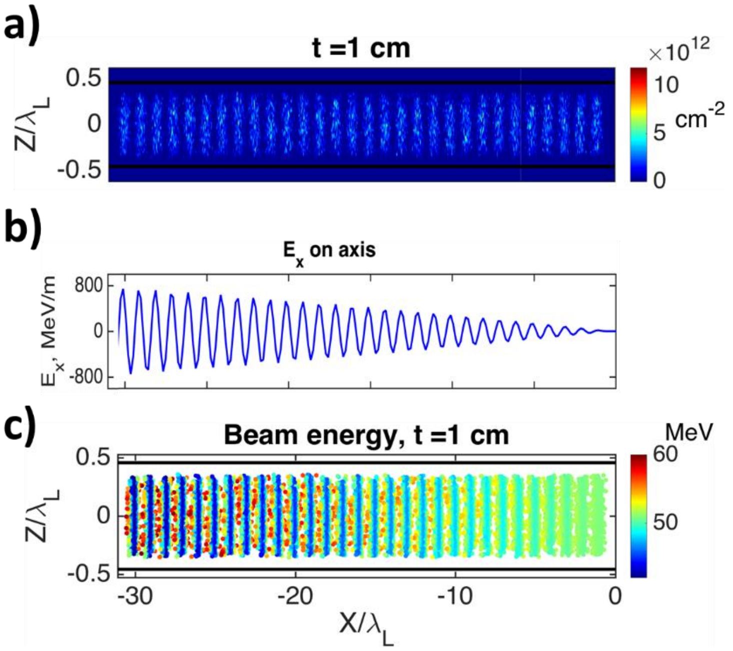

Figure 3.2 Density modulated electron bunch simulation. a) 2-D profile of electron density modulation. b) Longitudinal field component along the bunch length. c) Beam energy plot. Courtesy of Tianhong Wang.

As a result, broadened energy profile of the transmitted bunch in the Figure 3.3a indicates accelerated and decelerated of electrons from SWABSiC. One important observation is that the energy spectrum depends on the periodicity of density modulation. In the case of $\lambda_L = 10.3\mu m$ in Figure 3.3b, it is clear that energy spread is symmetric compared to the spectrum in Figure 3.3a. This obvious difference results from the fact that modulated electron beam stays in phase with surface modes at this wavelength. Therefore, most of the electrons loss energy to surface waves and are decelerated to lower energy. On the other hand, accelerated electrons gain more energy due to stronger longitudinal field component of surface modes. The simulation predicts a 9MeV maximum energy gain from single 1-cm acceleration length which equals to 900 MeV/m accelerating gradient.

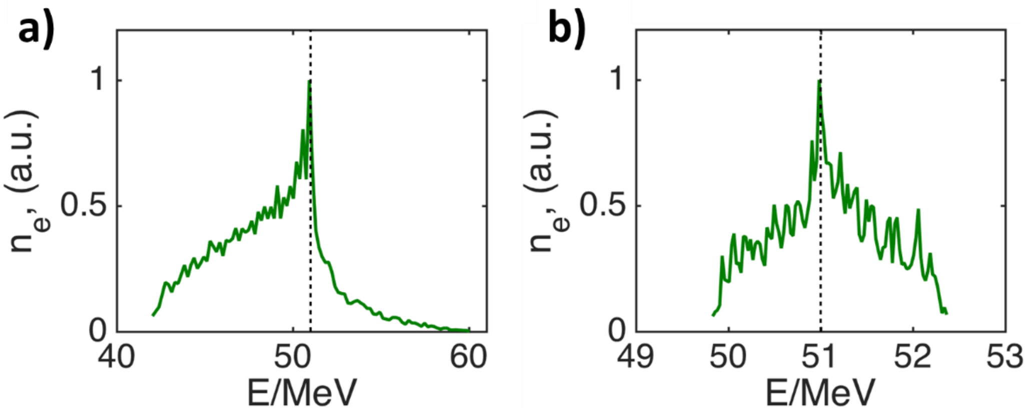

Figure 3.3 Energy profile simulation of transmitted electron. a) Density modulation with $\lambda_L = 11.4\mu m$. b) Density modulation with $\lambda_L = 10.3\mu m$ Courtesy of Tianhong Wang.

3.3 EXPERIMENTS IN ACCELERATOR TEST FACILITY

3.3.1 New Sample Fabrication and Holder Assembly

To perform the hot test of the SWABSiC with electron beam, a new sample is fabricated due to a technical difficulty in aligning the structure of the old prism-coupling. The challenge is the tight tolerance of angular alignment permitting the ballistic electrons to propagate through the narrow accelerating channel (~6μm) without entirely stopped by other part of the structure. On top of that, there is no aligning verification on neither the structure nor the sample assembly to facilitate the aligning process.

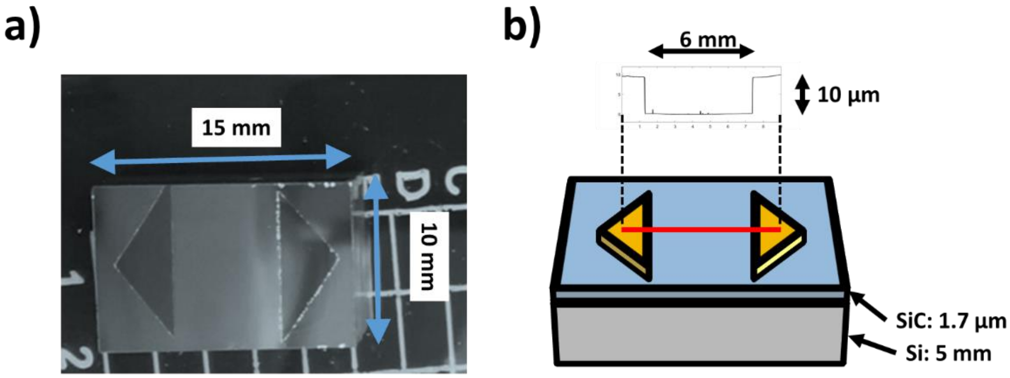

Figure 3.4 Newly fabricated piece of SWABSiC structure. a) Image of silicon brick with silicon carbide deposited on top. Two triangular patches are made of SU-8 photoresist. b) Schematic of the sample piece, yellow patches: gap spacer, cyan layer: silicon carbide thin film, gray brick: silicon substrate, red line: path of profilometer measurement. Inset: depth along the cutline showing the thickness of the spin-coated spacer.

A practical solution is employed by enlarging the gap size, though at the expense of the peak accelerating gradient, to ease out the physical limitation in the aligning process. While redesigning the dimensions of the structure, it is critical not to invalidate the working principle of the SWABSiC therefore one must separate two SiC-vacuum interfaces farther away in the mean while maintaining the mode hybridization. After evaluating the tradeoff, the gap size of the new design is set to 1.5-fold of the old sample (~10μm) which is sufficient to alleviate the difficulty of alignment without severe performance deterioration. In this sense, the previous experimental results, such as FTIR spectroscopy and angular resolved reflectivity measurement of table top CO_2 laser, evidently serve as the verifications for the existence of hybridized surface modes.

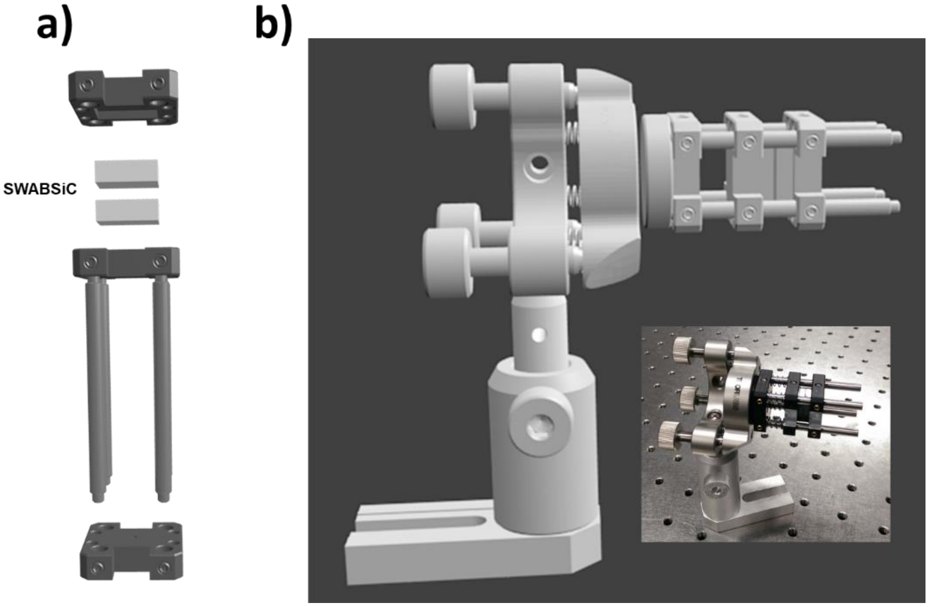

Figure 3.5 SWABSiC sample assembly. a) Schematic of sample holder. b) Schematic of sample assembly. Inset: photo of fully-assembled parts.

The newly fabricated sample was made from the similar processes as the old sample in the previous studies. A thin layer of silicon carbide (1.7μm) was grown on a rectangular silicon substrate (10mm × 15mm × 5mm) as shown in Figure 3.4. The 10μm vacuum gap between two SiC thin films was defined by spin-coated polymer spacers made of photoresist SU-8, which is chosen to withstand the acetone cleaning for complying the vacuum requirement in ATF. Likewise, another silicon substrate was fabricated with the same procedure but without the polymer spacers coated.

In Figure 3.5a, these two silicon bricks were then held against each other by two aluminum braces, modified from the commercial cage system plates, to form a narrow gap in between. The plates were firmly pressed together by four springs loaded at the bottom of the braces to ensure constant gap. The resulting sample assembly was then fixed onto a high vacuum compatible mirror mount (Polaris series from ThorLabs) to grant the capability to rough align the narrow accelerating channel in yaw and roll axis as shown in the Figure 3.5b. The SWABSiC structure is visually inspected for damage after the hot test with electron and CO_2 laser irradiance. No damage is found to exist after several runs experiment at ATF in BNL.

3.3.2 Beamline 2 Configuration at ATF in BNL

This section covers the beamline setup in the ATF. Our UCLA collaborators use the same beamline for investigating laser-electron interaction, such as helical IFEL [21], high efficiency energy extraction [22], and double buncher [23]. We follow the similar configuration in order to reproduce the electron-laser interaction result for generating the density modulated electron bunch. Therefore, the beamline configuration is briefly described for the sake of completeness.

Electron beam with energy from 45 to 70 MeV is prepared by the ATF LINAC using a 1.6 cell s-band gun and two SLAC LINAC sections. The output beam can be sent to one of three experimental beamlines through transport section, and various diagnostics such as strip-lines, pneumatic beam position monitors (referred as IPOPs in this study), and a Faraday cup are available for monitoring the beam. We installed the SWABSiC experiment in the Electron-Plasma Interaction Chamber on beamline 2, which is referred as I-line, where beamline already had optics for CO_2 laser transport from the previous users' experiments.

The beamline setup is shown in Figure 3.6. The electron is redirected onto the beamline 2 by a dipole magnet from the transport section. The CO_2 laser is delivered from the laser transport tunnel form the CO_2 laser room and focused by a NaCl lens prior injecting the vacuum system thru a high damage threshold NaCl window (not shown). The beamline is defined by two irises at the laser injection port and the end of beamline, and a HeNe laser is aligned to these reference points in order to align components to the beamline. On the other hand, the final CO_2 alignment iris and lens are located roughly 4.5 m upstream of the pre-buncher. In order to align the CO_2 laser to the beamline within the pre-buncher, the laser is kicked out from the beamline to a rail by a mirror mounted in IPOP3. The irises on the rail in the focal region are aligned to the beam line HeNe, and the CO_2 (imaged with the Pyrocam) is coaligned to these irises using the Picomotor controlled mirror near the final focusing lens. Note that to avoid collision with chamber installation, IPOP6 and IPOP7 are disabled by mechanically stopped with copper gaskets.

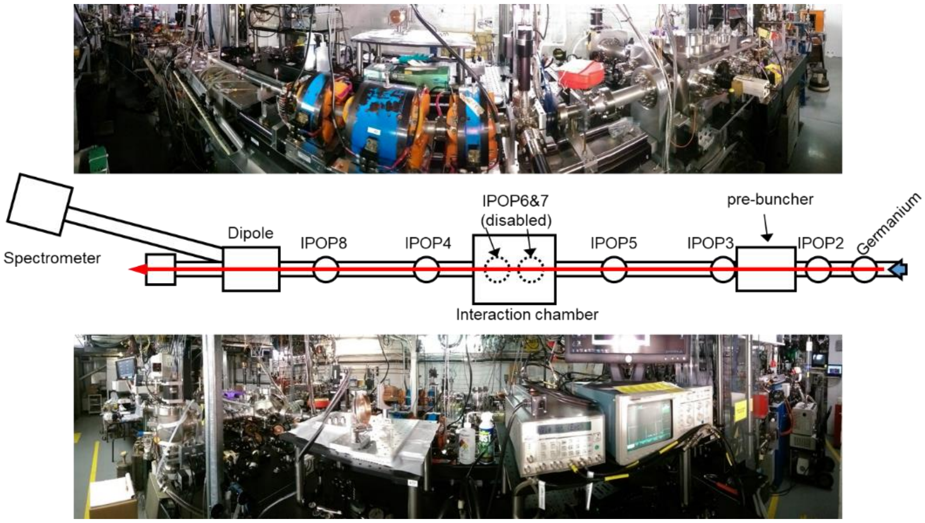

Figure 3.6 Schematic and photos of beamline 2 configuration at ATF. Electron beam propagates from right to the left. Red arrow: a HeNe laser used for beamline alignment. Note that IPOP6 and IPOP7 are disabled.

3.3.3 Installation in Interaction Chamber on Beamline 2

The chamber installation is shown in the Figure 3.7. A phosphor screen is setup for monitoring the shape of beam spot at the sample position since both IPOP6 and IPOP7 are disable due to space conflict. An imaging system consisting of an objective (10X Plan Apo Infinity-Corrected Long WD, Mitutoyo), a mirror, and a camera (COHU 4920) with TV lens (75mm f/1.4 C-mount) outside of the chamber (not shown) is established to image the phosphor screen. The sample assembly and the screen are mounted on a translation stage moving in the transversal direction to the beam axis for switching the target between screen, sample, and beam clear (free space) on the stage.

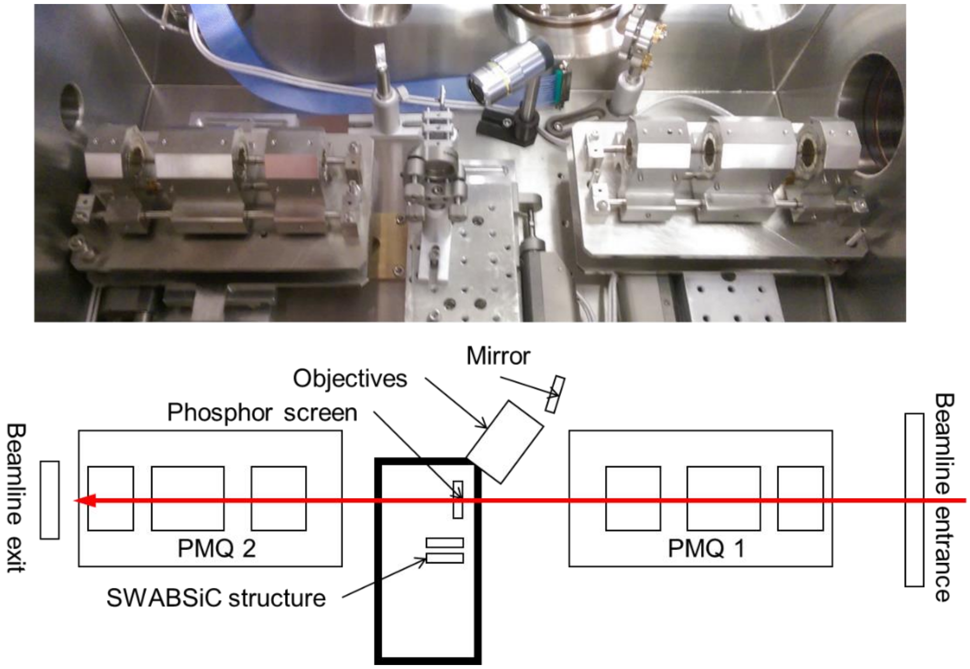

Figure 3.7 Photo and schematic of chamber installation of SWABSiC experiment.

In order to propagate the electron beam through SWABSiC, a permanent magnetic quadrupole (PMQ) mini-triplet from Radiabeam [24] is employed to shape the electron beam spot according to the narrow accelerating channel of the structure. To reach the tightest focus spot available, the mini-triplet is position ~14.6 mm upstream to SWABSiC structure. The other identical PMQ is used to de-focus the divergent beam so that the electron bunch can reach the spectrometer instead of losing in the beam pipe. Note that the direction of PMQs is facing opposite to each other. Likewise, both triplets are mounted to translation stages so one can retract all components in the chamber for initial electron beam alignment. The transmission rate for the charge is around 5% after all the beam tuning and dispersion correction.

3.3.4 Hot Testing SWABSiC at ATF in BNL

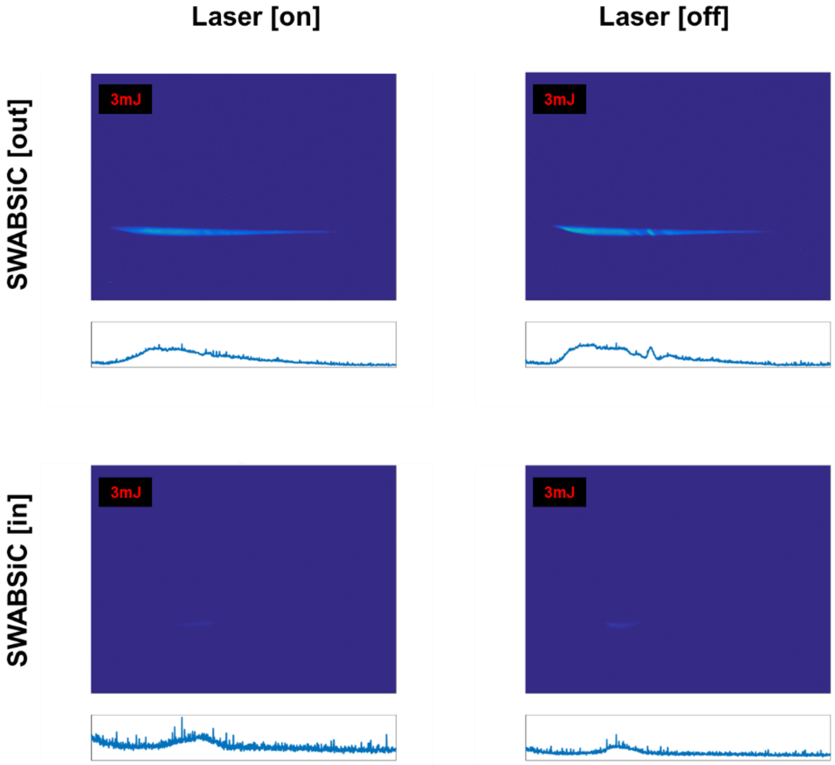

Figure 3.8 Full set of measurement taken at laser power 3mJ. The energy profile below each spectrometer image is the pixel sum of the vertical direction.

During the hot test of SWABSiC structure, the sample was tested with micro-bunched beam prepared in UCLA pre-buncher together with a $10.3\mu m$ CO_2 laser pulse. The energy spectrum of the transmitted electron bunch is measured. A set of measurement consists of with/without SWABSiC structure and laser on/off totaling 4 different cases as shown in Figure 3.8. The same set of measurement is repeated at different laser power level to study the dependence of bunching factor.

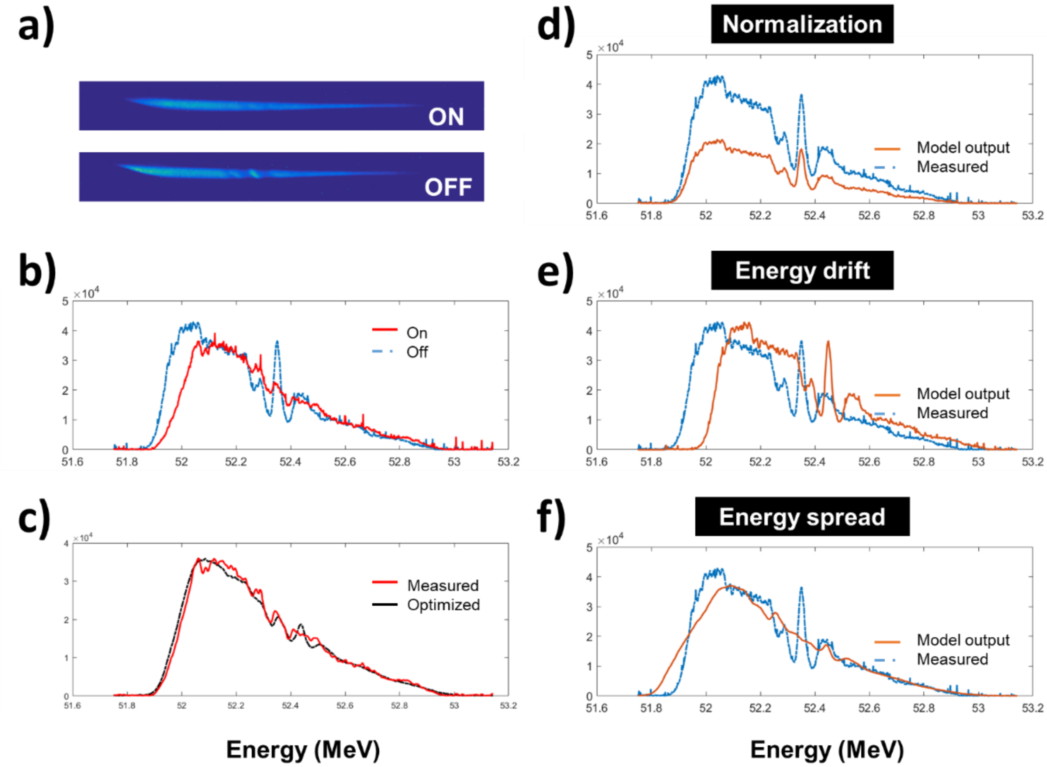

Figure 3.9 Model optimizing for measurement without structure. a) spectrometer images for laser on/off. b) energy profile. c) optimized spectrum by the model. Model out puts of only d) normalization. e) energy drift. f) energy drift.

In order to observe the effect of SWABSiC, it is crucial to remove two undesired contributions to energy spread, which are the intrinsic energy profile generated from the gun and energy modulation of micro-bunching effect as Figure 3.9a. This data processing is done with following steps.

First, the image of spectrometer is pixel summed to a single energy profile. The resulting spectrum measured through free space without SWABSiC is considered as a set of control experiments for extracting the parameter of energy spread from a phenomenological model. The spectrum taken without bunching effect, namely laser is not injected in the beamline, is used as a baseline of intrinsic energy profile (blue dashed curve). On the other hand, the spectrum recorded with laser injected (red curve) into the beamline is certainly broader than the baseline due to the energy modulation imprinted by CO_2 laser inside the pre-buncher as shown in Figure 3.9b.

Next, the said model is employed to account for this broadening by intentionally imposing a prescribed energy spread to the baseline spectrum. This model assumes 3 parameters, energy drift, normalization factor, and most importantly energy spread as shown in Figure 3.9d, e, and f. With these inputs, the model subsequently generates a broadened spectrum based on a baseline profile. These parameters are determined when the discrepancy between measured and emulated spectrum is minimized as shown in Figure 3.9c. Note that the first two parameters are included to remove the shot-to-shot variation since the electron energy and charges are all different in every shot due to stochastic nature of the photoemission. Furthermore, the offsetting and scaling to a spectrum do not change the “spreading” of the energy profile so the parameter of energy spread will be properly constrained and then extracted from this optimization process. This step is performed iteratively in Matlab. The resulting parameter of energy spread is readily to be used to account for the broadened spectrum with micro-bunching effect. Note that this optimizing process is repeated for all combinations of the spectra with and without laser injection. For instance, if there are 8 repeated measurements without laser and 7 repeated measurements with laser, total 56 energy spread values will be determined from the process. Then the final value at certain laser power is represented by the averaged value with standard deviation as error bar as shown in Figure 3.10a. Finally, spectrum measured with electron passing through SWABSiC structure enters in the picture. Similarly, the spectrum measured without micro-bunching is used as baseline and the energy spread factor is again extracted from the same optimization procedure. The resulting parameters are statistical represented as shown in Figure 3.10b.

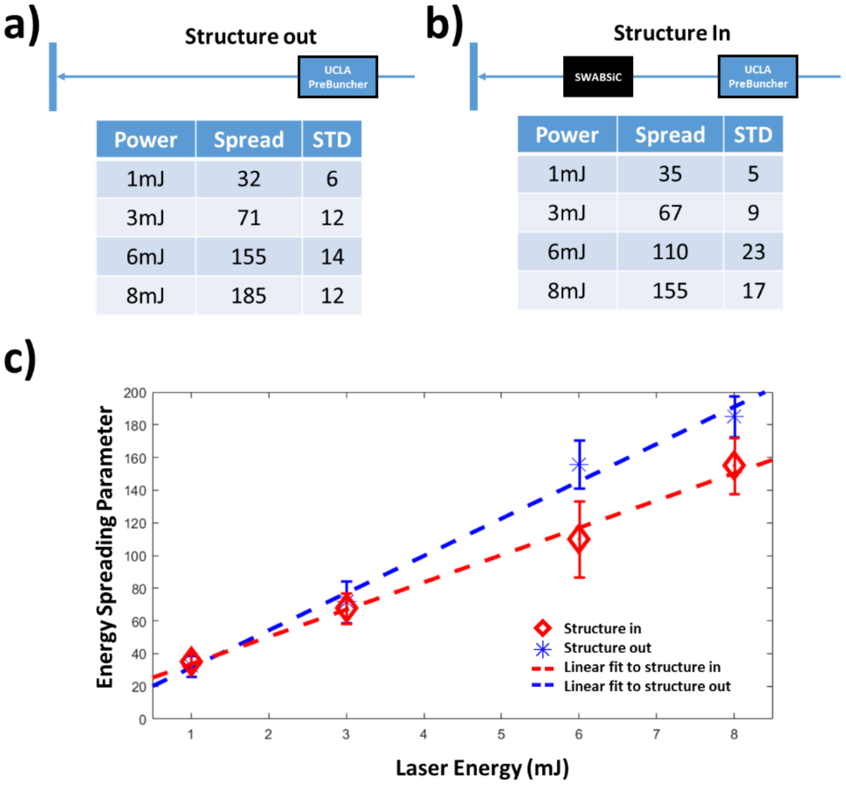

Power	Spread	STD
1mJ	32	6
3mJ	71	12
6mJ	155	14
8mJ	185	12

Power	Spread	STD
1mJ	35	5
3mJ	67	9
6mJ	110	23
8mJ	155	17

Figure 3.10 Result of phenomenological model optimizing. Energy spread parameter extracted from a) without structure and b) with structure c) Power dependent energy spread parameter. Blue star: without structure, red diamond: with structure, dashed line: linear fit of the scatter points.

The energy modulation induced on the electron beam is linearly dependent on laser power in this low power range and the curve fitting result is plotted to show this linear dependence. Hence, one can spot the effect of SWABSiC by comparing the energy spread with and without SWABSiC as shown in the Figure 3.10c. It turns out that the energy spread with SWABSiC is actually narrower than it is without the structure. We speculate this is due to the detuning of wavelengths between modulated electron beam and surface modes of SPhPs. The lower spread might result from the low transmission rate of the charge that the high energy electron is blocked at the entrance of the narrow accelerating channel where the dispersion is not compensated thus the spatial position is correlated to electron energy.

Therefore, we propose switching wavelength of CO_2 laser oscillator to match 10P line ($10.6\mu m$) or other branches with even longer wavelengths in regenerative amplifier. Certainly, drawback of this change is severe. For instance, instead of a single pulse in time domain, a train of multiple pulses with 18 ps spacing will be generated due to inverse-Fourier transformation of discrete lines in P-branch. In addition, this pulse splitting also decreases laser's peak power. Although the price is huge, it is crucial to operate at or close to wavelength of SPhPs to correctly excite SWABSiC.

3.4 SUMMARY AND COMMENT

The idea of advance accelerator concepts is much desired in future development. The SWABSiC is one of the promising platform to be used for higher accelerating gradient with compact size and high damage threshold. Moving forward from the previous development done by former group member, the author reviews the basic idea of such a platform together with new simulated predictions and on-site experimental results at ATF in BNL in this Chapter. The hot tests demonstrate the feasibility of using such a structure to withstand high power laser and the damage of electric discharging. The performance, however, deviates from the theoretical expectations which is largely due to the wavelength detuning of the CO_2 laser at ATF. Future test with correct wavelength of laser is expected to improve the performance of the accelerating structure.

Chapter 4 Photonic Topological Insulator

4.1 PHOTONIC CRYSTALS

4.1.1 Photonic Crystals and Bloch Waves

Much alike the surface waves at the interfaces between dissimilar homogenized media with no discrete periodicity in the preceding chapters, the surface waves can also be found in the photonic crystals (PCs), a medium of periodically modulated refractive index with the periodicity comparable to the wavelength, *i.e.* $a_0 \approx \lambda$ where a_0 is the primitive vector of the crystal and λ is the wavelength of the electromagnetic wave.

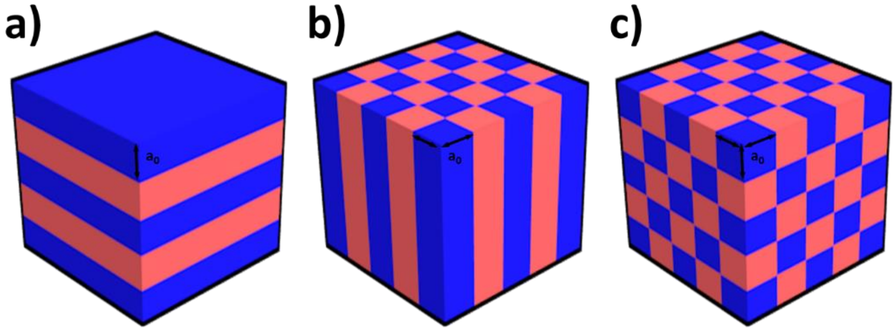

Figure 4.1 Examples of photonic crystals with periodicity $a_0$in different dimensions. a) a stack of slabs as 1D PCs. b) a wire or uniaxial medium as 2D PCs. c) a cubic lattice of bricks as 3D PCs. Red and blue domains are the media of different refractive index.

As shown in the Figure 4.1, the simplest example of a one-dimensional (1-D) PC is a stack of alternating materials with periodicity a_0 along the normal direction of slabs. A 2-dimensional (2-D) PC consists of a periodic 2-D array of materials in the transversal plane and is often referred as uniaxial or wire medium. In the same manner, a 3-dimensional 3-D PC are periodic in all three spatial dimensions. Note that this figure merely serves as examples of possible PCs and is by no means an exhaustive library. In fact, one can use different periodicity, geometrical shape, or even the type of lattice to engineer desired property of PCs.

Instead of directly solving the Maxwell's equations for the arrays of identical unit cells, it is beneficial to adopt the well-established methodology in the solid-state physics, namely the Bloch theorem, which deals with electrons propagation in a periodic potential structure made of atoms. For the sake of brevity, the conceptual constructs of solid-state physics are directly adopted with photonic analogues and rephrased in plain language in this dissertation. Reader of interest are recommended to resort to classic textbooks [5] for rigorous definitions and detailed derivations.

The critical point to make this connection is to massage the Maxwell's equations into an eigenvalue system so the Bloch theorem can be readily applied in the photonic systems. Starting from the Maxwell wave equations, it is shown that steady state of EM waves can be reduced to an eigenvalue problem of magnetic field with photon operator resembling the Hamiltonian in Schrodinger's equation for electron. With cyclic boundary condition specified by the choice of unit cells, the Bloch theorem can be readily applied to the photonic systems. This analogy not only reduces the calculation burden on computers but also provides insights to understand the seemingly complicated photonic systems with instinctive picture.

The Bloch wave construct is briefly presented here in the layman's language using a hypothetical solution of 1-D PC in the Figure 4.2. The gist of the derivation is to separate the periodic part of the full solution $\Psi(x)$ using the ansatz of exponential function e^{ik_1x}, where k_1 is the wavevector of the assume. The remaining function $u_1(x)$ is the local field solution with the same periodicity as the lattice such that the full solution can be expressed as $\Psi(x) = e^{ik_1x} \times u_1(x)$. Therefore, one can concentrate mainly on the collective phenomenon of the crystal, namely e^{ik_1x}, rather than the identical local field of individual unit cells. It is not surprising to find out that this ansatz is of the same mathematical form of a plane wave propagating in a homogeneous medium because the local field profile is a constant due to miniscule or lack of the explicit periodicity. It might seem to the readers that the function $u_1(x)$ has no physical significance whatsoever, but the local field in fact is of great importance while determining the frequency of Bloch waves. Furthermore, one can tailor novel photonic devices by exploiting the properties of the local field which will be presented in the later chapters.

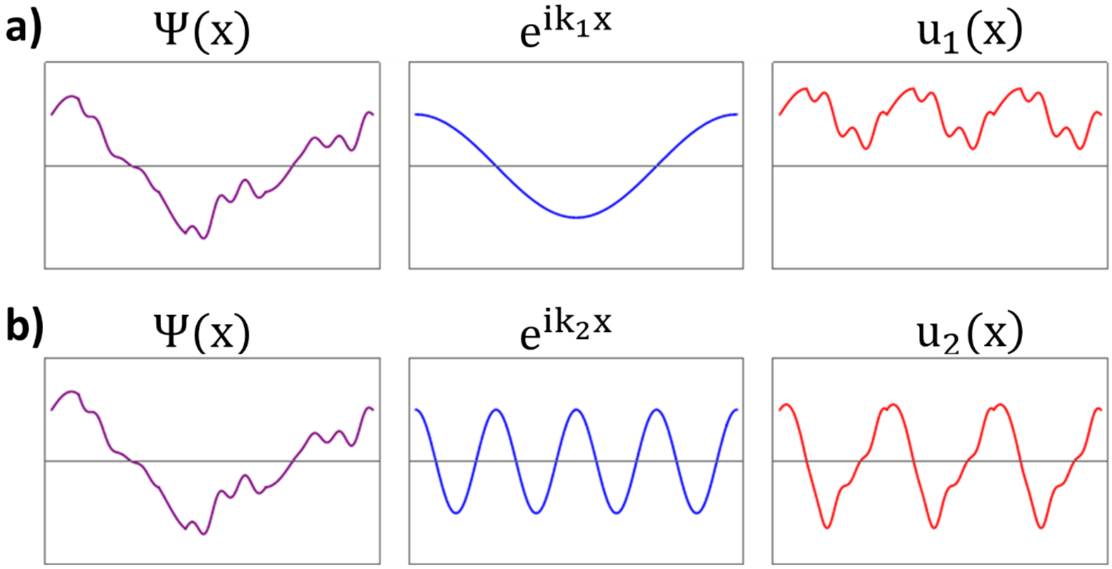

Figure 4.2 Schematic of Bloch wave decomposition in the solution of a 1-D photonic crystal. Purple: full solution, blue: plane wave, red: local field for the case of a) using an arbitrary reciprocal vector k_1. b) using reciprocal vector k_2 with the relation $k_2 - k_1 = G$, where G is the reciprocal lattice vector.

Like the counterpart in the solid-state physics, the Bloch wave in photonic system is also characterized by a reciprocal wavevector k in periodic Brillouin zone (BZ) and the dispersion relation of this wave is referred as the photonic band structure (PBS) of the photonic system. It is worth noting the fact that the way of decomposition is not unique. In

Figure 4.2b, it is obvious that the full solution can also be fully described by the other wavevector k_2 which differs from k_1 by an integer multiplied by the reciprocal lattice vector G, *i.e.* $\mathrm{k}_2 - \mathrm{k}_1 = \mathrm{nG}$ where n is any integer number. Using this fact, we could narrow the scope down to the first Brillouin zone (FBZ) because the dispersion curve at large wavevectors can be folded back as a higher order band in the FBZ which is often termed as band folding in the field.

By altering material property, geometry, periodicity or even topology of the unit cells, one could control the dispersion of the Bloch waves and thus access effects which could not be easily found in the continuous medium, such as slow light, super-prism, hyperbolic dispersion, and negative refraction. Particularly, one crucial feature among them is a forbidden region in the photon energy, also known as the photonic band gap (PBG), where no wave can propagate along certain directions. This could be understood as the destructive interference of the coherent back-scattering from unit cells when Bragg condition is satisfied at the boundary of the Brillouin zone. In the case of the bandgap spanning in all the directions, this spectral region is commonly referred as a complete photonic bandgap. The existence of this complete PBG plays an essential role in the emerging field, topological photonics, which will be covered in the following chapters.

4.1.2 Surface States in Photonic Crystals

In the physical system in the real world, nothing can extend to the infinite although a good approximation can usually be made when the irrelevant dimension is much larger than the system of interest. In the case of PCs, the periodicity of crystal is assumed to repeat without any termination which means the crystal size is infinitely large. While it is a good approximation in the center of the bulk, it is not a valid assumption in the proximity of the termination. The boundary of a crystal inevitably violates the periodic presumption of Bloch theorem and subsequently gives rise to the surface states in PCs. Under the proper termination of the periodicity as well as the unit cells, one can engineer a guided surface states in photonic systems at the interface between the crystal and the other medium as shown schematically in Figure 4.3. Making the analogy to the Tamm states in the solid-state physics where the guided surface modes in photonic crystals can be interpreted as the optical Tamm states [25,26] at the boundary. With the Bloch wave construct in mind, it becomes clear that the enveloping packet of surface waves in PCs are the same as the surface waves in the continuous medium, where the field is localized at the interface with exponentially decaying tails into both media.

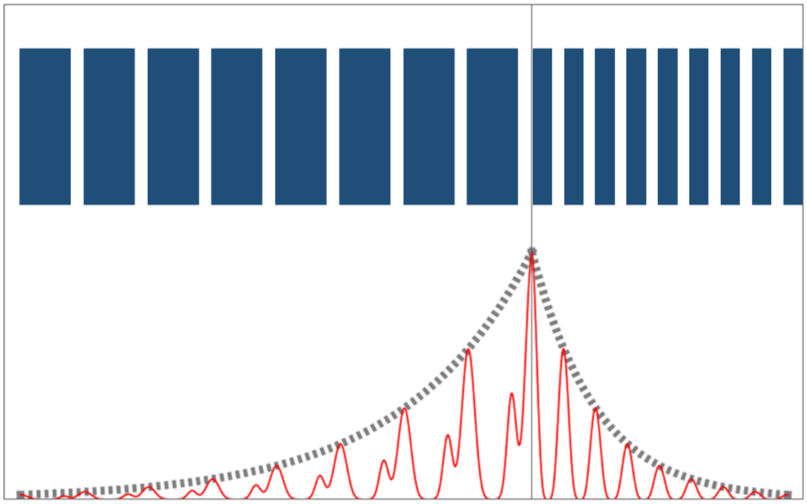

Figure 4.3 Conceptual illustration of a surface wave at the boundary between two dissimilar 1-D PCs made of the same material. Red curve: intensity of the EM waves, Gray dashed curve: exponential decaying envelope of a surface wave, indigo region in the inset: medium with high refractive index.

Despite from the severe termination which creates circumference of the crystal, there is a minor class of disruption to the crystal periodicity which could result in the so-called defect states in the bulk. As shown in Figure 4.4, these defects take place in a lower dimension compared to the dimensionality of PCs. For instance, the point (0-D) or line (1-D) defects in a 2-D PC are straight forward to visualize whereas a plane (2-D) defect is plainly not feasible in a 2-D PC. Depending on the how these imperfections of crystal are formed, the defects could behave as cavities, scatters or even waveguides for the propagating EM waves in the PCs. In fact, these modes are in close relation with the surface modes at the boundary, but the detailed discussion of defect modes is certainly beyond the scope of this introduction.

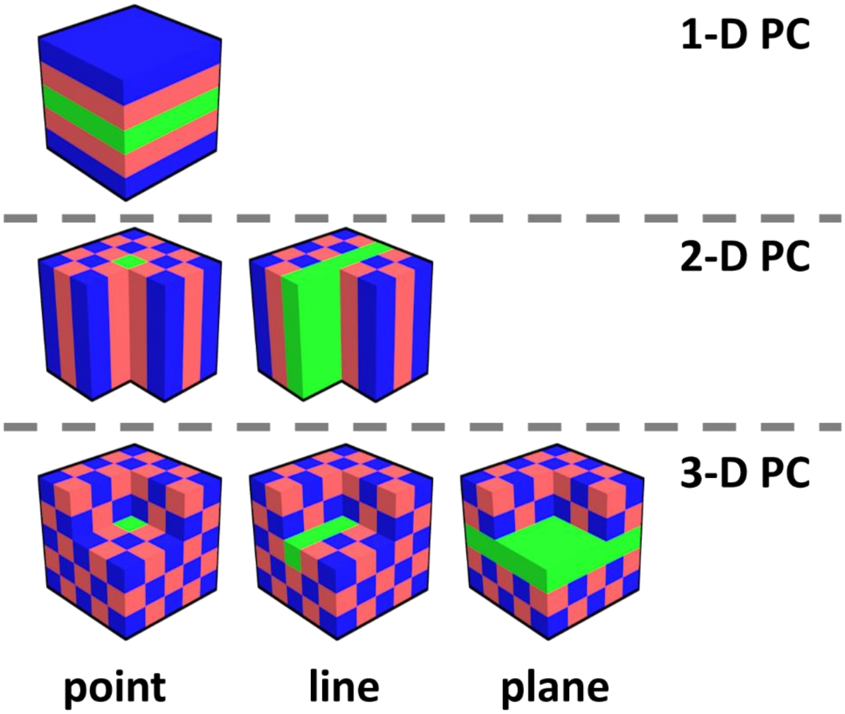

Figure 4.4 Examples of crystal defects in PCs of different dimensions. Green region: site of crystal defect where the possible imperfections are the discrepancy of physical dimension, material properties or even topology.

4.2 TOPOLOGICAL PHOTONICS

4.2.1 Brief Introduction to Topological Insulator

Topology, the mathematical concept dealing with quantized invariant under continuous deformation, is often introduced with a famous example: a donut and coffee cup with handle. These two utterly different objects fall into the same category of topology if one counts the number of holes, or genus of a solid, which is a topological invariant. In other words, one can continuous deform a donut-shaped solid into a coffer cup without creating or closing holes since they both have only one hole. Counterintuitively, a teapot, which shares similar utility and shape with a coffee cup in everyday life, is drastically different from the cup in a topological point of view because there are two holes, spout and handle, on the teapot. In addition, this daily example can take a step further to convey the quantized nature of the topological invariant since the number of holes are always an integer and can only be changed discretely, *i.e.* there is no one-and-a-half hole category between a donut and a teapot. As a result, physical features result from topological invariant are robust against perturbations which consist of continuous deformation or do not change the topology of the system.

One of such examples is the quantum Hall (QH) effect [27,28], in which the topological protection manifests as a robust quantized plateau-like growth of Hall resistance with increasing perpendicular magnetic field for a 2-D electron gas at low temperature. Specifically, the heights of these steps result from the topological invariant of the system and are independent of the sample parameters, for example, the size, the shape, and the charge carrier density. This phenomenon can be understood with following physical picture:

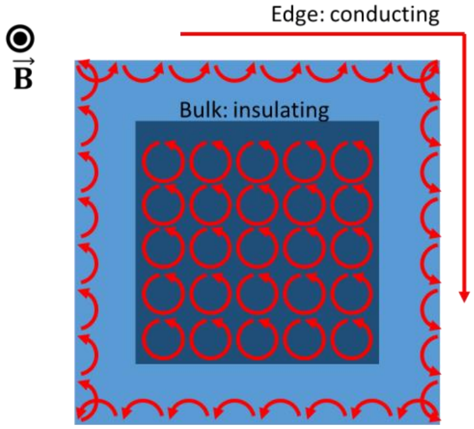

Figure 4.5 Classical image of electron transport in the case of quantum Hall effect.

Under the perpendicularly applied strong magnetic field to, the electrons are subject to move along circular orbits resulting in the insulating phase of the bulk 2-D electron gas whereas the orbits are terminated half-way by the edge of the system and possess transport as in Figure 4.5. The broken time-reversal symmetry by applying magnetic field means that electrons have no time-reversal partner (going backward) at the same energy. As a result, these edge state cannot be backscattered by impurity or defect and thus robust wave transport result from topological invariant.

Under the effect of magnetic field, the band structure of the electron is split into highly degenerate Landau levels separating by bandgaps. The edge transport only exists when the Fermi-energy of the electron is at these bandgaps and therefore the Hall resistance remains a plateau. When the magnetic field starts increasing, the Landau levels shift to overlapping with the Fermi energy and a step-jump in Hall resistant happens. As the strength keeps going, the Fermi energy snaps back in the bandgap where the conducting edge states emerge again. The correlation between the edge states and the topological invariant is reflected in the extremely robust step-height of the measured Hall-resistivity. It is then clear that the a QH effect system is a topological insulator.

Surprisingly, this effect could be present in utterly different system when the quantum spin Hall (QSH) effect is theoretically predicted and experimentally observed in graphene-based platform [29,30,31,32,33,34]. A different manifestation of this effect is predicted by opening the bandgap without applying external magnetic field. Combining the next-nearest neighbor hopping with a local periodic modulation of the magnetic field, the degeneracy lifts at the Dirac points and leads to the chiral edge states. The concept of the existence of chiral edge states without external magnetic field is proposed by Kane and Mele [32]. Without breaking the time-reversal symmetry, the chiral edge states can exist under certain condition when strong spin-orbital coupling is present.

4.2.2 QSH effect on Photonic Graphene

A 2-D photonic crystal with triangular or hexagonal lattice possessing the dispersion relation is often referred as a photonic graphene. One critical factor to emulate the photonic analogue of the QSH effect is to tailor the spin-orbital coupling on the photonic graphene. This seems to be counter-intuitive due to very different nature of photons compared to that of electrons. As shown by the study [35], the spin can be engineered from a metamaterial with duality relation: $\hat{\varepsilon} = \hat{\mu}$, where $\hat{\varepsilon}$ and $\hat{\mu}$ is the constituent permittivity and permeability of the in-plane Bloch wave propagation respectively. The linear combination of TE and TM modes are doubly degenerate and can be considered as spin states. Note that each of the two spin states is doubly degenerate at the K(K') point forming a 4-fold degeneracy owing to the hexagonal symmetry of the crystal. This degeneracy can be interpreted as orbital because two of the doublet can be linearly combined into a clockwise (right circular polarized, RCP) and counterclockwise (left circular polarized, LCP) rotating state.

By introducing the bi-anisotropy in the magneto-electric tensor to mix the TE and TM modes and thus the spin-orbital coupling in a photonic system. The four-fold degeneracy is lift and a finite size topological bandgap emerges at these Dirac points and the metacrystal becomes a photonic analogue of topological insulator. Starting with the eigen wave function of the Bloch wave, one can write down an effective photonic Hamiltonian of the system using the circular polarized (CP) basis which takes the same form of the Kane-Mele Hamiltonian for the spin-orbital coupling in graphene. Therefore, this system can be interpreted as the photonic topological insulator (PTI) hosting the photonic analogue of QSH effect. Specifically, the edge states can be shown to exist from bulk-edge correspondence as well as confirmed by the numerical simulations. Similarly, the wave transport is demonstrated to be robust and defect-immune which envisions the prospect of using the platforms designed from this methodology to emulate various electronic topological phases and to further investigate the effects that are hardly accessible in condensed-matter systems.

An alternative platform designed from the same principle with relaxed restriction of the duality relation is introduced in the next chapter and the topologically protected edge waves (TPEWs) are experimentally demonstrated.

Chapter 5 Quantum Sin Hall Photonic Topological Insulator

5.1 INTRODUCTION TO QSH PTI PLATFORM

5.1.1 Brief Recap of QSH PTI Design

An alternative PTI platform emulates the QSH effect by introducing a photonic analog of spin-orbital interaction using bianisotropic metamaterials, as well as uniaxial or bianisotropic metawaveguides (BMW). The spin degree of freedom can then be interpreted as the phase relationship between TE and magnetic TM modes of the metamaterial – in-phase for the spin-up and out-of-phase for the spin-down states.

The theoretical ground of this PTI platform has been firmly established by the former group member, Tzu-Hsuan Ma, in his pioneer works [36,37]. For the sake of brevity, this section only recaps the core design principles of the QSH PTI and provides theoretical background knowledge for paving the way to understanding the experimental realization of this platform in later sections. Some of the simulations are reran by the author to better explain the specific topics in this dissertation. Readers are advised to consult Ma's original publications as well as the supplemental materials for detailed derivation[1].

Firstly, we consider an unperturbed PC design, the so-called photonic graphene [38,39], which is a parallel-plate metal waveguide filled with a periodically arranged hexagonal array of metallic cylinders connected to both metal plates. The periodicity of the lattice guarantees the Dirac cones at the K/K' edges of the BZ for decoupled TE and TM modes respectively. By carefully choosing the separation between metal plates and the diameter of cylinders, the eigenfrequencies of TE and TM modes of the Bloch wave can be found doubly degenerate in the vicinity of the Dirac points [40]. Such mode degeneracy is essential for tailoring the spin degree of freedom based on the linear combinations of TE and TM modes that can be coupled to each other by a bianisotropic perturbation of the unit cell. The classic Slater theory [41], which describes the mode modification of a EM cavity by boundary perturbation, together with a degenerate perturbation theory [42] developed for nonreciprocal photonic crystal supporting a doubly degenerate TM mode are employed to analytically address the bianisotropic perturbation of the photonic graphene.

---

[1] The content of this chapter is modified from a prior publication: Lai, K., Ma, T., Bo, X., Anlage, S. and Shvets, G., "Experimental Realization of a Reflections-Free Compact Delay Line Based on a Photonic Topological Insulator". *Scientific Reports* **6**, 28453 (2016). T+he author designed, fabricated, assembled, conducted experimental measurements and contributed to manuscript writing.

Secondly, we calculate perturbed eigenfrequency ω' from the eigenvalue equation near the Dirac crossings at K point with the linearly polarized (LP) basis of TE and TM eigenmodes with the complex-valued amplitude: $\boldsymbol{a}_e = \left[a_{e_-}; a_{e_+}\right]$ and $\boldsymbol{a}_m = \left[a_{m_-}; a_{m_+}\right]$, where ‘e’ (’m’) refers to TE (TM) and ‘+’ (‘-‘) refers to the band with positive (negative) group velocity. Then the perturbation analysis indicates that by shortening the cylinders to create an air gap between the rod and the plate, the Z-inversion symmetry of the unit cell is broken by this asymmetrical gap. Subsequently, the doubly degenerate Dirac points are destroyed and a complete photonic bandgap appears at the same frequency. At the same time, this air gap provides bianisotropic coupling (Δ_{em}) which relates the phases between TE and TM modes.

$$\begin{bmatrix} \omega_{\mathrm{e}}(1+\Delta_{\mathrm{ee}})\hat{\mathbf{I}} - \mathrm{v}_{\mathrm{D}}|\delta\mathbf{k}|\hat{\boldsymbol{\sigma}}_{\mathrm{z}} & -\omega_{\mathrm{e}}\Delta_{\mathrm{em}}\hat{\boldsymbol{\sigma}}_{\mathrm{y}} \\ \omega_{\mathrm{m}}\Delta_{\mathrm{em}}\hat{\boldsymbol{\sigma}}_{\mathrm{y}} & \omega_{\mathrm{m}}(1+\Delta_{\mathrm{mm}})\hat{\mathbf{I}} - \mathrm{v}_{\mathrm{D}}|\delta\mathbf{k}|\hat{\boldsymbol{\sigma}}_{\mathrm{z}} \end{bmatrix} \times \begin{bmatrix}\mathbf{a}_{\mathbf{e}} \\ \mathbf{a}_{\mathbf{m}}\end{bmatrix} = \omega' \begin{bmatrix}\mathbf{a}_{\mathbf{e}} \\ \mathbf{a}_{\mathbf{m}}\end{bmatrix} \tag{5.1.1}$$

where $\delta\mathbf{k} \equiv \mathbf{k} - \mathbf{K}$, $\omega_{\mathrm{e(m)}}$ is the eigenfrequency at the Dirac point for TE (TM), v_{D} is the group velocity, Δ_{ij} (i, j= ‘e’ or ‘m’) is the perturbation strength determined by the overlapping integral of the fields, $\hat{\boldsymbol{\sigma}}_{\mathrm{x}}, \hat{\boldsymbol{\sigma}}_{\mathrm{y}}, \hat{\boldsymbol{\sigma}}_{\mathrm{z}}$ are the Pauli matrices, and $\hat{\mathbf{I}}$ is a 2×2 unity matrix.

Thirdly, the left circular polarized (LCP) and right circular polarized (RCP) basis (spin basis) is introduced to better formulate the system with a such phase relation. After the change of basis, there is an apparent possibility to minimize the hybridization of LCP and RCP modes by carefully choosing the strength of bianisotropic perturbation. Once the inter-spin scattering (modes hybridization) is fully suppressed, the eigenvalue equation is then expressed in a block-diagonal form with spin basis and dressed eigenfrequency $\omega'_\mathrm{D} = \frac{1}{2}\big(\omega_\mathrm{e}(1+\Delta_\mathrm{ee}) + \omega_\mathrm{m}(1+\Delta_\mathrm{mm})\big)$. Hereafter, one can interpret the spin DOF of photons as the phase relation between TE and TM where the spin-up (spin-down) corresponds to the electric field in-phase (out-of-phase) with the magnetic field and the orbital DOF as the handiness (phase shift between two LP components).

$$\begin{bmatrix} \mathrm{v_D}\delta\mathbf{k}\cdot\boldsymbol{\sigma} + \omega_\mathrm{D}\Delta_\mathrm{em}\hat{\boldsymbol{\sigma}}_\mathrm{z} & \mathbf{0} \\ \mathbf{0} & \mathrm{v_D}\delta\mathbf{k}\cdot\boldsymbol{\sigma} - \omega_\mathrm{D}\Delta_\mathrm{em}\hat{\boldsymbol{\sigma}}_\mathrm{z} \end{bmatrix} \times \begin{bmatrix} \boldsymbol{\psi}_\mathrm{K}^{\uparrow} \\ \boldsymbol{\psi}_\mathrm{K}^{\downarrow} \end{bmatrix} = \Omega \begin{bmatrix} \boldsymbol{\psi}_\mathrm{K}^{\uparrow} \\ \boldsymbol{\psi}_\mathrm{K}^{\downarrow} \end{bmatrix} \tag{5.1.2}$$

where $\boldsymbol{\sigma} = \left(\hat{\boldsymbol{\sigma}}_x + \hat{\boldsymbol{\sigma}}_y\right)$, $\boldsymbol{\psi}_\mathrm{K}^{\uparrow(\downarrow)}$ is the spin-up (spin-down) state of circular polarized light, and $\Omega = \omega' - \omega'_\mathrm{D}$ is the detuning from the dressed Dirac frequency.

Lastly, we expand the space of the resulting photonics states to include the both K and K' points of the BZ. The effective Hamiltonian matrix can be written in a compact form which is identical to the Kane-Mele Hamiltonian.

$$\boldsymbol{\mathcal{H}} = \mathrm{v_d}\big(\delta\mathrm{k_x}\hat{\boldsymbol{\tau}}_\mathbf{z}\hat{\mathbf{s}}_\mathbf{0}\hat{\boldsymbol{\sigma}}_\mathbf{x} + \delta\mathrm{k_y}\hat{\boldsymbol{\tau}}_\mathbf{0}\hat{\mathbf{s}}_\mathbf{0}\hat{\boldsymbol{\sigma}}_\mathbf{y}\big) + \omega_\mathrm{D}\Delta_\mathrm{em}\hat{\boldsymbol{\tau}}_\mathbf{z}\hat{\mathbf{s}}_\mathbf{z}\hat{\boldsymbol{\sigma}}_\mathbf{z} \tag{5.1.3}$$

This defines the photonic modes that have the same topological nature as the electronic states in graphene with strong SOC described by the last term. One side-note here is that that the coupling strength Δ_em will be relabeled as Δ_SOC for a broader framework encompassing different DOFs in the later chapter. Therefore, this BMW is an example of a QSH-PTI that posses a bandgap $\Delta\omega_{\mathrm{gap}} = 2\omega_{\mathrm{D}}|\Delta_{\mathrm{em}}|$.

5.1.2 Topological Spin Chern Index and Topologically Protected Edge Waves

As covered in the previous section, the spin DOF is constructed from the in-phase and out-of-phase relation between degenerate TE and TM modes at K/K' points. The spin-preserving perturbation which emulates the SOC in solid state physics is introduced by connecting one end of the cylinder with the confining plate to close one of the cylinder-to-plate air gaps. This bianisotropic perturbation breaking z mirror symmetry gives rise to a photonic bandgap centered at the double-degenerate Dirac point with the spectral width proportional to the overlap integral Δ_{em} between TE/TM modes inside the sealed cylinder-to-plate air gap. The electromagnetic modes propagating above and below the bandgap have a QSH-like topological nature with a spin-Chern number given by $2C^{\mathrm{SOC}}_{\uparrow/\downarrow,\mathrm{v}} = \pm 1 \times \mathrm{sgn}\,\Delta_{\mathrm{em}})$, where $\mathrm{s} = \uparrow, \downarrow$ is the spin label, $\mathrm{s} = \mathrm{K}, \mathrm{K}'$ is the valley label, and the valley-independent perturbation strength $\Delta_{\mathrm{em}} > 0$ $(\Delta_{\mathrm{em}} < 0)$ if the bottom (top) cylinder-to-plate gaps are closed with metal filling.

The topological spin-Chern index of the electromagnetic modes propagating below the bandgap changes sign when the rods are re-attached from the top to the bottom plate. Therefore, the Chern number is reversed across the wall between two QSH PTIs domains (“claddings”) with the rods attached to the opposite plates as shown in Fig. 1a. Such topological waveguide is expected to support four TPEWs plotted in Fig. 1b as red lines: two spin-up states propagating in the forward, and two spin-down states propagating in the backward directions. In the absence of spin-flipping perturbations, backscattering is prohibited for the TPEWs.

5.1.3 Toward experimental realization

The existence of localized TPEWs at the PTI's edge or at an interface between two PTIs with different electromagnetic properties holds great promise for photonic applications. Their scattering-free propagation along sharply-curved paths [36] opens exciting opportunities across the electromagnetic spectrum, including optical isolators [43,44], multiple-input multiple-output communications systems [45], and topologically robust broadband optical buffers and time delay lines [46,47]. Remarkably, while the latter set of applications was the original motivation for PTI development, an experimental demonstration of such functionality has been elusive. For example, in one successful implementation of topologically protected edge transport that utilized an ensemble of high-Q resonators [48], statistical properties of time delays were measured [49]. However, the combination of finite disorder and sharp resonances makes the development of a single-channel delay line in a given photonic structure extremely challenging.

5.2 EXPERIMENTAL REALIZATION OF QSH-PTI

5.2.1 Design and Fabrication of QSH-PTI Platform

This section is modified from the publication [50]. The proposed platform in this study is a rectangular layout contains two PCs of different topology separated by a straight domain wall along the longer dimension. As shown in Figure 5.1a, the size is designed to be 45 periods along the x-direction for long range transport of the surface states, and 20 periods in the y-direction to prevent energy leakage to the lateral boundaries.

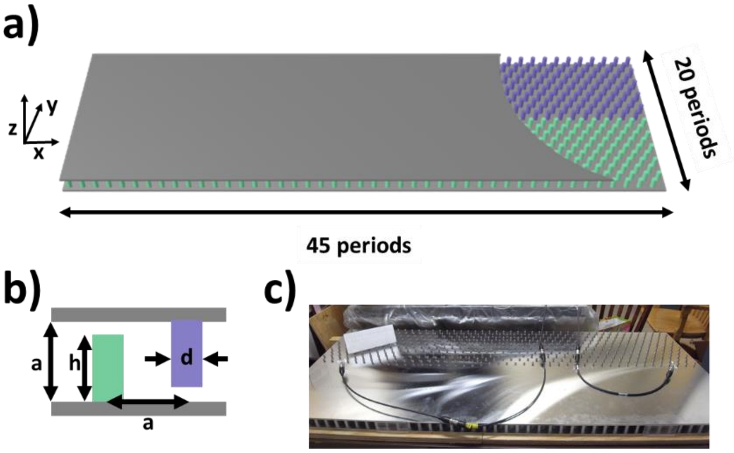

Figure 5.1 The fabrication of a QSH-PTI platform. a) Schematic of the platform layout totaling 45×20 periods of PCs. Part of the top metal plate is removed to reveal the cylinders attached to the bottom plate (green, $\Delta_{\mathrm{em}} > 0$) and to the top plate (purple, $\Delta_{\mathrm{em}} < 0$), leaving a gap to the other plate. b) Finalized geometric parameters of the unit cell of the QSH-PTI. See Table 5.1 for values of the parameters. c) Picture of fabricated structure made of aluminum.

The most important factor in fabricating the QSH-PTI platform is the choice of the operating frequency. Considering the material of the structure is a good conductor, the design of the QSH-PTI is highly scalable owing to the non-resonant working principle. In the microwave region, most of the metals are well conducting as mentioned in the Chapter 2 and aluminum 6061 has been chosen to be used for fabrication due to its lightweight, strong structural strength, and great variety of available shapes. Despite the scalability of design, the fabricated sample must meet the caliber of the instrumentation as well as the compatibility of future expansion. The top priority is to have the operating frequency fall into the spectral range of the testing instrument, vector network analyzer (VNA), which will be discussed in the later section. In the light of huge number of cylindrical rods (~900) to be fabricated, it is the most efficient to start with a round rod with long length and cut it down to the correct height of the rescaled design. This could avoid time-consuming turning process in metal machining at the expense of the precision of rod diameter up to the tolerance out of factory (~0.05 mm). Thus, the scaling factor of the design is specified by the rod diameter which is chosen to be $1/2$ inch (12.7 mm) due to the availability on the market. The finalized dimensions are summarized in Table 5.1.

	Value
Diameter of rod (d)	12.7 mm
Height of rod (h)	31.3 mm
Periodicity of lattice (a)	36.8 mm
Operating frequency	6.08 GHz
Wavelength	49.3 mm

Table 5.1 Dimensions of the finalized design of QSH-PTI unit cell in this study

During the structure assembling, the platform is divided into top and bottom pieces with rods attached to either top or bottom enclosing plate. To precisely install the rod onto the lattice point, a hole array of triangular lattice is drilled on a $1/4$ thick aluminum plate using computer numerical control (CNC) machining. A $1/4-20$ threaded hole is tapped into the end of cylindrical rod which is then fastened to the plate using a screw through the hole. In addition, a series of smaller holes are opened on the top plate at the line of domain wall so that the RF probes can stick into the parallel-plate waveguide for launching the surface states. Even with the aluminum in the sample fabrication, the total weight of the top piece is heavy enough to make the plate bulging downward which could destroy the modes. Several plexiglass spacers are made to provide structural support and maintain the constant separation between two plates.

5.2.2 Automated Test Station for RF Characterization

As mentioned briefly in the sample fabrication section, the whole instrumentation of this experiment is designed around the VNA, the standard equipment for RF device testing, which can measure both amplitude and phase of transmitted and reflected EM waves of a network. The specific model used in this study is a 2-port Agilent E5071C VNA with bandwidth from 1k Hz up to 8.5 GHz.

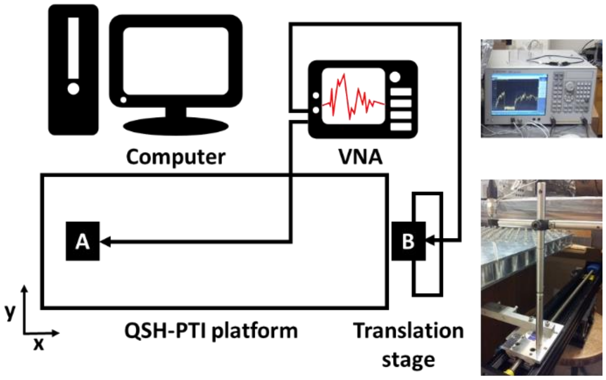

Figure 5.2 RF test station for probing QSH-PTI platform. Schematic of the setup. PC is used to control both VNA and stage. A: transmitting antenna stuck into the platform, B: receiving antenna place outside of the edge of platform. Insets are the picture of VNA and linear translation stage respectively.

In Figure 5.2, a customized setup capable of reliably scanning the probe through multiple wavelengths has been built to experimentally characterize the TPEWs at the interface. The backbone of this test station is modified from a legacy established by a former group member who has used it for investigating a sub-wavelength endoscope in microwave region. The current setup in this study consists of a personal computer, a VNA and a translation stage (VELMEX Single Axis BiSlide) to scan the probe along the interface. Therefore, one could program the computer to coordinate VNA to take spectrum and then reposition the probe a step farther for taking next spectrum. A full round of measurement containing multiple "scan-and-move" cycles along the scan path is termed as the edge scan measurement in this thesis. A set LabView codes is developed to automatically complete this measurement and save the data to a computer in the format of S-parameters. This RF test station is fully automated down to parameters input from the user. The parameters of the edge scan are summarized in the following table:

	Value	Remarks
Number of step	256	Total distance of travel: 406.64 mm
Step size	1.59 mm	
Frequency range	1 GHz~8GHz	
Sampling point	1601	
IF bandwidth	70 kHz	
Spectrum averaging	None	

Table 5.2 Input parameters of the LabView program for measuring QSH-PTI

To match the wavelength of interest, a dipole antenna along Z-direction used for launching and receiving is modified from a flexible cable (RG405 Coax) with SMA connectors. The outer conductor of the cable is stripped off leaving the core conductor with 19 mm in length for the best coupling efficiency. A plastic stopper is glued to the remaining outer shielding to ensure that the antenna is stuck into the structure with constant depth. The resulting antenna is attached to a SMA-N adapters (SM4236) which is then connected to a Type-N test cable from VNA port. These RF components are chosen to minimize the disturbance to the device under test and to rule out the spurious artifacts during the experiment.

5.2.3 Simulation, Data Processing and Analysis

In this study, two types of first-principles frequency domain electromagnetic simulations were performed using the COMSOL package: (a) the eigenvalue simulations which determine the frequencies $\omega(\vec{k}_\perp)$, $\vec{k}_\perp = (k_x, k_y)$ is the in-plane wavenumber, $\omega = 2\pi f$ is the angular frequency, and (b) the driven simulations that determine the electric/magnetic field distribution for a given current source. To examine the effect of Ohmic loss in metal and plasmonic effects on the propagation of the TPEWs around $\omega = 1.5\ \mu m$, we performed eigenfrequency simulation by scaling down the dimensions of the photonic structure. The relative geometric sizes of the structure were slightly adjusted to account for the plasmonic response of the selected metal (silver). With loss in the metal fully accounted for, we found the propagation length $L_x \approx 60a \approx 48\lambda$ to be sufficiently long for taking advantage of topological protection.

To obtain the PBS of the topologically trivial/non-trivial waveguides, eigenvalue simulations were carried out on a supercell containing a single period along the X-direction, and 30 cells on each side of the interface. The shaded regions resultant PBS are the projected band structure of the bulk modes. The transmission through the photonic structures containing a straight interface and a bent interface with one or two detours were calculated using driven simulations on the simulation domains containing 45×20 cells so as to closely approximate the actual structure used in the experiments.

Despite carefully choosing the RF components, it is important to notice the fact that repositioning the probe inevitably induces cable movement between two consecutive measurements. The resulting signal distortion could not be easily suppressed by the standard fixture removal practice since the effect is constantly changing in between each measurement. To mitigate this effect, we choose to post-process the measured spectrum using moving average with a 50MHz windows to account for the cable movement.

The subsequent data analysis aims at smoothing the interference pattern produced by the superposition of the positive and negative index spin-up TPEWs. The spatial periodicity of the resulting intensity pattern is $\mathrm{P_x} = 3\mathrm{a}$ along the interface separating the two PTIs. The following averaging treatment is used to suppress this beat pattern and to clarify the intensity distribution: every transmission curve of the TPEWs is the average of 6 individual raw $|\mathrm{S}_{21}|^2(\mathrm{y}, \mathrm{f}; x_0)$ spectra for the feeding source positions ${x_0}^{(i)}$ (where $\mathrm{i} = 1, \dots 6)$ that are evenly spaced inside the $0 < {x_0}^{(i)} < \mathrm{P_x}$. In the case of TTGWs, similar procedure of averaging over the $0 < {x_0}^{(i)} < \mathrm{P_x}$ interval is used, but with $\mathrm{i} = 1,2,3$. The averaging domain spans from 4th rod to 6th rod along the interfaces for both TPEWs and TTGWs cases.

5.3 VERIFICATION OF TOPOLOGICALLY PROTECTED EDGE WAVES

5.3.1 Verification of Fabricated Platform

To experimentally realize the existence of the TPEWs, it is crucial to distinguish the surface modes from the bulk mode. Beginning from the most basic building block of platform, we will show the undeniable evidence to the existence of TPEWs step-by-step in this section. First, the fabricated structure is subject to the verification of functioning as designed. It is done by measuring the platform containing only one kind of QSH-PTI and then compared the measured data with numerical prediction.

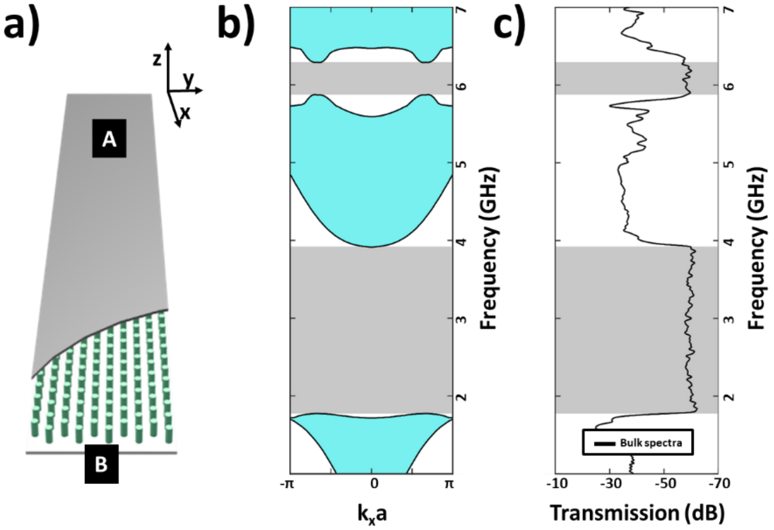

Figure 5.3 Bulk modes measurement and simulation verification. a) Schematic of the setup for testing the platform containing one kind of QSH-PTI (all rods attached to the bottom plate). A: launching port at 5 periods from the edge, B: receiving port placed outside of the structure. b) Calculated photonic band structure of the QSH-PTI. c) Measured transmission spectra $|S_{21}|^2$ through the bulk PTI. Cyan: bulk modes, gray region: complete PBG.

Instead of building a new platform for this measurement, we choose a pragmatic way of reconfiguring the existing top and bottom pieces to form a half-size (45×10)

structure in Figure 5.3. It is natural to ask if this number of cells is large enough to build up collective behaviors of a periodic crystal. From the preliminary test done by Xiao Bo from Professor Steven Anlage's group, our collaborators in University of Maryland, a smaller size test unit containing only 31 rods could provide fair performance compared to the numerical simulation. Needless to say, the platform consisting of 45×10 cells is a much better approximation to an infinitely large crystal. The said platform is assembled in a way that the metal plate is facing opposite direction to avoid forming propagating modes at the edges and thus to minimize the possible reflection from the air interface.

The resulting structure is then characterized by the test station. Note that this is not an edge scan since only one spectrum is taken with the receiving probe at port B as indicated in the figure. The first observation of the measured spectra of bulk modes in Figure 5.3c is the regions of low transmission (gray shaded area) where the signal strength is below the detectable level of the VNA. These are the complete PBGs where no waves can travel in any direction inside the crystal. The spectral positions of these PBGs are in excellent agreement to the numerical prediction: one topologically trivial PBG at the lower frequency $\mathrm{f}{:}\ 1.8\ \mathrm{GHz} < \mathrm{f} < 3.9\ \mathrm{GHz}$ and the other topologically non-trivial PBG at frequency of interest for $\mathrm{f}{:}\ 5.87\ \mathrm{GHz} < \mathrm{f} < 6.29\ \mathrm{GHz}$. This verification lays a solid foundation rock toward discovering the TPEWs.

5.3.2 Measuring the Topologically Protected Edge Waves

In Figure 5.4, the platform is assembled to the proposed configuration and the same single spectrum measurement is performed to probe the TPEWs. This time around we concentrate at the PBG at higher frequency where the edge states are designed. It is obvious that the measured spectrum is very different from the bulk modes. Specifically, the transmission is largely enhanced (~30 dB) in the PBG which suggesting the formation of a new propagation channel after interfacing two domains of QSH-PTIs. Note that both spectra in Figure 5.4c are normalized to the transmission peak of the edge spectrum for the future comparison. However, this piece of evidence is not yet sufficient to deduce the existence of the TPEWs. The conclusive argument could only be made after the correlation between the enhanced transmission and the edge states is demonstrated experimentally.

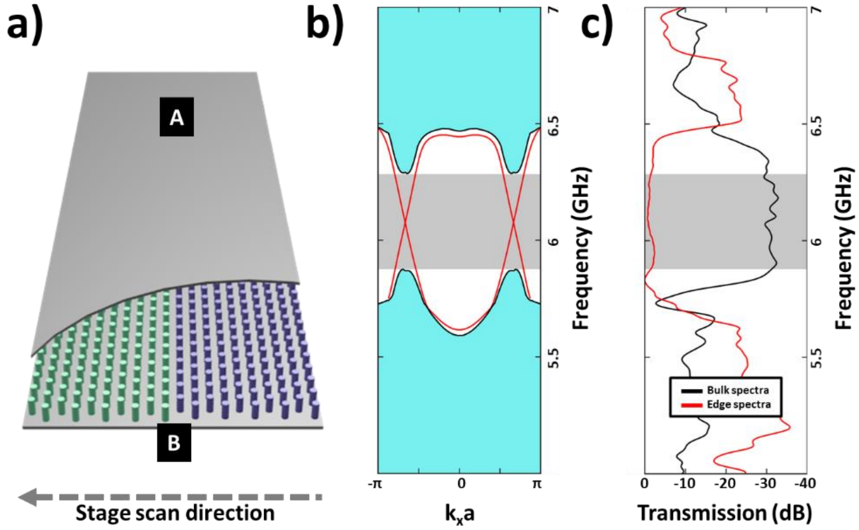

Figure 5.4 Experimentally measured TPEWs. a) Schematic of platform layout of the platform containing topologically non-trivial interface between two dissimilar QSH-PTI domains. A: launching port, B: receiving port. b) Calculated photonic band structure with topologically non-trivial interface. Cyan: bulk modes, red curve: edge states inside the PBG, gray region: complete PBG. c) Measured transmission spectra $|S_{21}|^2$ through the bulk PTI. Black: bulk modes, red: edge states.

Thus, the next step is to show that this enhancement in transmission results from the newly formed edge states at the domain wall between two topologically distinct photonic crystals. By mapping out the spatial distribution of the energy along the edge of the structure, the edge scan could provide univocal evidence that this enhanced transmission is indeed the result of the existence of the TPEWs. In Figure 5.5b, the color map shows the result of edge scan consisting 257 transmission spectra along the edge of the structure around the interface. The stage scans along with total distance of travel equal to roughly 12 unit cells in Y-direction which is more than sufficient to capture the signature of decaying tail from the surface wave.

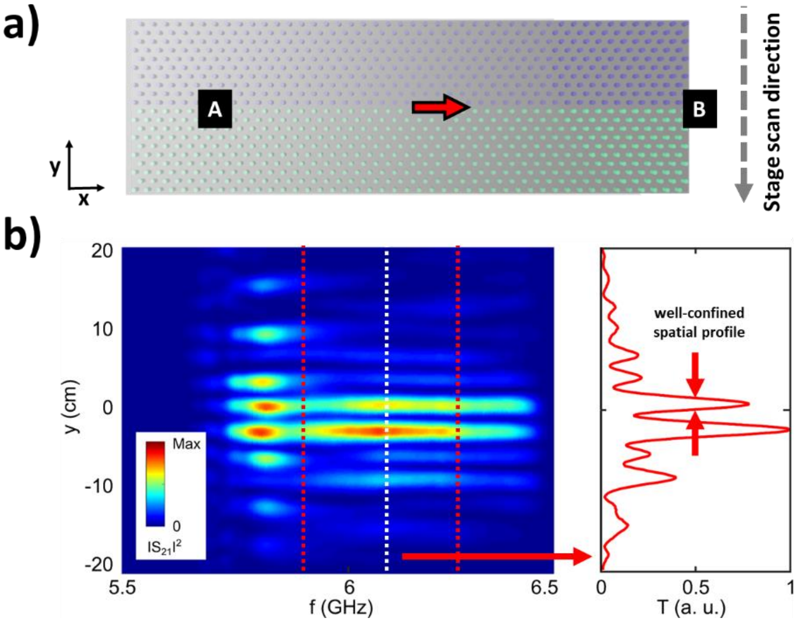

Figure 5.5 Edge scan measurement of TPEWs. a) A straight path of wave propagation. b) Color map consists of 257 transmission spectra taken at the edge of the structure to show the localized spatial confinement of the edge modes. White dashed line: spectral position at mid-gap frequency, red dashed line: the spectral region of the topologically non-trivial PBG hosting the TPEWs. Inset: the line cut at the mid-gap frequency to show the confinement of the wave at the interface ($y = 0$).

Indeed, one can easily identify the transmission plateaus around $y = 0$ whereas the signal is very low at the position away from the interface. Furthermore, a line cut at the mid-gap frequency (white dash line) is extracted to explicitly show the tight energy localization (red arrows) as well as the decaying trend in transversal direction. The important to notice the fact that this wave remains tightly confined at the domain wall even after 30 wavelength of propagation which implies that the transmission peaks in the bandgap is due to a surface waves at the boundary between two PCs. This solidify the connection between the enhanced transmission and the existence of the edge states.

Consequently, the existence of TPEWs across the entire bandgap is experimentally demonstrated in Figure 5.5c by measuring the ~30dB transmission enhancement over that through the bulk PTI. Therefore, the electromagnetic waves excited by the launching antenna inside the bandgap do not evanescently tunnel through the PTI's bulk. Instead, they couple to the surface mode and propagate unimpeded towards the probe antenna at port B as illustrated on Figure 5.5a. To the best of our knowledge, this is the first experimental evidence of the wavelength-scale confinement of a surface wave propagating at the interface between two PTIs.

5.3.3 Robust Wave Propagation of TPEWs

Finally, we demonstrate the topological protection of the surface wave by experimentally observing its most important physical property: that reflection-free energy flow can occur despite encountering a broad class of possible lattice defects along its propagation path that maintain spin-degeneracy and preserve the spin DOF. Within this class falls the detour defect shown Figure 5.6a, where the rods are re-attached to the opposite plate so as to bend the interface between PTIs. The defect contains four 120° bends indicated by red circles, each of which is capable of reflecting most of the incident surface wave in the absence of topological protection. Therefore, it is not surprising to find that instead of being scattered by the defect in the path of propagation, the surface wave is still localized tightly from the edge scan result in Figure 5.6. There is only negligible change to the transmitted peaks while the signal drops significantly at the outer edge of the bandgap.

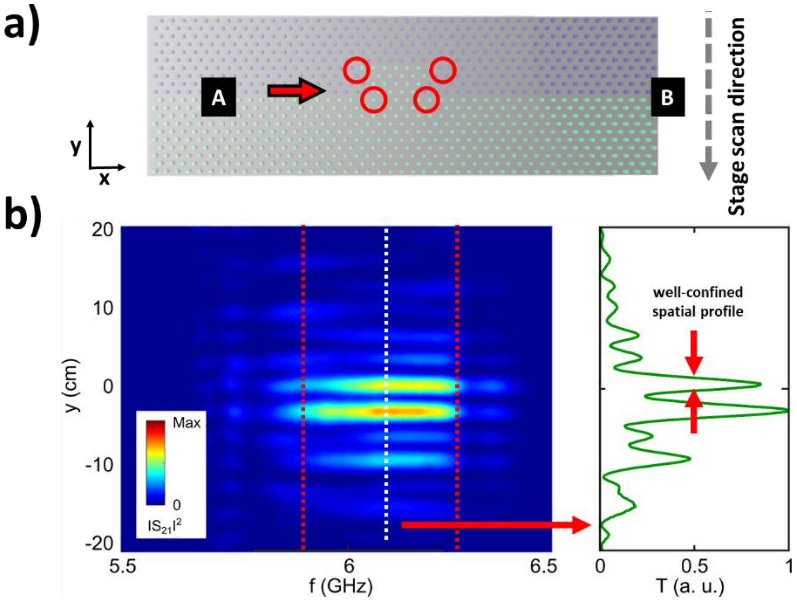

Figure 5.6 Edge scan measurement of TPEWs propagating along a detoured path. a) A detour path of wave propagation. Red circle: sharp corner of a severe defect. b) Color map consists of 257 transmission spectra taken at the edge of the structure to show the localized spatial confinement of the edge modes. White dashed line: spectral position at mid-gap frequency, red dashed line: the spectral region of the topologically non-trivial PBG hosting the TPEWs. Inset: the line cut at the mid-gap frequency to show the confinement of the wave at the interface ($y = 0$).

The topological protection is apparent from Figure 5.7a where the transmission spectra along the uninterrupted interface (red line) and the same interface interrupted by a detour-type defect (green line) are plotted as a function of frequency. Outside of the bandgap (*e.g.* at the frequencies marked by black arrows) the transmission is reduced by almost an order of magnitude because the defect blocks the propagating bulk modes from the receiving antenna. Inside the bandgap, however, the forward-propagating spin-up TPEW flows around the defect because the defect does not flip the spin, and no back-reflection is allowed (Figure 5.7b). The almost negligible ~1dB decrease in transmission (red arrow) serves as a clear experimental signature of topologically robust transport.

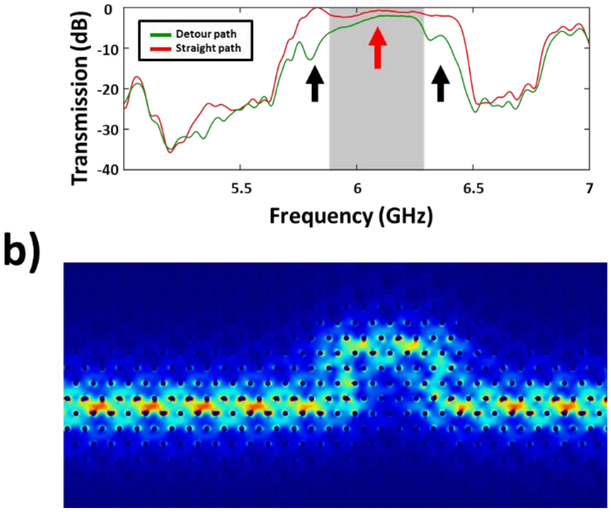

Figure 5.7 Robust test of TPEWs propagating along a detour path. a) Comparison of measured transmission spectra between the straight (red curve) and the detour (green curve) interfaces b) Simulated energy density at $f = 6.08$ GHz showing the TPSW flowing around the defect without scattering.

5.4 COMPARISON TO TOPOLOGICALLY TRIVIAL WAVEGUIDES

The uniqueness of topological protection of guided waves is underscored by comparing the topological waveguide described above with a topologically-trivial one, which is formed by removing one row of cylinders. The resulting waveguide (Figure 5.8a) supports topologically trivial guided waves (TTGWs) that are spectrally located (orange curve in Figure 5.8b) inside the topologically trivial band gap of the claddings centered at mid-gap frequency $f \approx 3$ GHz(gray area).

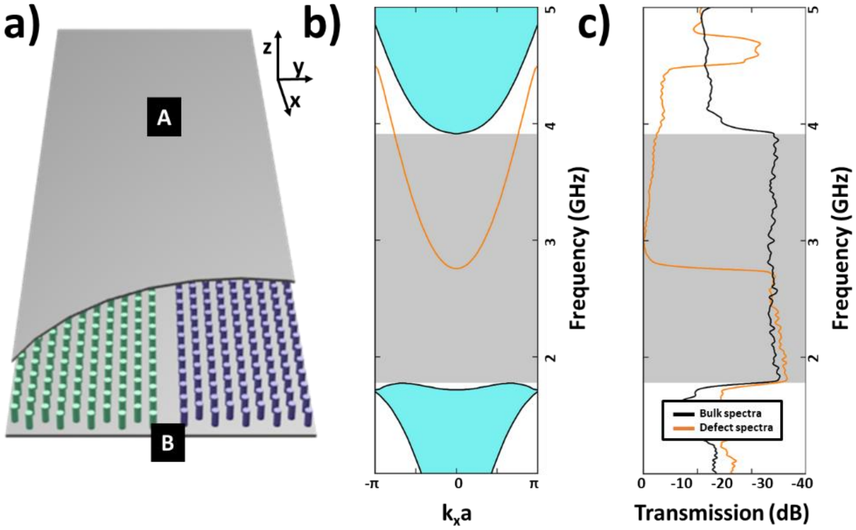

Figure 5.8 Experimentally measured TTGWs. a) Schematic of platform layout of the platform containing topologically trivial interface between two dissimilar QSH-PTI domains. A: launching port, B: receiving port. Note that one row of rods is removed to create a defect waveguide for TTGWs. b) Calculated photonic band structure with topologically trivial interface. Cyan: bulk modes, orange curve: defect modes inside the PBG, gray region: complete PBG. c) Measured transmission spectra $|S_{21}|^2$ through the bulk PTI. Black: bulk modes, orange: defect modes.

In Figure 5.9a, we insert a large sharply-edged scattering defect into the path of the TTGW. While the defect is almost identical to the one inserted into the path of the TPEW, its effect on the TTGW is dramatically different. For most frequencies, the measured transmission plotted in Figure 5.9b is more than an order of magnitude lower than in the absence of the defect. High narrow-band transmission and tight spatial confinement due to resonant tunneling and multi-bounce backscattering only occurs at the three Fabry-Pérot (FP) resonances of the defect (Figure 5.9c). The absence of such FP resonances for the TPEWs observed from Figure 5.7b is the experimental proof of their topological protection against backscattering.

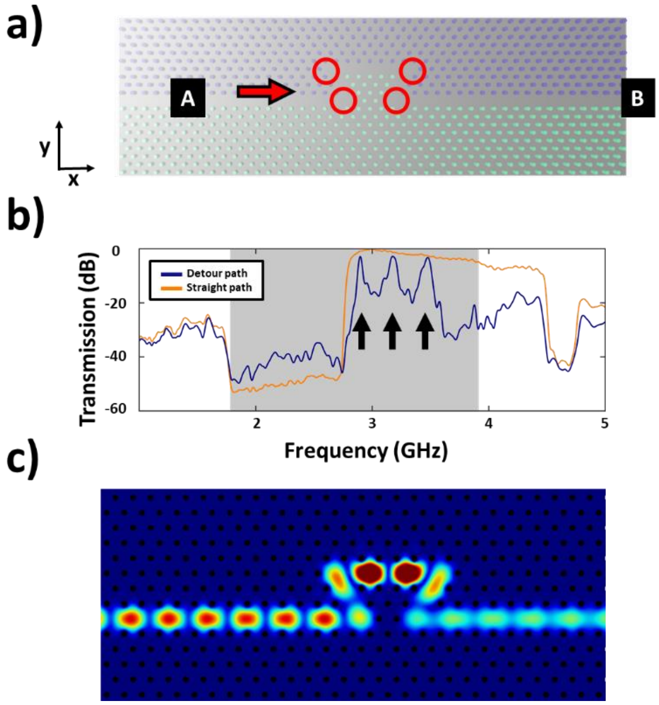

Figure 5.9 Robust test of TTGWs propagating along a detoured path. a) A detour path of wave propagation. Red circle: sharp corner of a severe defect. b) Comparison of measured transmission spectra between the straight (orange curve) and the detour (blue curve) path. c) Simulated energy density at $f = 2.95$ GHz showing the TTGW resonant tunneling through the defect.

Chapter 6 Quantum Valley Hall Photonic Topological Insulator

6.1 INTRODUCTION TO QVH PTI PLATFORM

6.1.1 Brief Recap of QVH PTI Design

This chapter following the same line in Ma's publication [37] which implements new binary DOFs, namely QVH PTIs emulating quantum valley Hall effect and QH PTIs emulating quantum Hall effect, on the existing QSH PTI platform based on photonic graphene. Specifically, the QVH PTI is of great interest of the novel out-coupling property [51] and thus will be the main focus in this study. The theoretical background is briefly revisited in this section and the experimental realization is modified from the joint publication [52] with collaborators from Nanyang Technological University in Singapore in the latter section[2].

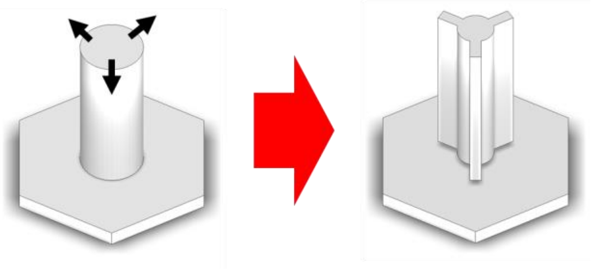

Figure 6.1 Deformation of the unperturbed unit cell of photonic graphene to the broken in-plane inversion symmetry.

The detailed derivation of the effective Hamiltonian for QVH PTI is thoroughly covered in the supplemental information of Ma's publication [37,51]. The gist is recapped in the section for the sake of completeness. Consider a deformation of the unperturbed unit cell to a tripod-like C_3-symmetric shape that breaks in-plane inversion symmetry with respect to the principal axis of the lattice as in the Figure 6.1, the perturbation strength Δ_P can be calculated by overlapping integral from the perturbation theory. Note that the calculation is greatly simplified due to the fact that this perturbation doesn't couple TE and TM modes which will be addressed by symmetry argument later and further simplification reals that the perturbed Hamiltonian is diagonalized in the CP basis with 8-component spinor $\boldsymbol{\Psi} = [\mathbf{V_K}; \mathbf{TV_{K'}}]$, where the transformation matrix T swaps the RCP and LCP orbital states.

---

[2] The content of this chapter is modified from a prior publication: Gao, F., Xue, H., Yang, Z., Lai, K., Yu, Y., Lin, X., Chong, Y., Shvets, G. and Zhang, B., "Topologically protected refraction of robust kink states in valley photonic crystals". *Nature Physics* **14**, 140-144 (2018). The author designed part of the unidirectional excitation experiment and contributed to manuscript writing.

First, we perform a π-rotation operation $\mathcal{P}$ with respect to z-axis on the four eigenstates at K valley $\mathbf{V}_\mathbf{K}^{\uparrow/\downarrow,\mathbf{R/L}}$ (the rest four eigenstates at K' valley are denoted by $\mathbf{V}_\mathbf{K'}^{\uparrow/\downarrow,\mathbf{R/L}}$). $\mathcal{P}$ transformation takes x to -x, y to -y, and thus K to K'. It can be shown that the Hamiltonian before and after the $\mathcal{P}$ operation has the following relation:

$$\boldsymbol{\mathcal{H}}_{\mathbf{P,K'}}^{(\mathbf{rev})} = -\omega_\mathrm{D}\Delta_\mathrm{P}\hat{\mathbf{s}}_\mathbf{0}\hat{\boldsymbol{\sigma}}_\mathbf{z} = -\boldsymbol{\mathcal{H}}_{\mathbf{P,K}} \tag{6.1.1}$$

where the $\boldsymbol{\mathcal{H}}_{\mathbf{P,K'}}^{(\mathbf{rev})}$ is the perturbed Hamiltonian. Next, we have to prove $\boldsymbol{\mathcal{H}}_{\mathbf{P,K'}} = -\boldsymbol{\mathcal{H}}_{\mathbf{P,K'}}^{(\mathbf{rev})}$ in order to reach the final conclusion: $\boldsymbol{\mathcal{H}}_\mathbf{P} = \hat{\boldsymbol{\tau}}_\mathbf{0}\otimes\boldsymbol{\mathcal{H}}_{\mathbf{P,K}}$. To see the connection between $\boldsymbol{\mathcal{H}}_{\mathbf{P,K'}}^{(\mathbf{rev})}$ and $\boldsymbol{\mathcal{H}}_{\mathbf{P,K'}}$ of the original perturbation, we show that the sign of the perturbation strength is reversed due to the re-orientation of the tripod, $\Delta_\mathrm{P} \rightarrow -\Delta_\mathrm{P}$, which can be show explicitly from applying $\mathcal{P}$ transformation while calculating the perturbation strength. Therefore, $\boldsymbol{\mathcal{H}}_{\mathbf{P,K'}} = -\boldsymbol{\mathcal{H}}_{\mathbf{P,K'}}^{(\mathbf{rev})} = \boldsymbol{\mathcal{H}}_{\mathbf{P,K}}$, and the Hamiltonian equations at the K and K' points for all the eigenstates are

$$\begin{pmatrix} \boldsymbol{\mathcal{H}}_{\mathbf{P,K}} & \mathbf{0}_{4\times4} \\ \mathbf{0}_{4\times4} & \boldsymbol{\mathcal{H}}_{\mathbf{P,K'}} \end{pmatrix} \begin{pmatrix} \mathbf{V}_\mathbf{K}^{\uparrow/\downarrow,\mathbf{R/L}} \\ \mathbf{0} \end{pmatrix} = \omega_\mathrm{D}\Delta_\mathrm{P} \begin{pmatrix} \hat{\mathbf{s}}_\mathbf{0}\hat{\boldsymbol{\sigma}}_\mathbf{z} & \mathbf{0}_{4\times4} \\ \mathbf{0}_{4\times4} & \hat{\mathbf{s}}_\mathbf{0}\hat{\boldsymbol{\sigma}}_\mathbf{z} \end{pmatrix} \begin{pmatrix} \mathbf{V}_\mathbf{K}^{\uparrow/\downarrow,\mathbf{R/L}} \\ \mathbf{0} \end{pmatrix}$$

$$\begin{pmatrix} \boldsymbol{\mathcal{H}}_{\mathbf{P,K}} & \mathbf{0}_{\mathbf{4\times4}} \\ \mathbf{0}_{\mathbf{4\times4}} & \boldsymbol{\mathcal{H}}_{\mathbf{P,K'}} \end{pmatrix} \begin{pmatrix} \mathbf{0} \\ \mathbf{TV}_{\mathbf{K'}}^{\uparrow/\downarrow,\mathbf{R/L}} \end{pmatrix} = \omega_{\mathrm{D}}\Delta_{\mathrm{P}} \begin{pmatrix} \hat{\mathbf{s}}_{\mathbf{0}}\hat{\boldsymbol{\sigma}}_{\mathbf{z}} & \mathbf{0}_{\mathbf{4\times4}} \\ \mathbf{0}_{\mathbf{4\times4}} & \hat{\mathbf{s}}_{\mathbf{0}}\hat{\boldsymbol{\sigma}}_{\mathbf{z}} \end{pmatrix} \begin{pmatrix} \mathbf{0} \\ \mathbf{TV}_{\mathbf{K'}}^{\uparrow/\downarrow,\mathbf{R/L}} \end{pmatrix}$$

(6.1.2)

or simply

$$\begin{aligned} \boldsymbol{\mathcal{H}}_{\mathbf{P}}\Psi^{K,\uparrow/\downarrow,R/L} &= \omega_{\mathrm{D}}\Delta_{\mathrm{P}}\otimes\hat{\mathbf{s}}_{\mathbf{0}}\hat{\boldsymbol{\sigma}}_{\mathbf{z}}\Psi^{K,\uparrow/\downarrow,R/L} \\ \boldsymbol{\mathcal{H}}_{\mathbf{P}}\Psi^{K',\uparrow/\downarrow,R/L} &= \omega_{\mathrm{D}}\Delta_{\mathrm{P}}\otimes\hat{\mathbf{s}}_{\mathbf{0}}\hat{\boldsymbol{\sigma}}_{\mathbf{z}}\Psi^{K',\uparrow/\downarrow,R/L} \end{aligned} \tag{6.1.3}$$

in which we have proven that $\boldsymbol{\mathcal{H}}_{\mathbf{P}} = \omega_{\mathrm{D}}\Delta_{\mathrm{P}}\hat{\mathbf{s}}_{\mathbf{0}}\hat{\boldsymbol{\sigma}}_{\mathbf{z}}$.

One important element during the above derivation is to verify that this deformation perturbation is diagonalized with respect to the CP basis or doesn't couple TE and TM modes so to speak. The goal is then to prove cross-overlap integrals between RCL and LCP must be zero under this perturbation. We start with the observation that, by performing a $2\pi/3$ rotation ($\mathcal{R}_3$) around the z-axis, the perturbed structures are not altered. The perturbation strength takes the form $\Delta_{\mathrm{RL}}^{\mathrm{P,e(m)}} = -\int_{\Delta\mathrm{V}}\left[\mathrm{e}_{\mathrm{e(m)}}^{\mathrm{R*}}\cdot\mathrm{e}_{\mathrm{e(m)}}^{\mathrm{L}} - \mathrm{h}_{\mathrm{e(m)}}^{\mathrm{R*}}\cdot\mathrm{h}_{\mathrm{e(m)}}^{\mathrm{L}}\right]\mathrm{dV}$ where e and h are the electric (magnetic) coefficients of the basis and the 'e' and 'm' denotes the TE and TM modes respectively. Because the system is unchanged under $\mathcal{R}_3$, the following equality must hold:

$$\Delta_{\mathrm{RL}}^{\mathrm{P,e(m)}} = \mathcal{R}_3\Delta_{\mathrm{RL}}^{\mathrm{P,e(m)}} \tag{6.1.4}$$

The explicit operation of $\mathcal{R}_3 \equiv \mathcal{R}_{\theta=2\pi/3}$ contains two parts: (i) mapping the argument of a function such that $(\mathrm{x,y,z}) \rightarrow (\mathrm{x',y',z'})$ where $(\mathrm{x',y',z'})^{\mathrm{T}} = \bar{\bar{\mathrm{R}}}_{-\theta}(\mathrm{x,y,z})^{\mathrm{T}}; \bar{\bar{\mathrm{R}}}_{-\theta} = \begin{pmatrix} \cos\theta & -\sin\theta & 0 \\ \sin\theta & \cos\theta & 0 \\ 0 & 0 & 1 \end{pmatrix}$ and $\theta = 2\pi/3$; rotating the components of a vector such that $\left(\mathrm{v_x,v_y,v_z}\right)^{\mathrm{T}} \rightarrow \bar{\bar{\mathrm{R}}}_{-\theta}\left(\mathrm{v_x,v_y,v_z}\right)^{\mathrm{T}}$. Combining these two together, one has the rotation operation of a vector field:

$$\mathcal{R}_3\begin{pmatrix} \mathrm{v_x(x,y,z)} \\ \mathrm{v_y(x,y,z)} \\ \mathrm{v_z(x,y,z)} \end{pmatrix} = \bar{\bar{\mathrm{R}}}_{\theta}\begin{pmatrix} \mathrm{v_x(x',y',z')} \\ \mathrm{v_y(x',y',z')} \\ \mathrm{v_z(x',y',z')} \end{pmatrix} \tag{6.1.5}$$

From the definition of the R and L fields, we know that $\mathcal{R}_3 e_{e(m)}^{R} = \eta^{*} e_{e(m)}^{R}$ and $\mathcal{R}_3 e_{e(m)}^{L} = \eta e_{e(m)}^{L}$, where $\eta = \exp(i\,2\pi/3)$. Thus, equation 6.1.4 becomes

$$\begin{aligned}\Delta_{RL}^{P,e(m)} &= -\int_{\Delta V} \left[\mathcal{R}_3 e_{e(m)}^{R*} \cdot \mathcal{R}_3 e_{e(m)}^{L} - \mathcal{R}_3 h_{e(m)}^{R*} \cdot \mathcal{R}_3 h_{e(m)}^{L}\right] dV \\ &= \eta^2 \int_{\Delta V} \left[e_{e(m)}^{R*} \cdot e_{e(m)}^{L} - h_{e(m)}^{R*} \cdot h_{e(m)}^{L}\right] dV \\ &= \eta^2 \Delta_{RL}^{P,e(m)}\end{aligned} \tag{6.1.6}$$

To satisfy the above equality, the cross-overlap integral $\Delta_{RL}^{P,e(m)}$ has to be zero.

6.1.2 Topological Valley Chern Index and Topologically Protected Edge Waves

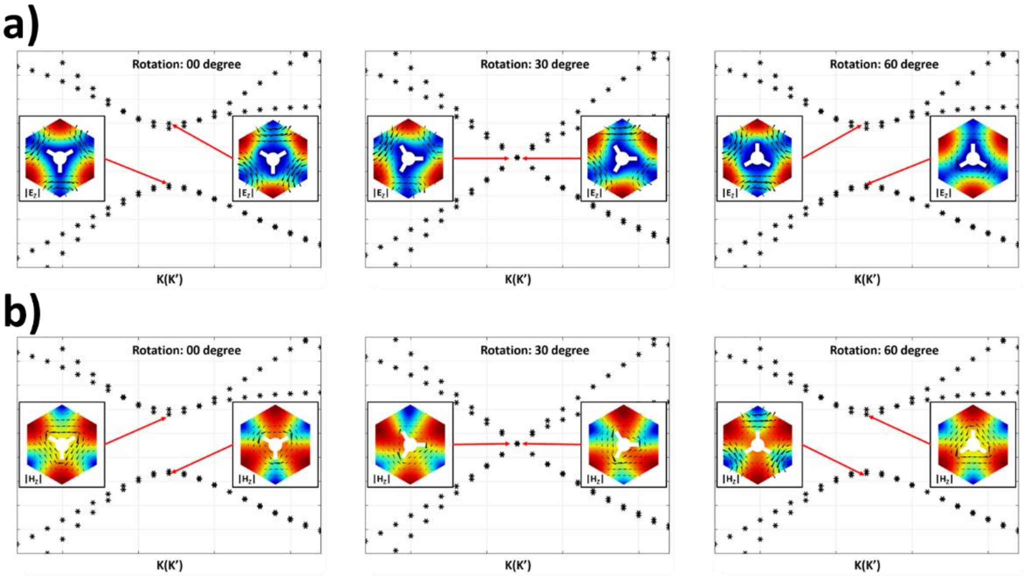

Figure 6.2 PBS of QVH PTI unit cells with various perturbation strength. Field profiles of the relevant bands at K(K') point for a) $|E_Z|$ component of TM modes and b) $|H_Z|$ component of TE modes at $\theta = 0°, 30°, 60°$. Color plot: strength of field component; black arrow: Poynting flux.

It is essential to match the perturbation strength of TE and TM modes so that the perturbed structure becomes QVH PTIs emulating quantum valley Hall effect [53] and henceforth supports propagating electromagnetic waves below the bandgap with a spin-independent valley-Chern number $2C^{P}_{s,K/K'} = \pm 1 \times \mathrm{sgn}(\Delta_P)$. The width of this bandgap is proportional to perturbation strength Δ_P which can be controlled by rotating the tripods with respect to the principle axes and is maximized at $\theta = 0° \, (\Delta_P > 0), 60° (\Delta_P < 0)$ where the strongest perturbation happens as shown in Figure 6.2.

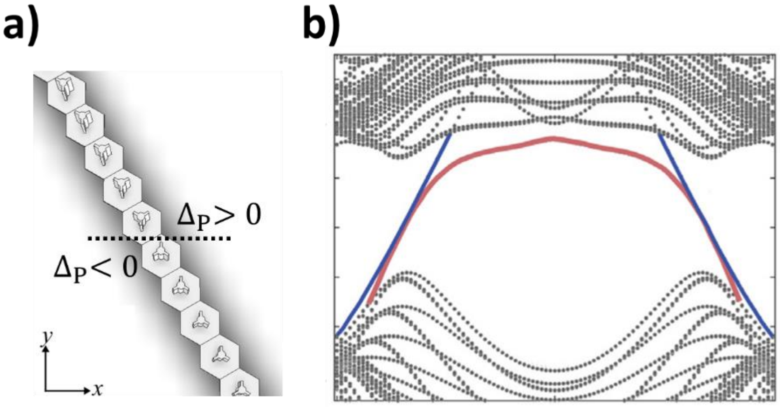

Figure 6.3 Dispersion relation of the TPEWs at QVH/QVH ($\Delta_P > 0, \Delta_P < 0$) interface. a) The geometry of the topological interface (black dashed line) between two QVH PTIs. The boundary condition of supercell simulation is periodic in X-direction. b) Calculated PBS of the TPEWs. Red curves: TE polarization, blue curves: TM polarization.

The ability to control the sign of Δ_P by simply rotating the tripods of a QVH PTI allows one to create a topological cladding that supports TPEWs at the QVH/QVH interface ($\Delta_P > 0, \Delta_P < 0$). According to the bulk-boundary correspondence [54], the difference between the number of forward-moving modes and the number of backward-moving modes equals the difference of the valley Chern indices. For example, an interface along the zigzag direction shown in Figure 6.3 has $\Delta_P > 0$ ($\Delta_P < 0$) in the upper (lower) domain; consequently, there is a forward-moving TPEW at the K point because $\mathrm{C}_{\mathrm{s,K}}^{\mathrm{P}} - \mathrm{C}_{\mathrm{s,K}}^{\mathrm{P}} = +1/2 - (-1/2) = 1$ and a backward-moving TPEW at the K' point because $\mathrm{C}_{\mathrm{s,K'}}^{\mathrm{P}} - \mathrm{C}_{\mathrm{s,K'}}^{\mathrm{P}} = -1/2 - (+1/2) = -1$. And vice versa for the interface with the other configuration ($\Delta_{\mathrm{P}} < 0$ in upper domain and $\Delta_{\mathrm{P}} > 0$ in the lower domain). The dispersions of TPEW for such interfacing are calculated using COMSOL Multiphysics.

6.2 EXPERIMENTAL REALIZATION OF VSH PTI

6.2.1 Fabrication and Experimental Results of VSH PTI Platform

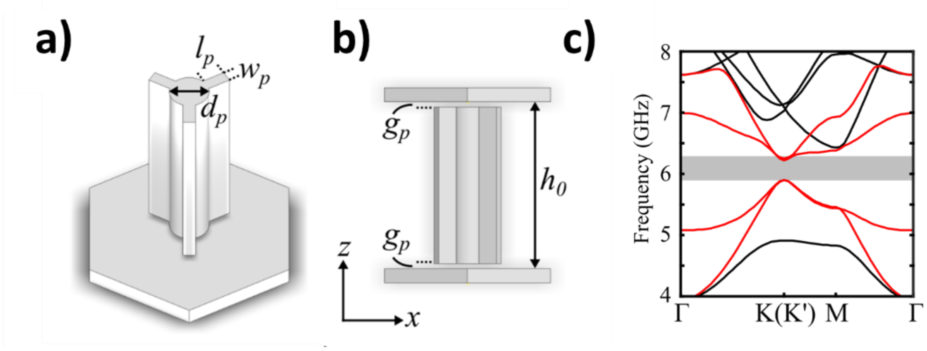

Figure 6.4 Realistic design of QVH PTI. a) tripod-like shape metallic cylinder breaking in-plane symmetry. b) Side-view of the metallic tripod suspended between two parallel metallic plates leaving two symmetric gaps between the cylinder and two plates. This preserves the symmetry which is used for tailoring spin DOF in Chapter 5. c) PBS of the QVH PTI. Red curves: topologically non-trivial modes.

This section is modified from the joint publication [52]. To pave the way to the integrated system of topological photonics, the operating frequency is rescaled to be the same as the QSH PTI [50] in Chapter 5, namely $f_0 = 6.08\text{GHz}$. The resulting geometric parameters are summarized in the Table 6.1.

	Value
Operating frequency	6.08 GHz
Wavelength	49.3 mm
Diameter of rod (d_p)	7.36 mm
Height of parallel plate (h_0)	36.8 mm
Periodicity of lattice (a)	36.8 mm
Width of protrusion (w_p)	2.21 mm
Length of protrusion (l_p)	4.27 mm
Gap between plate (g_p)	1.1mm

Table 6.1 Dimensions of the finalized design of QSH PTI unit cell in this study.

To meet the tolerance and minimized the deviation from the design, the tripods are outsourced and fabricated by wire electric discharge machining (wire-EDM). The resulting parts are sandwiched by parallel plate waveguide with the 1.10 mm air gaps are filled with a low-refractive index foam spacer (ROHACELL 71 HF) to provide mechanical support. The assembled structure then is characterized by a VNA on a similar RF test station in Nanyang Technological University.

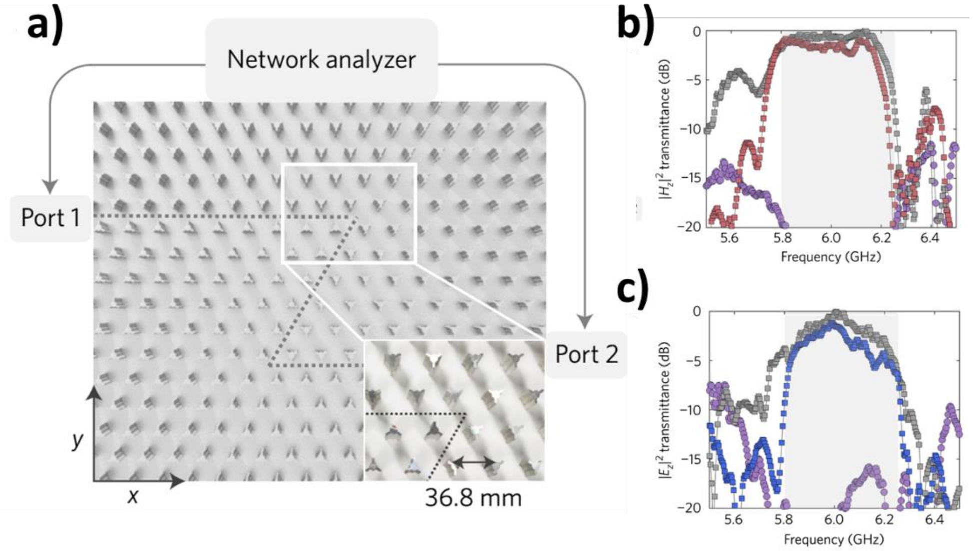

Figure 6.5 The experimental set-up for measuring kink states. a) The zigzag domain wall is indicated with a dashed line. The inset is a zoomed-in photo. The upper metallic plate of the parallel-plate waveguide is removed for illustration. b) Measured $|H_z|^2$ transmittance. Grey/red curves are for straight/zigzag domain walls, respectively. Purple curve is for a straight domain wall when the bandgap in the upper domain closes. c) Measured $|E_z|^2$ transmittance. Grey/blue curves are for straight/zigzag domain walls, respectively. Purple curve is for a straight domain wall when the bandgap in the upper domain closes. Courtesy of Fei Gao.

Following the same logic in Chapter 5, the robust transport of the TPEWs based on the platform QVH PTIs is demonstrated by comparing the transmitted signal between a straight path and a sharply curved path with two 120° corners. Similar to the case of the platform of QSH PTI, the TPEWs propagates through the detour path unimpededly without significant loss from the sharp corners. In addition, these is no transmission peaks resulted from the resonant tunneling at the spectral position of the FP resonance thanks to the scattering-free wave propagation under the topological protection. The importance of is topological protection of TPEWs is further emphasized by the severe signal decrease in the case of an interface between QVH PTIs with $\Delta_{\mathrm{P}}< 0$ and with $\Delta_{\mathrm{P}}= 0$ where the photonic band gap is closed as shown by the purple curves in Figure 6.5b and c. In addition, the field confinement is again verified from the discrete edge scan along the outer edge perpendicular to the interface in Figure 6.6.

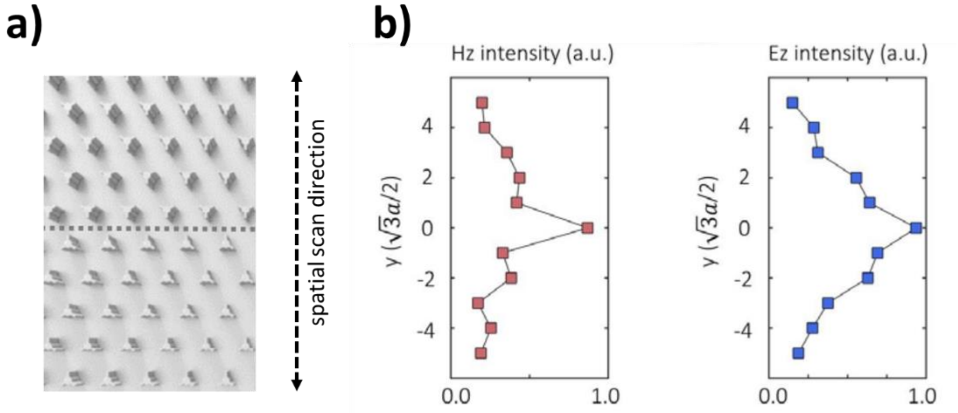

Figure 6.6 The edge scan of the QVH/QVH interface. a) the configuration of the spatial edge scan along the transversal direction respect to the exit of a straight topological interface. b) $\mathrm{E_z}$ and $\mathrm{H_z}$ components of transmitted TE (red) and TM (blue) respectively. The decaying tails away from the interface are apparent in both cases. Courtesy of Fei Gao.

Furthermore, the topological protection resulted from valley DOF is underscored by a defect test which the introduction of the defect breaks the C_3-symmetry in unit cell as shown in the Figure 6.7a. A unit cell at the topological interface between QVH PTIs is replaced by a square cylinder which is not C_3-symmetric object. This tiny perturbation to the interface produces significant enhancement in reflected signal (~30dB) in Figure 6.7b. This could be easily understood by realizing that the EM waves are reflected back to the launching point from this defect since the topological protection is no longer present.

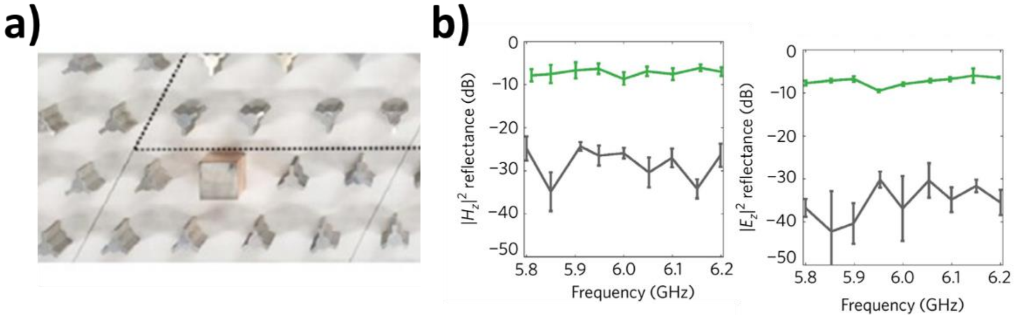

Figure 6.7 Defect test of TPEWs transport on QVH PTI platform. a) Location of the defect (a square cylinder) at the interface. b) Measured reflectance of TE and TM modes respectively. Black curves are the reflectance from the zigzag domain wall. Green curves are for the case when a square metallic rod replaces one tripod at the domain wall, as shown in a. Error bars represent the standard deviation of multiple measurements. Courtesy of Fei Gao.

Note that in order to justify the reflectance measurement one has to excite unidirectionally propagating wave so that one can univocally claim the captured signal is from the scatters and not from the launching transmitter. The method of unidirectionally exciting the TPEWs on the QVH PTIs together with that on the QSH PTIs is omitted in this section for now and will be covered in the next chapter.

Finally, we proceed to demonstrate the unique feature of the PTI preserving valley DOF, namely the topologically protected refraction at the valley-preserving zigzag termination of the QVH PTIs into the empty space in the parallel-plate waveguide. The reflectance of the TE and TM mode is measured with unidirectional excitation. Nearly vanishing reflectance is observed across the entire bandgap Figure 6.8a and Figure 6.9a.

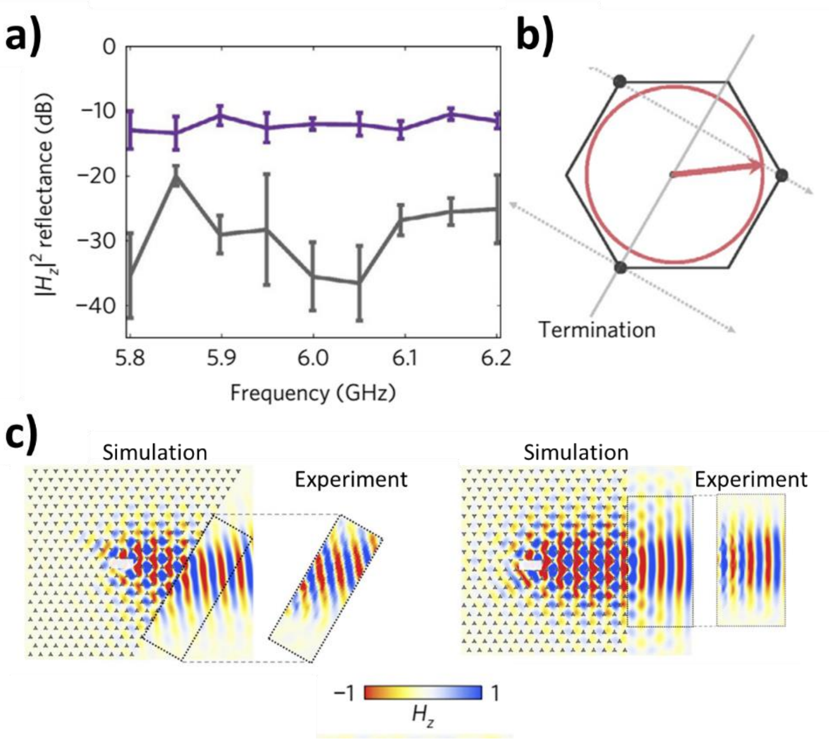

Figure 6.8 Topologically protected refraction of TE-polarized TPEW into an empty waveguide region. a) Measurement of $|\mathrm{H_z}|^2$ reflectance for zigzag (grey) and armchair (purple) terminations. Error bars represent the standard deviation of multiple measurements. b) The iso-frequency analysis on the out-coupling of the TE polarization. Red circle: dispersion of TE modes in the parallel-plate waveguide, black dot: K' valley. c) The spatial scan at $\mathrm{f} = 6.12\mathrm{GHz}$ indicating the refraction of TE states through the zigzag (left) and armchair (right) termination. The white bars indicate the position of phase-arrayed dipoles. The insets are the experimentally measured field patterns. Courtesy of Fei Gao.

Experimentally scanned empty-space field patterns at $\mathrm{f} = 6.12\mathrm{GHz}$ for zigzag and arm-chair terminations are plotted in Figure 6.8c and Figure 6.9c where excellent agreement can be found between measured and simulated field patterns. In addition, the direction of the refracted angle can be fully-explained by the phase-matching condition from the iso-frequency analysis in Figure 6.8b. On the other hand, the armchair termination is not valley-preserving and thus creates backscattering at the termination which builds up the reflectance by generally one order of magnitude compared to zigzag termination.

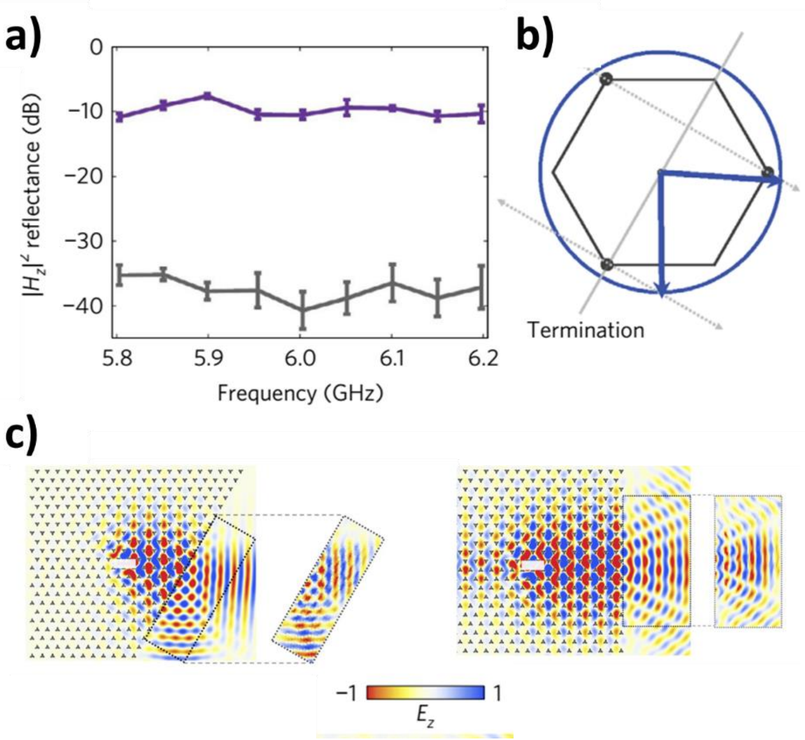

Figure 6.9 Topologically protected refraction of TM-polarized TPEW into an empty waveguide region. a) Measurement of $|\mathrm{E_z}|^2$ reflectance for zigzag (grey) and armchair (purple) terminations. Error bars represent the standard deviation of multiple measurements. b) The iso-frequency analysis on the out-coupling of the TM polarization. Blue circle: dispersion of TM modes in the parallel-plate waveguide, black dot: K' valley. c) The spatial scan at $\mathrm{f} = 6.12\mathrm{GHz}$ indicating the refraction of TM states through the zigzag (left) and armchair (right) termination. The white bars indicate the position of phase-arrayed dipoles. The insets are the experimentally measured field patterns. Courtesy of Fei Gao.

Similarly, the TM-polarized TPEWs shows the same topologically protected refraction as the TE-polarized TPEWs. However, it is worth noting a major difference that the dispersion relation of TM-mode in the parallel-plate waveguide is different from the that of TE-mode. In Figure 6.9b, the resulting iso-frequency contour of the TM-polarized wave is a circle with larger radius laying outside of the FBZ which consequently predicts two out-coupling lobes into the empty-space waveguide whereas there is only one solution in the case of TE-polarized TPEWs as in Figure 6.8b.

The above results demonstrate the topologically protected refraction of robust kink states into the ambient space defined by an unpatterned parallel-plate waveguide. The polarization multiplexing can double data capacity to support robust and high-speed wireless and optical data networks. Due to the high efficiency of the coupling between the topological modes and free space modes, we anticipate many practical applications for directional antennas, lasers, and other communication devices across the electromagnetic spectrum.

6.3 SUMMARY AND COMMENT

In summary, we address a QVH PTI with the following unique features which will be experimentally demonstrated in the later chapter. First, our design is based on a four-band model that allows polarization multiplexing. Thus, two pairs of kink states with transverse-electric (TE) and transverse-magnetic (TM) polarizations can be selectively excited, whereas previous studies based on the two-band model can host only one pair of kink states in a monolayer structure.

Second, the kink states can out-couple, or refract, with nearly perfect efficiency into ambient space, with promising applications for directional antennas, lasers and displays based on topological modes. This form of refraction has never been demonstrated before with topological edge modes and is fundamentally different from ordinary light refraction at the Brewster angle, which applies only to plane waves with a specific polarization. In the latter chapter, we are able to demonstrate spin–valley-locked topological transport. For a spin–valley-locked kink state, even though the spin conservation is broken, the conserved valley symmetry can still guarantee topologically protected out-coupling behaviors.

Chapter 7 Selective Mode Excitation on PTI Platforms

7.1 GENERAL IDEA OF MODE EXCITATION

The excitation of a waveguide is often discussed in the context of the coupling efficiency where the input impedance of the feeding source is matched to waveguide to maximize the power delivery to waveguide. Particularly, selective mode excitation, launching solely prescribed propagating modes of a waveguide, is occasionally persuaded when the mode purity is critical to the system under study.

Realizing the fact that Maxwell's equations is a set of differential equations destined by the boundary conditions, the rule of thumb to selective mode excitation is to match the input source to the field pattern of desired eigen modes in a waveguide. It might seem trivial to selectively excite TPEWs on the previous PTI platforms because the PBG forbids all EM wave propagation except for the edge states so a source feeder operating in this PBG would certainly excite TPEWs. However, to excite a specific mode the supported TPEWs requires further effort to match the field pattern in spatial as well as temporal manner. In this chapter, methods of unidirectional excitation on the QSH PTI and QVH PTI platforms will be covered and experimentally demonstrated based on collaborated publications with Maryland and Nanyang Technological University[3].

---

[3] The content of this chapter is modified from prior publications [50,52] and from the following publication: Xiao, B., Lai, K., Yu, Y., Ma, T., Shvets, G. and Anlage, S. M., "Exciting reflectionless unidirectional edge modes in a reciprocal photonic topological insulator medium". *Phys. Rev. B* **94**, 195427 (2016). The author supported to the unidirectional excitation experiment and contributed to manuscript writing.

7.2 UNIDIRECTIONAL EXCITATION ON QSH PTI PLATFORM

7.2.1 Excitation of Circular Polarized TPEWs

This section is modified from the joint publication with University of Maryland [55]. The experiment of unidirectional excitation is designed to take place in the fabricated QSH PTI platform in UT as previously covered in Chapter 5 due to large crystal size to suppress bulk modes.

The spin-up and spin-down edge modes on QSH PTI platform have opposite handedness in CP basis and the direction of propagation is locked to the spin state, allowing for unidirectional TPEW propagation depending on the sense of rotation of the magnetic dipole antenna where a right circularly polarized magnetic dipole only excites the right-going modes which implies the chirality of the wave transport.

In order to efficiently excite the TPEW in the QSH PTI platform, the source must be placed in a location where the edge mode field is most intense and it must generate a field profile that matches the edge mode at that location. By inspecting the numerical simulated profiles of the magnetic field projected onto the circularly polarized basis for the spin-up and spin-down eigenmodes, the $5.5\ \mathrm{mm}$ air gap between the metal plate and the cylinder rod is identified as the best place to locate the source. At that location the field profile is a rotating magnetic dipole around the center frequency of $6.08\ \mathrm{GHz}$. The right circularly polarized component of the magnetic field is maximized for the forward-propagating spin-up eigenmodes and vanishes for the backward-propagating spin-down eigenmodes.

Mechanically rotating a loop antenna at a rate of the order of 109 revolutions per second is impractical to be implemented in such limited space. Instead, we use two loop antennas, perpendicularly positioned to each other, with two $\mathrm{f} \sim 6\mathrm{GH}$ sinusoidal input voltage waves with variable phase shift $\mathrm{v_A(t)} = \mathrm{V_A cos(\omega t)}$ and $\mathrm{v_B(t)} = \mathrm{V_B cos(\omega t} +$

φ) for antennas A and B respectively. By setting $V_A = V_B$ and $\varphi = +(-)\pi/2$, a clockwise (or counterclockwise) rotating magnetic dipole is mimicked. Furthermore, by tuning φ one can continuously vary the amplitude of the left- or right-going modes, providing more control over the directivity.

7.2.2 Experimental Result and Discussion

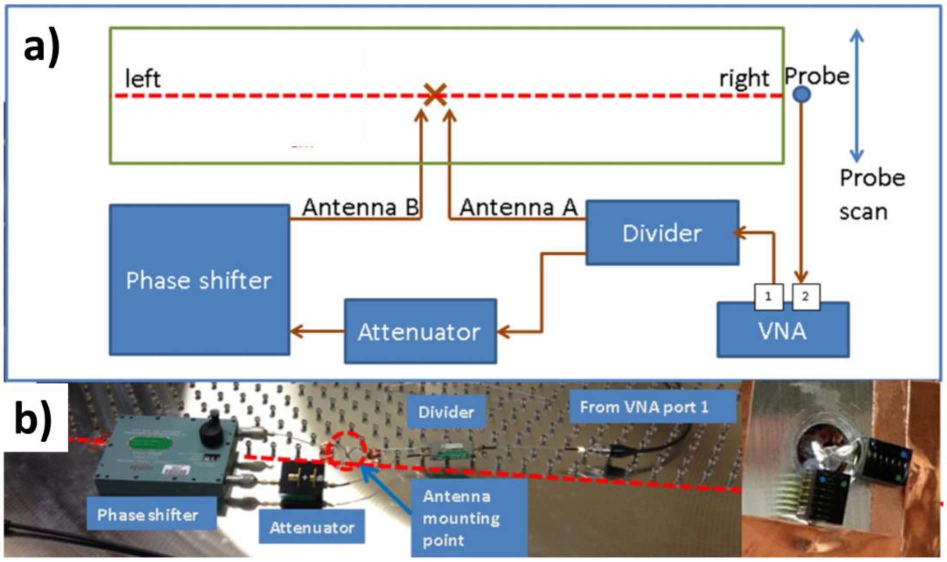
a)
left
right
Probe
Probe scan
Antenna B
Antenna A
Divider
Phase shifter
Attenuator
1
2
VNA
b)
Divider
From VNA port 1
Phase shifter
Attenuator
Antenna mounting point

Figure 7.1 Experimental setup for unidirectionally excite TPEWs on QSH PTI platform. a) Schematic of source feeding and location of antennas. The topological interface is denoted by the red dashed line. (b) Photograph of setup described in a). Inset: Arrangement of the two loop coils which are in the air gap of a cylinder at the interface.

As shown in Figure 7.1a, the source feeding of the said two loop antennas is from the first port of the VNA and that output signal is split approximately in half by a HP87304C power divider, creating two branches. One branch goes directly to loop antenna A, while the other one is connected to a variable attenuator and variable phase shifter before going to the other loop antenna, B. The two loop antennas are in fact air-core RF coil inductors (Coilcraft model No. 1812SMS-56NJLB; $R = 6.2\ m\Omega$, $L = 56nH$ at 150 MHz) with one end grounded to the metal plate and the other end soldered onto the center conductor of the feed coaxial cable, as shown in the inset in Figure 7.1b. Hence the input signal from the VNA is divided, phase-shifted, and then sent to the two RF coils, which each create a magnetic dipole by controlling the value of the phase shift, it can produce a linearly, circularly, or elliptically polarized magnetic dipole source.

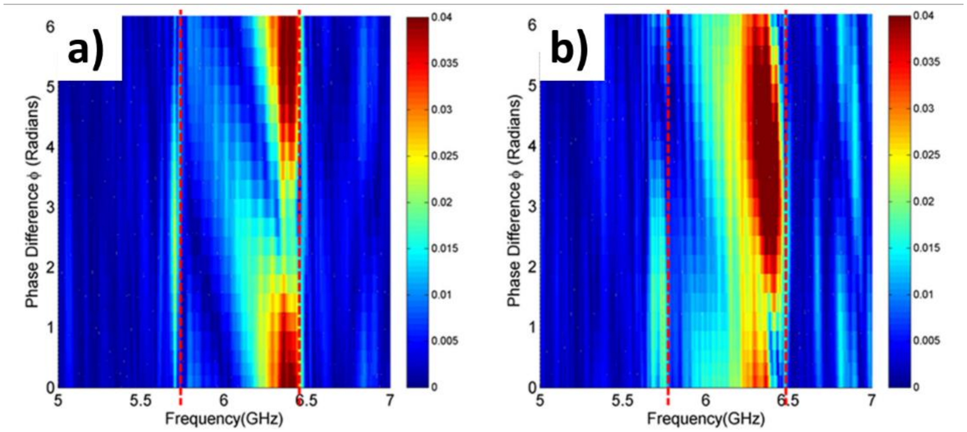

Figure 7.2 Transmission amplitude on the a) left side and b) right side of the PTI platform as a function of the frequency while the phase difference ϕ of the two launching loop antennas is varied from 0 to 2π. The probe is positioned at the center of the edge. The BMW bulk band gap extends from 5.80 to 6.47 GHz, as shown by the dashed vertical lines.

A transmission experiment is performed by placing a simple electric dipole antenna at the edge of the QSH PTI platform on either the left or the right side where the interface comes to the edge to pick up and record the transmitted signal at port 2 of the VNA. We then move the probe along the edge to do spatial edge scan while recording the transmission amplitude as a function of the probe's location and also the phase difference between the two loops. The experimental result for the transmission when the probe is at the midpoint of the edge is shown in Figure 7.2. From the midpoint transmission plot, the excited wave propagates primarily to the left (right) when the phase difference is close to 2π (1.27π), confirming the successful excitation of a predominantly unidirectional edge mode. It is also clear that the transmission has a period of 2π with respect to the phase difference in the frequency range from $5.80\mathrm{GHz}$ to $6.47\mathrm{GHz}$, which corresponds to the plateau of enhanced transmission.

Naively, it is expected that when $V_A = V_B$ and $\phi = \pi/2$, a clockwise-rotating magnetic dipole would excite a purely left- or right-going TPEW, depending on whether the dipole is placed at the lower or upper air gap, and thus the left transmission should reach its maximum while the right transmission should vanish. However, the experiment is affected by several physical limitations causing nonidealities beyond our control. For instance, the two loop antennas are of finite sizes and cannot be overlapped on top of each other, the geometry is also different giving rise to the uneven feeding, the coupling efficiency to the edge mode, and the actual power received from input feed lines. Henceforth we must loosen the restrictions on V_A, V_B, and ϕ to obtain a more general result. To keep the total input power constant while giving the two loop antennas variable portions of the power, we parametrize the amplitudes of the driving voltage waves with an angle θ as $V_A = V_0\cos\theta$ θ and $V_B = V_0\sin\theta$, where $\theta \in [0,2\pi]$.

We performed a numerical simulation of a finite-size PTI structure, whose detailed geometry can be found in the supplemental information [55]. The simulation calculates the transmission from antenna A and B to the left- and right-side probes and expresses it as a 2×2 scattering matrix, $S_{sim} = \begin{bmatrix} S_{LA} & S_{RA} \\ S_{LB} & S_{RB} \end{bmatrix}$,where S_{ij} is the transmission from j to i, L (R) represents the left-side (right-side) probe, and A and B represent antennas A and B respectively. This driven simulation is calculated with the package of using CST

Microwave studio. Given the simulation result of $\mathrm{S_{sim}}$, and that $\mathrm{V_A = V_0 cos\theta}\ \theta$ and $\mathrm{V_B = V_0 sin\theta}$ (to keep the total input power constant), we can calculate the transmission to the left or right side at different driving amplitudes in the two antennas (θ) and different phase shift values (ϕ). To calculate transmission to the right side, for instance, one has

$$\mathrm{V_R = V_A S_{RA} + V_B e^{-i\phi} S_{RB} = V_0\left(S_{RA} cos\theta + e^{-i\phi} S_{RB} sin\theta\right)} \qquad (7.1.1)$$

where $\mathrm{e^{-i\phi}}$ controls the phase difference between antenna A and antenna B. Figure 7.3 shows the resulting transmission to the left and right probes as a function of θ and ϕ, at two frequencies within the bulk band gap of the PTI structure. Since S is frequency dependent and is simulated over the whole band gap, choosing a different frequency could lead to a different plot but the unidirectional propagation property should remain.

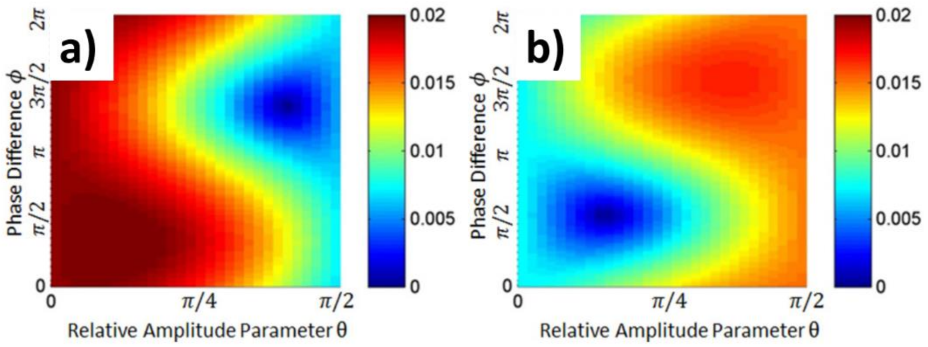

Figure 7.3 CST simulation results for transmission amplitude on the left and right sides of the QSH PTI structure while both the phase difference ϕ and the driving amplitude (parameterized by angle $\theta \in [0,2\pi]$) of the two loop antennas are varied. Results are shown for a) left side and b) right side at 6.08GHz.

The first observation of the Figure 7.3 is that when the transmission to the left side is at its maximum, the transmission to the right side is not necessarily vanishing and is not at its minimum although it is in the vicinity of the minimum point which confirms the nonideality in the experimental setup mentioned in earlier paragraph. More importantly, one can effectively eliminate the transmission to one side although the transmission to the other side is not at its maximum and by doing so one can achieve contrast ratio between left-going and right-going wave could achieve 1 part in 10^4 as shown in the later analysis. In short, the strategy of this unidirectional excitation study is to suppress the undesired mode for higher mode purity instead of persuading high coupling efficiency for desired mode.

This phenomenological model can be used for selective feeding of a waveguide in either direction. This can be used to feed a beam-forming array of antennas through a series of sensitive and rapidly tunable structures. The current design can also handle high microwave powers, making it attractive for transmit applications. Since the directivity of the edge modes can be varied by ϕ, it can be used as a modulation method for communications.

To sum up, we have experimentally demonstrated excitation of a unidirectional edge mode using a rotating magnetic dipole antenna consisting of two perpendicular coils. The edge mode in this time-reversal symmetry-preserved QSH PTI platform has been demonstrated to be unidirectional. In addition, the degree of directionality can be tuned continuously using the method that we have outlined here, allowing for novel applications in the field of communications, for example, phased array antennas.

7.3 UNIDIRECTIONAL EXCITATION ON QVH PTI PLATFORM

7.3.1 Excitation of Valley-Polarized TPEWs

Different from the CP basis in the QSH PTI in the previous section, the basis used to describe field pattern of QVH PTIs can be characterized by the angular quantum numbers (AQNs) $n = \pm 1$. Accordingly, the unidirectional excitation of valley-polarized wave is demonstrated using a four-antenna phased array in the recent study [56]. The content of this section, however, is not attempted to repeat the said publication, but rather to provide a simple method of preferentially exciting a specific mode of the TPEWs on QVH PTI platform in order to substantiate the result of the reflectance measurements in Chapter 6.

7.3.2 Experimental Result and Discussion

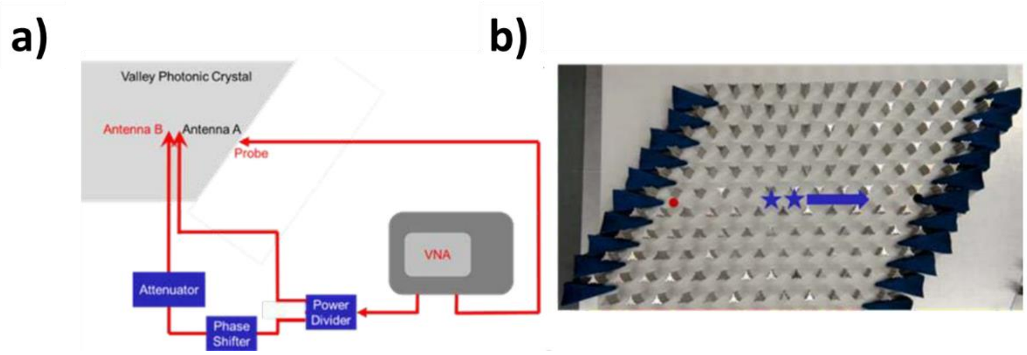

Figure 7.4 Unidirectional excitation of TPEWs on QVH PTI platforms. a) Schematic of a similar signal feeding setup as in the Figure 5.2. b) Photo of sample for unidirectional excitation calibration. Blue stars represent the phase array source. Red and black dots indicate minimum and reference probe positions. Blue cones are electromagnetic absorbers

The employed experimental setup of the unidirectional excitation in Figure 7.4a follows the same logic as in the QSH PTI case in Figure 7.1. The parameters of unidirectional excitation are experimentally extracted from measuring the sample Figure 7.4b. The two zigzag terminations are enclosed with tapered absorbers to reduce the reflection from the boundary of the crystal due to impedance mismatch.

By tuning the phase shifter and attenuator, namely changing θ and ϕ, we can achieve extremely low signal at the left side (red dot) in Figure 7.4b, and a large signal at the right side (black dot) which is recorded as the reference. We changed the probing positions at the left side, which still show extremely low signal. This process can double confirm the extremely low signal at the left side, thus the unidirectional excitation.

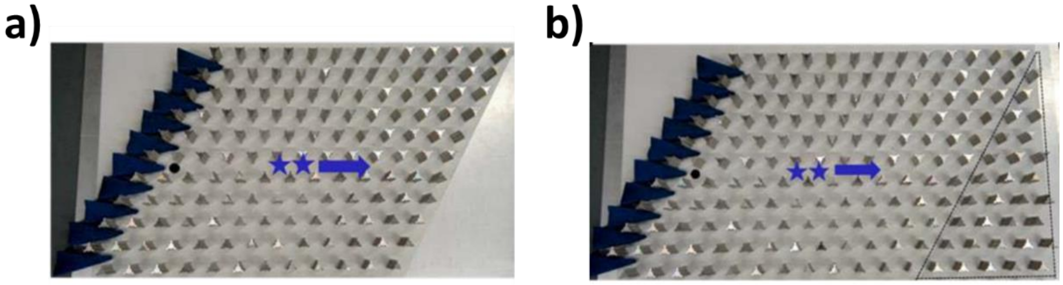

Figure 7.5 Photos of reflectance measurement setup in Chapter 6. a) Photo of zigzag termination. b) Photo of armchair termination. Blue stars represent the phase array source. Black dot indicates probing positions. Blue cones are electromagnetic absorbers

Then, we start to measure the reflectance of both zigzag and armchair terminations. Firstly, we removed the right absorbers as shown in Figure 7.5, and probe the signal at the left black dot. This signal is from the reflection of zigzag termination. Secondly, we add the structure highlighted with dashed triangle (shown in Figure S5d). The signal is from the reflection of the armchair termination. In the spectral range of PBG, we take 9 frequency points for reflectance measurement. For each frequency point, we repeat above reflectance measurement 5 times.

7.4 SUMMARY AND COMMENT

In summary, methods of unidirectional excitation on the QSH PTI and QVH PTI platforms are introduced based on the profile matching analysis. A simple preferential excitation source consisting two-antenna array is proposed according to the basis of field profile on QSH PTI and QVH PTI respectively. Specifically, a phenomenological model is developed on the QSH PTI platform to predict the mode purity under ideal conditions. The experimental demonstrations of both platforms are shown to provide high ratio between prescribed mode versus undesired modes.

Chapter 8 Applications Based on PTI Platform

8.1 COMPACT BROADBAND RF DELAY LINE

8.1.1 Reflection-less Compact RF Delay Line

A delay line is a simple device to produce a prescribed time delay in a transmitted signal which finds various functions in practical instrumentations, such as oscilloscope event triggering, echo effect in acoustic amplifier, data buffering in early television standard, and digital signal processing. The most straightforward method of achieving this delay is to provide an extra path of wave propagation so the input signal travels over a longer path and transmits to the output with additional lapsed time. Preferably, the property of this path is bound to be similar to the input/output channels with low dispersion to minimize insertion loss as well as signal distortion. On top of that, it is desirable to suppress the cross-talking among such devices granting the capability to increase the time delay by stacking devices in serial.

These requirements make the robust and reflection-less wave transport on the TPEW platform a highly potential candidate for a broadband RF delay line application. For example, a detour-type lattice defect shown in Figure 5.6 introduces a time delay

$$\tau = \frac{1}{2\pi}\left(\frac{\partial \phi_{\mathrm{def}}}{\partial f} - \frac{\partial \phi_{\mathrm{str}}}{\partial f}\right) \tag{8.1}$$

where $\phi_{\mathrm{str}}(f)$ and $\phi_{\mathrm{def}}(f)$ are the phases of the transmitted EM waves for the straight and defect-interrupted interfaces.

The key advantage of topologically protected delay lines is their compactness: TPEWs can make sharp turns into tightly-packed phase-delaying detours without any backscattering. By loading a straight PTI interface (which plays the role of a bus waveguide for the propagating TPEWs) with a sequence of phase-delay defects (Figure 8.1, top), nearly arbitrary phase profiles $\phi_{\mathrm{def}}(\mathrm{x,f})$ can be generated and subsequently used in a variety of applications, including frequency-division multiplexing for free-space wireless communications and terahertz wave generation. The detour defect shown in Figure 8.2b and c can be viewed as a building block for these applications.

8.1.2 Experimental and Theoretical Demonstrations

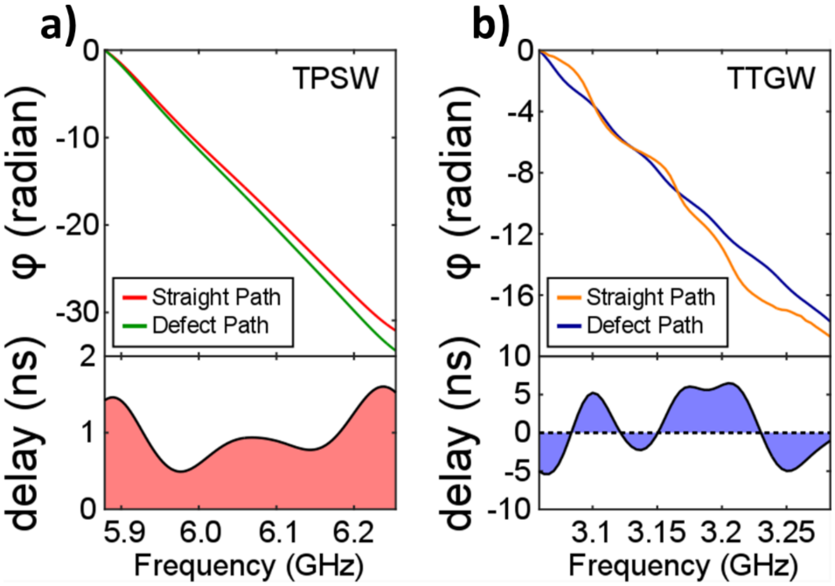

Figure 8.1 Photonic delay line applications based on QSH PTI. Top half: the relative phases extracted from the transmission spectra of straight path and defect path; bottom half: the time delays of delay line application on the platforms of (a) TPEWs and (b) TTGWs.

The experimentally measured phase and time delays of the transmitted TPEWs are plotted in Figure 8.1a for the straight and defect-interrupted interfaces. Note that $\tau(f) > 0$ everywhere inside the gap, although considerable fluctuations are observed at the edges of the gap, where the amplitude of the transmitted TPEW is reduced due to incomplete topological protection. However, for most frequencies the time delay is spectrally flat. In contrast, without topological protection, the delay time of TTGWs is a rapidly-varying sign-changing function of the frequency inside the topologically trivial bandgap.

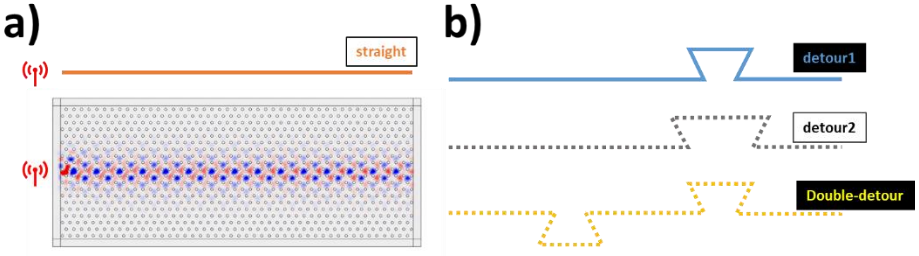

Figure 8.2 Schematic of full-size time delay simulation. a) straight path as the baseline for calculating time delay. b) various paths of wave propagation. Cyan line: path with one detour (the same as in experimental measurement), gray dashed line: path with one elongated detour, yellow dashed line: path with two detours. Color: energy density of spin-up (rightward propagating) wave. The launching probe locates at the leftmost edge of the structure.

Note that the time delays for the TTGWs can be negative around the Fabry-Perot (FP) resonances of the detour. Negative time delays are not observed for the detoured TPEWs because topological protection against backscattering prevents FP resonances. This observation seems to be counterintuitive at the first glance: why signal travels faster in a path with detour than in a straight path? This puzzle could be explained by following the line of Wigner delay time [57]. These experimental results constitute the first step in building a multi-stage broadband topologically protected delay line capable of buffering multiple electromagnetic pulses.

The time delay can be indefinitely increased by stacking multiple detour defects. For example, two detours produce twice the delay time for the transmitted TPEWs, with no decrease in the bandwidth because of the lack of interaction between adjacent defects due to topological protection. In Figure 8.2, a set of full-size simulations has been calculated to validate this claim. Three instances of delay line are constructed in the model: the first configuration consists of a straight bus channel and a detour which is the same as measured in the experiment; the second is in a similar setup but with a larger detour; the last one is a bus channel with two detours in the path. The time delay is then extracted and fitted with linear curves in Figure 8.3 below.

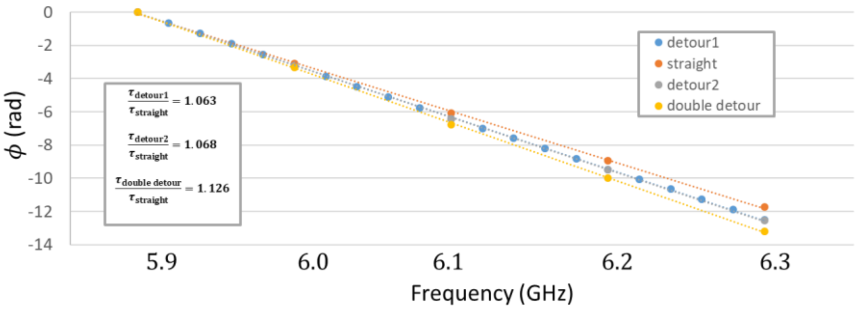

Figure 8.3 Calculated time delays of various configurations in Figure 8.2.

The first observation is that the ratio of the detour 1 agrees to the experimentally measured value ($\tau_{\text{detour}}/\tau_{\text{straight}} = 1.069$) with less than 1% discrepancy. In addition, one can easily point out that the total distance of travel is in fact same for both detour-1 and detour-2 because the elongated part in the detour-2 evens out the shorten travel length in the bus channel. As a result, the value deviates from the case of detour-1 negligibly. Finally, the path consisting of two detours surely introduces twice the extra path and thus possess two-fold elapsed time.

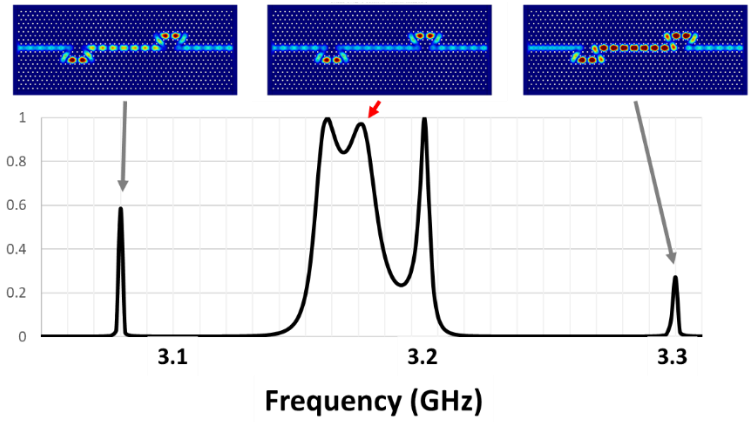

Figure 8.4 Transmission spectrum of TTGWs on path with double detours. The scale is normalized to the highest peak of resonance tunneling. Insets: the profile of energy density at transmission peaks. Red arrow: the FP resonance peak, grey arrows: extra transmission peaks of cross-talking in the waveguide.

On the contrary, using two detour-type defects in a topologically trivial waveguide (Figure 8.4) reduces the operating bandwidth for TTGWs. Even the delay could be increased by stacking two detours in series, the overall delay-bandwidth product is in fact less as shown in the Figure 8.5 due to the fact that the signal tunnels through the device via the resonance effect. On top of that, since back-scattering is no longer suppressed, the cross-talking inevitably takes place and causes EM waves to bounce back and forth in between two components. Consequently, this interaction manifests as two extra transmission peaks ($f \approx 3.08\text{GHz}, 3.3\text{GHz}$) as indicated in the inset of Figure 8.4.

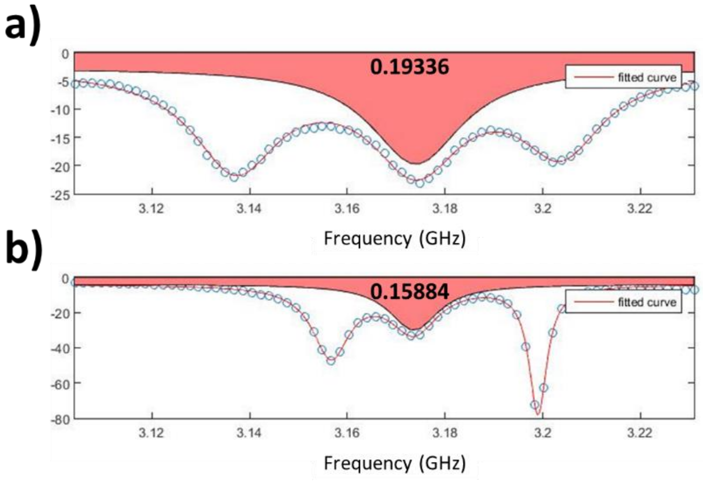

Figure 8.5 Stacking two TTGWs delay line for the spectral position indicated by the red arrow in Figure 8.4. The platform consists of one bus waveguide and with of a) one detour, b) two detours. Note that the elapsed time of the straight path is not subtracted in this figure. Blue circle: calculated elapsed time, red curve: curve fitting of a Lorentz function. The number representing the area of shaded area below the curve, which is effectively the integrated DBP over the spectral range of interest.

8.1.3 Summary and Comment

In summary, we experimentally realized in the microwave frequency range a delay line based on a quantum spin Hall photonic topological insulator. Topological protection of localized surface waves between two PTIs resulted in reflection-less spectrally uniform time delays of several wave periods that were induced by a compact sharply-edged detour-type defect. Because such defects can be of nearly arbitrary shapes and sizes, we anticipate that novel geometries for compact wave buffers and delay lines utilizing topological photonic transport will emerge across the electromagnetic spectrum, from micro- to infrared waves.

8.2 VALLEY-SPIN SORTING PLATFORM

8.2.1 Introduction to Valley Wave Sorting Platform

The next example stems from the fact that the platform implementing two independent binary DOFs grants more functionalities compared to platform with only one binary DOF. In this section, we experimentally demonstrate a valley wave sorting platform based on the valley-spin-locked edge waves at the heterogeneous interface between two photonic crystals with independent topological invariants, namely spin-Chern number and valley-Chern number in the QSH PTIs and QVH PTIs respectively. Such a domain wall supports edge states propagation according to the topology of the bordering PTIs which suggests that one can choose to enable or suppress a specific edge states in a channel by changing the topology of the PCs.

Working with this idea, it is then straight forward to consider the platform layout with a junction connecting three channels: one of which is a unidirectional input, the rest two are outputs supporting different edge states. Specifically, we choose to input the wave on the QSH/QSH interface to acquire one-way propagating mode toward this junction and dispatch the valley-polarized waves into two QSH/QVH channels with opposite valley-spin locking to sort waves according to its valley polarization[4].

8.2.2 Framework of Implemented Topological Indices

The topologically protected edge waves at a heterogeneous QSH/QVH interface have been constructed from a 4-band model in the previous chapters and the will again be briefly recapped here for the sake of readability. Also, note that Δ_{em} in Chapter 5 is now relabeled as Δ_{SOC}. In the case of QSH PTI, the spin DOF is constructed from the in-phase and out-of-phase relation between degenerate TE and TM modes at K/K' points. The electromagnetic modes propagating above and below the bandgap have a QSH-like topological nature with a spin-Chern number given by $2\mathrm{C}_{\uparrow/\downarrow,\mathrm{v}}^{\mathrm{SOC}} = \pm 1 \times \mathrm{sgn}(\Delta_{\mathrm{SOC}})$, where $\mathrm{s} = \uparrow, \downarrow$ is the spin label, $\mathrm{v} = \mathrm{K}, \mathrm{K}'$ is the valley label, and the valley-independent perturbation strength $\Delta_{\mathrm{SOC}} > 0$ ($\Delta_{\mathrm{SOC}} < 0$) if the bottom (top) cylinder-to-plate gaps are closed with metal filling.

---

[4] The content of this chapter is modified from a prior uploaded manuscript. Lai, K., Yu, Y., Han, Y., Gao, F., Zhang, B. and Shvets, G. "Sorting and Routing Topologically Protected Edge States by their Valleys". arXiv: 1712.04589. The author designed, fabricated, supported the experimental measurements and contributes to manuscript writing.

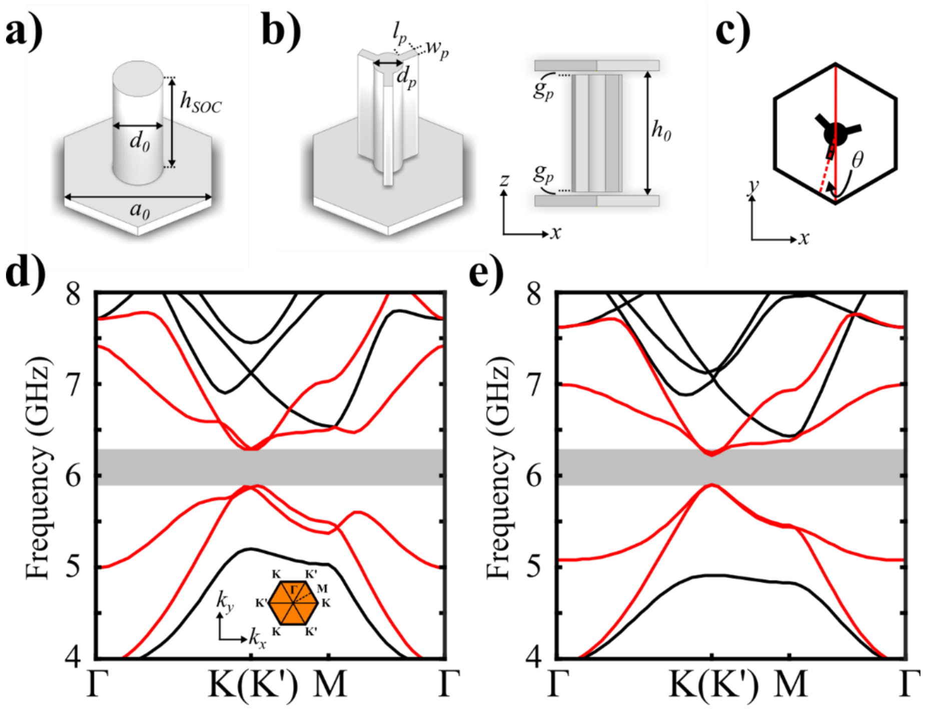

Figure 8.6 Designs of photonic crystal with non-trivial topology. a) QSH PTI. b) QVH PTI. c) Schematic unit cell of QVH PTI illustrating rotation angle θ between the tip of tripod (red dashed line) and negative y-direction (red solid line). The symmetry-breaking perturbation is maximized at $\theta = 0°$ ($\Delta_{\mathrm{P}} > 0$), $60°$ ($\Delta_{\mathrm{P}} < 0$). d) dand e) Calculated photonic band structures of d) QSH PTI and e) QVH PTI at $\theta = 0°$. Red curves: topologically non-trivial modes; black curves: dispersion of bulk modes; gray shaded area shows a complete photonic bandgap centered at $f_0 = 6.08\mathrm{GHz}$ with 7% bandwidth.

Similarly, the valley-preserving perturbation of the QVH PTI is imposed by deforming cylinder of the unperturbed design into a tripod-like, C_3-symmetric shapes shown in Figure 8.6b that breaks the in-plane inversion symmetry with respect to the principle axes of hexagonal lattice in Figure 8.6c. It is essential to match the perturbation strength of TE and TM modes so that the perturbed structure becomes QVH PTI and henceforth supports propagating electromagnetic waves below the bandgap in Figure 8.6e with a spin-independent valley-Chern number $2C^{\mathrm{P}}_{\mathrm{s},\mathrm{K}/\mathrm{K}'} = \pm 1 \times \mathrm{sgn}(\Delta_{\mathrm{P}})$, where Δ_{P} is the perturbation strength of the inversion symmetry breaking. The width of this bandgap is proportional to Δ_P which can be controlled by rotating the tripods with respect to the principle axes and is maximized at $\theta = 0° \ (\Delta_P > 0), 60° \ (\Delta_P < 0)$ where the strongest perturbation happens. It is worth noting that a critical step toward implementing independent DOFs onto one common platform is to match the bandgap of QVH PTIs with the bandgap of QSH PTIs so that the edge states could reside in the same spectral range as indicated in Figure 8.6d and e.

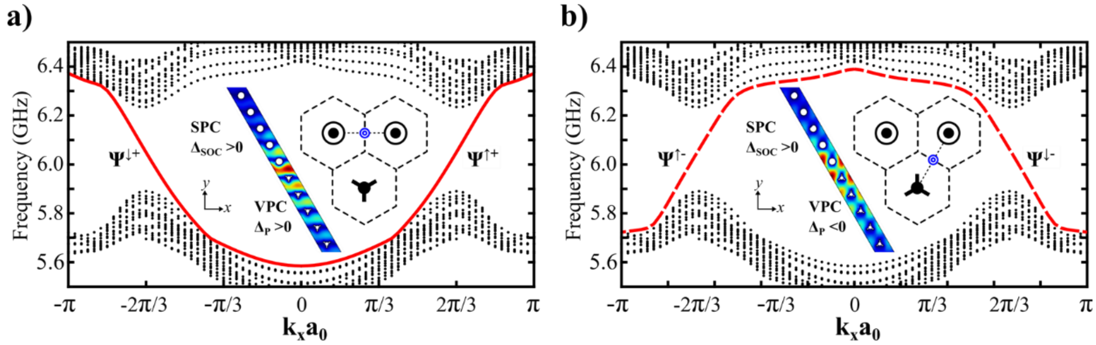

Figure 8.7 TPEWs with valley-spin locking propagation. Photonic band diagrams of a heterogeneous interface between: a) QSH/QVH PTIs ($\Delta_{SOC} > 0, \Delta_P > 0$) b) QSH/QVH PTIs ($\Delta_{SOC} > 0, \Delta_P < 0$). The band structure is calculated with a supercell with periodicity a_0 along X-direction and 15 cells on each side of the domain wall. Red solid curves: positive index TPEW; red dashed curves: negative index TPEW; black dots: bulk modes; edge modes are denoted with positive/negative $(+/-)$ indices and up/down $(\uparrow/\downarrow)$ spins. Inset: $|E_z|$component for two kinds of QSH/QVH interfaces in supercell simulation (only 10 cells are shown); blue double circles: locations of low $|E_z|$ value at the vicinity of domain wall for preferential mode excitation.

Building upward from the laid foundation, a heterogeneous interface could be constructed using QSH PTIs and QVH PTIs on this common platform. Indeed, such an interface locks the relation of spin- and valley- DOFs at the domain wall, thus supports specific valley-spin locked TPEWs propagation. For example, the supercell simulation in

Figure 8.7a suggests the domain wall between QSH PTI with $\Delta_{\mathrm{SOC}} > 0$ and QVH PTI with $\Delta_{\mathrm{P}} > 0$ supports wave propagation with locked down DOFs, namely spin-up wave at K' point and spin-down wave at K point.

This locking could be easily understood using symbolic notation according to the principle of bulk-boundary correspondence. In the case of Figure 8.7a, the only two existing edge states are a spin-up wave at K' point: $\mathrm{C}_{\uparrow,\mathrm{K}'}^{\mathrm{SOC}} - \mathrm{C}_{\uparrow,\mathrm{K}'}^{\mathrm{P}} = +1/2 - (-1/2) = 1$ and a spin-down wave at K point: $\mathrm{C}_{\downarrow,\mathrm{K}}^{\mathrm{SOC}} - \mathrm{C}_{\downarrow,\mathrm{K}}^{\mathrm{P}} = (-1/2) - (+1/2) = -1$ since the outcome of the rest two combinations are zero. On the other hand, the same principle gives to a spin-up wave at K point and a spin-down wave at K' point at the interface between QSH PTI with $\Delta_{\mathrm{SOC}} > 0$ and QVH PTI with $\Delta_{\mathrm{P}} < 0$ for the interface in Figure 8.7b.

An important insight could be deduced from these PBSs that the dispersion relation of edge states in Figure 8.7a acts like a EM wave propagates in a medium with positive refractive index as the group velocity is positive (negative) at positive (negative) k_{x} and the other way around for the edge states in Figure 8.7b. Therefore, the TPEWs will be referred as positive index mode $\Psi^{\uparrow/\downarrow +}$ in Figure 8.7a and as negative index mode $\Psi^{\uparrow/\downarrow -}$ in Figure 8.7b from this point on. It is also worth noticing a fact that the color plots of $|\mathrm{E}_{\mathrm{z}}|$ component in the insets are spatially dissimilar to each other for both modes. Particularly the low strength spots (blue double circles in schematics) locate differently in Figure 8.7a and b. This provides a control handle to preferentially excite one of two modes. In other words, one can launch more energy into one mode by placing a linear antenna along z-axis at the low strength spot of the other mode. This idea will be thoroughly examined in the later part of this section.

8.2.3 Experimental Realization of the Sorting Platform

To fully utilize both modes of TPEWs and to further demonstrate the functionality of valley waves sorting, a platform consisting of 15×15 unit cells has been proposed and fabricated in Figure 8.8a. The fabricated platform is then measured using the RF test station described in Chapter 5. The aluminum tripod of QVH PTI is fabricated using wire electrical discharge machining (wire EDM). The structural foam (ROHACELL 51HF) is used on both ends to support the tripod in the center of parallel plates waveguide. Another piece of structural foam is laser-cut into a mask to orient the direction of tripods.

The platform is partitioned into three bordering domains of PCs, which are QVH PTI with $\Delta_{\mathrm{P}} > 0$ at $\theta = 0°$ (yellow shaded area), QSH PTIs with $\Delta_{\mathrm{SOC}} > 0$ (green shaded area) and $\Delta_{\mathrm{SOC}} < 0$ (blue shaded area). The domain wall between QSH/QSH ($\Delta_{\mathrm{SOC}} > 0$, $\Delta_{\mathrm{SOC}} < 0$) guarantees the launching antenna at Port A excite spin-up waves $\Psi^{\uparrow +/-}$, containing both positive (red arrow) and negative index (purple arrow) modes, toward positive x-direction. One thing to be aware of is the ratio of these two modes is undetermined at this point since the transmitter location is not specified at Port A. For the sake of clarity, the discussion will first focus on the positive-preferred excitation (red double circle in Figure 8.8b) and move onto the case of the other configuration later.

At the common vertex of these domains, there are two other topologically distinct QSH/QVH interfaces. The one extending along the positive x-direction is situated between $\Delta_{\mathrm{SOC}} > 0$ and $\Delta_{\mathrm{P}} > 0$ and hence supports the positive index mode $\Psi^{\uparrow +}$. Similarly, the other interfaces angled 60° from x-axis hosts the negative index mode $\Psi^{\uparrow -}$ at the domain wall between PCs with $\Delta_{\mathrm{SOC}} > 0$ and $\Delta_{\mathrm{p}} < 0$. Upon encountering with this y-shaped junction, the excited TPEW is being sorted into either QSH /QVH interfaces according to its valley DOF and is then picked up by a receiving antenna placed just outside of the platform at Port B or Port C in Figure 8.8a.

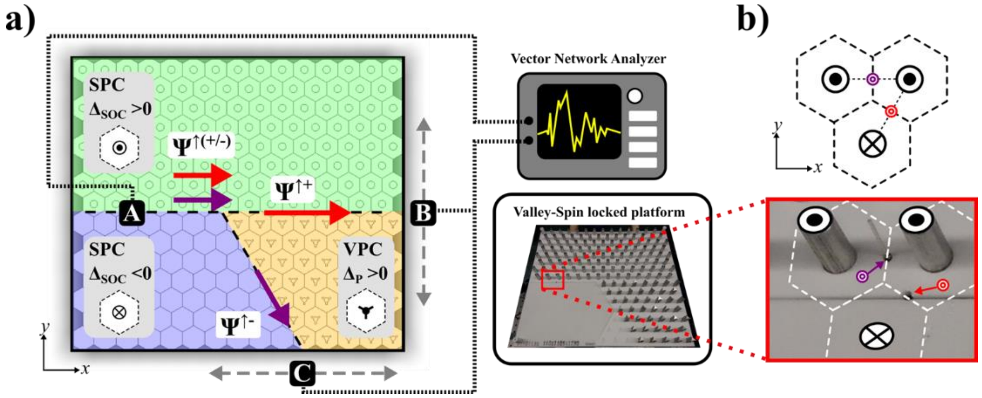

Figure 8.8 Demonstration of valley wave sorting on a valley-spin locked platform. a) Schematic of radio frequency test station. The launching antenna (Port A) sticks into the structure through a drilled hole located a_0 from leftmost edge on the bottom plate. The receiving antenna is mounted on a translation stage to scan along the outer edges of the platform at Port B or Port C. The transmitted signal through channel A-B or A-C is measured by a vector network analyzer. Inset: the fabricated platform with top plate removed to reveal the layout of PCs. b) Schematic and picture of Port A indicating preferential mode excitation using different launching locations. Red double circle: positive-preferred excitation; purple double circle: negative-preferred excitation.

All ports are connected to a vector network analyzer to measure the S-parameters of valleyed-sorted TPEWs through A-B or A-C channel. The receiver at both Port B and C is mounted on a translation stage of the test station. To better observe the energy routing of the platform, the measured $|S_{21}|^2$ of spectrum is double-summed over every location along the scanned path and frequencies points in the spectral range of the photonic bandgap. The resulting transmitted energy through A-B channel (blue stars) and A-C channel (green circles) is plotted in Figure 8.10a and further verifies the excited waves contain more $\Psi^{\uparrow+}$ content using the positive-preferred excitation configuration of Port A. Noting that the purity of excited modes could be easily improved by using an array of phased dipole antennas, but this optimizing process is beyond the scope of this paper.

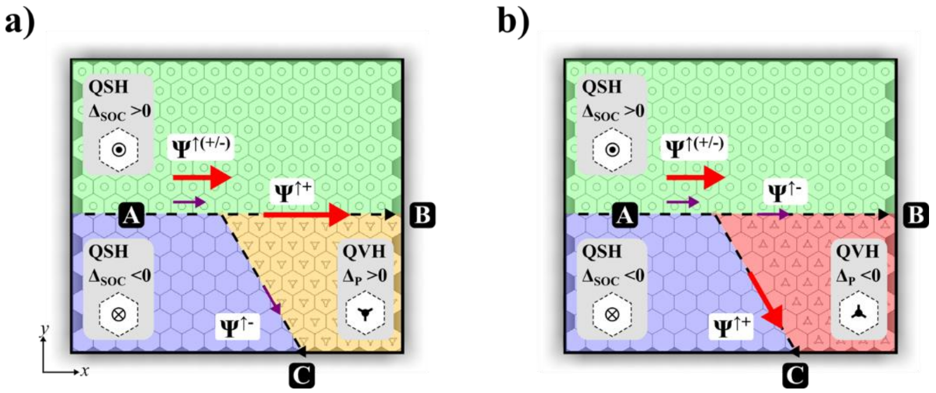
a)
QSH
$\Delta_{SOC}>0$
$\Psi^{\uparrow(+/-)}$
$\Psi^{\uparrow+}$
A
B
QSH
$\Delta_{SOC}<0$
QVH
$\Delta_P>0$
$\Psi^{\uparrow-}$
C
y
x
b)
QSH
$\Delta_{SOC}>0$
$\Psi^{\uparrow(+/-)}$
$\Psi^{\uparrow-}$
A
B
QSH
$\Delta_{SOC}<0$
QVH
$\Delta_P<0$
$\Psi^{\uparrow+}$
C

Figure 8.9 Energy routing of the platform with positive-preferred excitation. Schematic of valley-polarized waves routing a) with QVH PTI at $\theta = 0°$ ($\Delta_p > 0$). b) with QVH PTI at $\theta = 60°$ ($\Delta_p < 0$). Green: QSH PTI with $\Delta_{SOC} > 0$, blue: QSH PTI with $\Delta_{SOC} > 0$, yellow: QVH PTI with $\Delta_P > 0$, red: QVH PTI with $\Delta_P > 0$. Red and purple arrows: positive and negative index waves.

Another novel property of this valley-spin locked platform is the capability to binary-switch the topology of QVH PTIs from $\Delta_p > 0$ to $\Delta_p < 0$ by rotating the tripods from $\theta = 0°$ to $\theta = 60°$ as illustrated in Figure 8.9. In doing so, the supported modes of two channels swapped accordingly due to the distinct topology of QVH PTI domain. In Figure 8.10a, for example, $\Psi^{\uparrow+}$ is previously directed to Port B at $\theta = 0°$ and is now routed to Port C due to the QSH/QVH segment of A-B channel is situated between $\Delta_{SOC} > 0$ and $\Delta_p < 0$ at $\theta = 60°$ and thus suppresses the propagation of the positive index TPEWs (see supplemental information). Likewise, this switching of topology affects the QSH/QVH domain wall of A-C channel as well and eventually two channels interchange the supporting TPEWs modes.

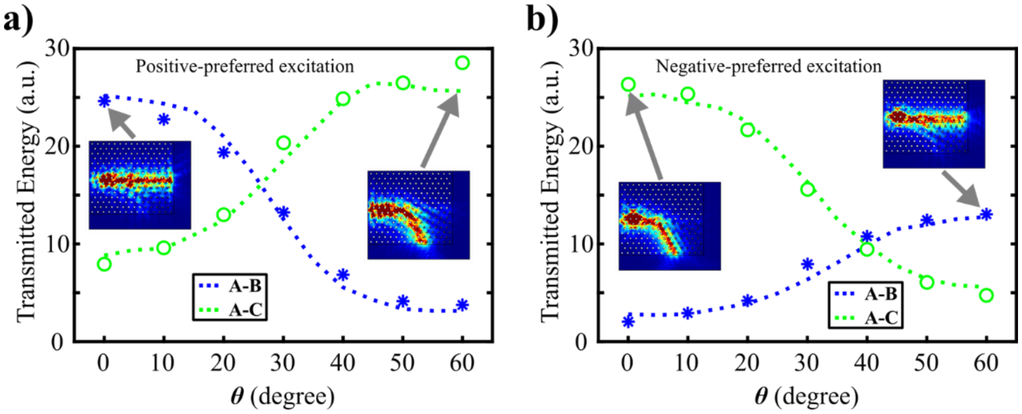

Figure 8.10 Transmission measurements of the valley sorting platform with c) positive-preferred excitation and d) negative-preferred excitation. Blue star (green circle) shows the summation of experimentally measured $|S_{21}|^2$ through A-B (A-C) channel. Numerical simulation of the transmission through A-B (blue dashed curve) and A-C (green dashed curve) channels agrees well to experimental observations. The tripods are rotated gradually from $\theta = 0°$ to $\theta = 60°$ (from $\Delta_P > 0$ to $\Delta_P > 0$) with $10°$ per step. Insets: energy density plots of full-size simulation at $\theta = 0°$ to $\theta = 60°$ showing the energy is in fact routed according to the topology swapping of two QSH/QVH interfaces.

This transition of topology is monitored by gradually rotating tripods from $\theta = 0°$ to $\theta = 60°$ with $10°$ per step. The measured result clearly shows the transmitted signal decreases at Port B and increases at Port C throughout the process. The numerical simulation of this transition of topology (blue and green dashed curves) agrees well to the experimental observation and confirms the signal change is in fact due to energy routing in the insets at $\theta = 0°$ and $\theta = 60°$. The numerical model is simulated at 5 spectral positions spanning evenly from $0.98f_0$ to $1.02f_0$ and the transmitted energy is calculated by integrating $|E_z|^2$ at the exiting surface of Port B and Port C. The resulting value are summed over 5 frequencies inside PBG as a single measure to match the experimental results. Combining above demonstrations, the platform is shown to not only have the capability of valley waves sorting, but also be able to dispatch the TPEWs of specific DOFs to the desired port.

With clear display of platform characteristics with positive-preferred excitation, we now shift the focus to the controlling of mode excitation mentioned in the earlier context by studying the case of negative-preferred excitation. Using a launcher at purple double circle in Figure 8.8b, one can more efficiently excite the negative index mode. In Figure 8.10b, one would expect the launched waves with predominately $\Psi^{\uparrow-}$ mode will be sorted and dispatched in a simply opposite way compared to the wave with majorly $\Psi^{\uparrow+}$ mode. However, an obvious discrepancy happens at A-B channel with lower transmitted energy roughly by a factor of 2. This seemingly abnormal asymmetry could be readily explained by the outcoupling behavior of valley-polarized waves at various terminations in the recent reports.

In short, the valley DOF plays an important role in suppressing the back-scattering from the zigzag termination (A-C channel) of crystals and subsequently granting efficient outcoupling into the ambient environment. In contrast, the arm-chair termination (A-B channel) could reflect TPEWs and deteriorate outcoupling efficiency since the valley DOF is not preserved at the edge of the platform. It is important to also notice a fact that although both $\Psi^{\uparrow+}$ and $\Psi^{\uparrow-}$ suffer from the inefficient outcoupling in A-B channel, the arm-chair termination is more deleterious to the negative index mode than to the positive index mode due to larger impedance mismatch.

8.2.4 Summary and Comment

In conclusion, we have experimentally demonstrated a valley-spin locked platform based on PTIs in radio frequency. Implementing QSH PTIs and QVH PTIs into a single structure enables numerous applications, such as valley waves sorting and polarized waves dispatching, that is impossible to construct from PCs with only one binary DOF. The predicted topological transition of QVH PTIs is observed and later utilized to substantiate valley-polarized energy routing. The crucial role of valley conservation on this platform is directly examined by studying the efficiency of TPEWs outcoupling at crystal termination. With the functionalities of this design firmly established in this study, this design could pave the way toward real world applications based on PTIs. Aside from the down-to-earth interest, this valley-spin platform naturally serves as an ideal test bed for emulating phenomenon in the context between spintronics and valleytronics.

8.3 PTI AS TWO-BEAM ACCELERATOR

8.3.1 Concept of a Two-Beam Accelerator

As mentioned earlier in the Chapter 3, the progress in high energy physics evolves along the ever-increasing energies of the colliding particles which requires longer length of colliders. As the physical sizes of the conventional accelerators grows unacceptably large and the cost skyrockets rapidly, novel accelerator concepts are desired for ultra-high gradient accelerators. It is commonly known that operating the accelerating structure at high frequency could alleviate the pulsed heating and structural breakdown problems of the traditional RF-based metallic accelerators and thus validates the envision of a sub-mm EM wave accelerator. However, the difficulty of fabricating the conventional accelerating structure has proven to be formidable due to precise 3-D machining of the parts. In addition, powerful radiation sources at such short wavelength is also challenging.

One particular instance circumventing these hurdles is the concept of two-beam accelerator (TBA) [58,59], where a low-energy beam generates high-frequency radiation and subsequently powers the acceleration section for the high-energy beam. The modern realization of the TBA concept is embodied by the CLIC project at CERN [60]. One of the key limitations of the CLIC-like TBA concepts is that it utilizes the standard bar-loaded cavity that requires three-dimensional precision machining of at least the same complexity level as the disc-loaded conventional traveling wave structure. The machined accelerating cells then need to be bonded to each other to form the complete accelerating structure [61,62]. Therefore, it is unlikely that the existing accelerating structure geometries can be directly extended to mm and sub-mm waves, as would be highly desirable for achieving accelerating gradients that are much higher than the currently achievable values. Thus, a radical departure from the standard accelerator geometries, would be welcome. An example of one possible alternative that does not require any three-dimensional machining is shown in Chapter 5. This “bed-of-nail” structure has been investigated by us theoretically and experimentally during the previous chapters [36,50,55]. As part of the proposed experimental and theoretical research program, we will investigate its applicability to the TBA concept and experimentally test its properties using high-charge electron bunches that are available at the Argonne Wakefield Accelerator (AWA) facility at the Argonne National Laboratory.

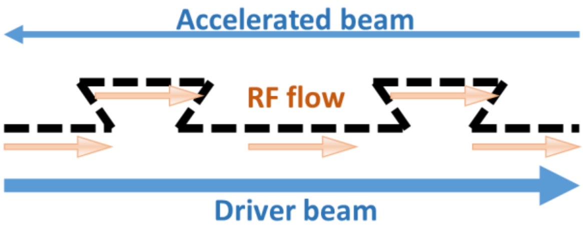

Figure 8.11 Conceptual schematic of a two-beam accelerator (TBA) based on a compact photonic structure that avoids reflections due to topological protection of the interface-guided electromagnetic waves. (a) The concept: a high-current low energy driving beam is slowed down in the lower portion of the accelerating structure, while the low-current high-energy main beam is accelerated in the upper portion of the structure. The power flow between the decelerating and accelerating portions of the structure occurs along the sharply bent interface between two PTIs of the type shown in Figure 5.6b.

For example, a photonic structure shown in Figure 8.11 is composed of two 2 QSH PTIs that do not require any complex machining, don’t need to be brazed (no electrically contacting sidewalls are required for transverse mode confinement), and can be easily assembled. A boundary (domain wall) between two PTIs as the supports TPEWs which can be guided along any the curved or zigzag-like interfacial line because TPEWs are topologically protected against backscattering from any interfacial perturbation. TPEWs are thus very attractive for delivering microwaves to the accelerated beam because they can propagate in any direction, i.e. not necessarily collinearly with the beam. Therefore, one can conceive using PTIs as an integrated platform for (i) microwaves generation by a driver beam in the TBA context, (ii) microwaves delivery to the accelerated beam, and (iii) beam acceleration.

Even more remarkably, one can place the driver and accelerated beam on the same electromagnetic platform as shown in Figure 8.11. Thus, a topological electromagnetic photonic crystal could become a unified platform for both power extraction and transfer structures that removes the kinetic energy of the high-current low-energy driver beam, and the main accelerator that delivers that energy to the high-energy low-current main beam. The most important feature of TPEWs that would be utilized in such a design is that the electromagnetic waves can be phase delayed by turning them around on the scale of less than one vacuum wavelength as exemplified in Chapter 8.1. Therefore, the normally super-luminous accelerating TPEW can be made luminous by providing an extra phase delay to the electromagnetic wave using a series of delay.

The concept of synchronizing the wave with the beam via phase delay is not new: it has been implemented in the form of folded waveguide traveling wave tubes. The important advantage of the topologically protected surface wave is that the actual delay can be made very small due to the ability of TPEWs to make sharp turns without back-reflections. This clearly minimizes the region occupied by the wave where it is not overlapping with the beam. Such minimization of the delay region reduces the stored energy per unit length of the accelerator and, therefore, increases the of the structure. Additionally, the rapid change of the electromagnetic environment experienced by an electron bunch near the bend increases the emission of radiation into a TPEW. This emission is conceptually equivalent to transition radiation of an electron that moves from one medium to another. In this case, such transition radiation is beneficial because it serves as a mechanism for converting the kinetic energy of the driver beam into radiation.

Moreover, by designing the structures in such a way as to ensure that both the driving beam and the accelerated beam are simultaneously synchronous with the TPEWs, we can envision ultra-compact two-beam accelerators that can be scaled down to very short wavelengths (e.g., to mm-wave dimensions). Of course, a TBA is not the only concept that can benefit from a topologically-protected electromagnetic structure. Because of the super-luminous nature of the TPEWs, it is also possible to couple the electromagnetic energy into the structure by simply opening the entrance holes into the structure. Such far-field coupling has significant advantages at short wavelength because high Ohmic losses make conventional waveguide unacceptable at mm-wave frequencies.

8.3.2 Transition Radiation in Photonic Bandgap

The main focus of this section is to study the feasibility of using a transition radiation for the short-wavelength EM waves source on the QSH PTI platform. Thanks to the topological protection, the resulting radiation could be routed away from driver beam without suffering loss and then precisely phase delayed for matching the accelerated beam. Particularly, this transition radiation generated by a relativistic charged particle passing through a topological interface, namely a domain wall between QSH/QSH ($\Delta_{\mathrm{SOC}}> 0, \Delta_{\mathrm{SOC}}< 0$), posts a fundamental question: can a charged particle generate transition radiation at the interface between two very similar media which only differ in topology? To better answer this question, a semi-analytical method has been developed by a colleague, Yang Yu, to integrate analytical modeling and numerical simulation together and provide a physical insight of the transition radiation at such topological interface. This section is a short summary of the said model at the courtesy of Yang Yu for the sake of completeness. Readers of interest are advised to check the future publication for the rigorous derivation and details of numerical simulations.

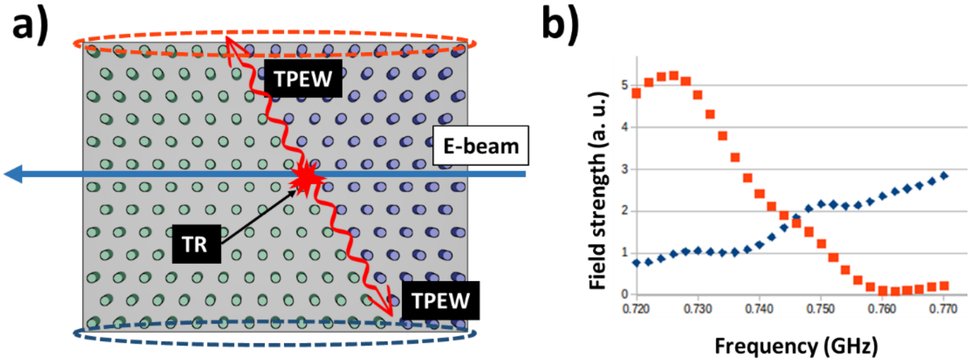

Figure 8.12 Simulated results of transition radiation in a PBG. a) The layout of the PTI accelerating platform with a straight interface between $\Delta_{SOC} > 0$ (green) and $\Delta_{SOC} < 0$ (purple) domains of PCs. b) Calculated result of radiated power with semi-analytical model. Orange (blue) scatters: TPEWs power integrated over the top (bottom) edge of the structure as shown in a).

Inspired by the classic textbook [63] together with the transition radiation in photonic crystal [64] and the recent development of Bloch mode expansion in photonic crystals [65], this model is an analytical model implemented with numerical calculation of first principal simulation. The gist of the derivation is following: the transition radiation is accounted by the Bloch modes expansion in PCs with the modes determined by the eigenfrequency simulation in COMSOL. The simulation domain is chosen to be the same as the supercell simulation in the proceeding chapters, namely a QSH/QSH interface with 15 PCs on each side whereas as the incident particle is propagating along the boundary of this domain. Then an overlapped integral between the mode profile of the resulting propagating mode and the charged particle propagation is numerically calculated and summed together to give out the transition radiation at the topological interface. A separate driven model from COMSOL is constructed and simulated to verify the prediction of the developed method.

As a result, the calculated spectrum using the semi-analytical model agrees well to the numerical result from the driven simulation of the same geometry as shown in Figure 8.12. Note that the results are calculated with normalized frequency without any scaling factor. The geometric parameters of realistic platform will be determined in the next section with specific constraints and physical requirements.

8.3.3 Toward Experimental Realization

To be used as a TBA and tested at the AWA in ANL, it is important to choose the operating frequency of the platform to be high harmonics of the repetition rate of the electron beam of the LINAC in the facility. Equally crucial are enough egress for high-current driver beam to propagate through without losing huge charges and also enough number of crystals on the platform to substantiate the standing ground of Bloch wave. The evaluating process is briefly summarized below.

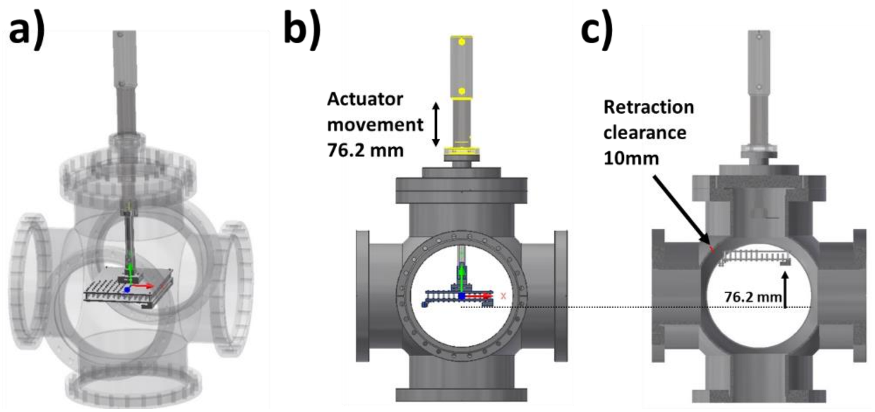

Figure 8.13 Drawings of 6-way cross vacuum chamber with in AWA. This chamber designated to be used for testing the transition radiation on PTI platform. a) Orientation of the accelerating structure in the chamber. The chamber is rendered transparent to show how the structure (indicated by the origin) is fixed to the actuator on the top flange. b) The drawing showing the actuator retraction of the 3-inch (76.2mm) distance of travel. The electron beam is passing through the center of the chamber (concentric to the PTI structure). c) The 10mm secure clearance between structure and the wall of chamber after the actuator fully retracted. Half of the chamber is removed to show the clearance.

Among all the requirements, the strictest limitation is the physical size of the experiment chamber. The designated chamber is the 6-way cross chamber with 10-inch diameter ports. In order to fabricate the sample with material other than oxygen-free high-conductivity copper, the vacuum of the chamber is secured by a Beryllium window at the entrance of the chamber at the expense of the increased emittance of the electron beam. To meet the vacuum requirement in the chamber, the material of sample fabrication is again chosen to be aluminum 6061 due to the cost-effective price.

	Value
Diameter of rod (d)	3.97 mm
Height of rod (h)	9.78 mm
Periodicity of lattice (a)	11.5 mm
Operating frequency	19.47 GHz
Wavelength	15.4 mm
Sample aperture	11.5 mm × 6mm

Table 8.1 Dimensions of QSH PTI platform unit cells as a TBA.

The accelerating structure will be mounted to a fixture extension from an actuator from the top flange as shown in Figure 8.13a. The actuator can be inserted and retracted from the chamber with 3-inch distance of travel. The upper-bound of the sample size is limited by this physical factor for avoiding the collision between the structure and the chamber as indicated in Figure 8.13c. After taking these trade-offs into account, we finalize the scaling factor and the resulting diameter of rods is: $\mathrm{d} = 5/32\,'' = 3.97\mathrm{mm}$, which is close to the 15th harmonics of the $1.3\mathrm{GHz}$ with 2% of detuning in frequency. The geometric parameters are summarized in the Table 8.1.

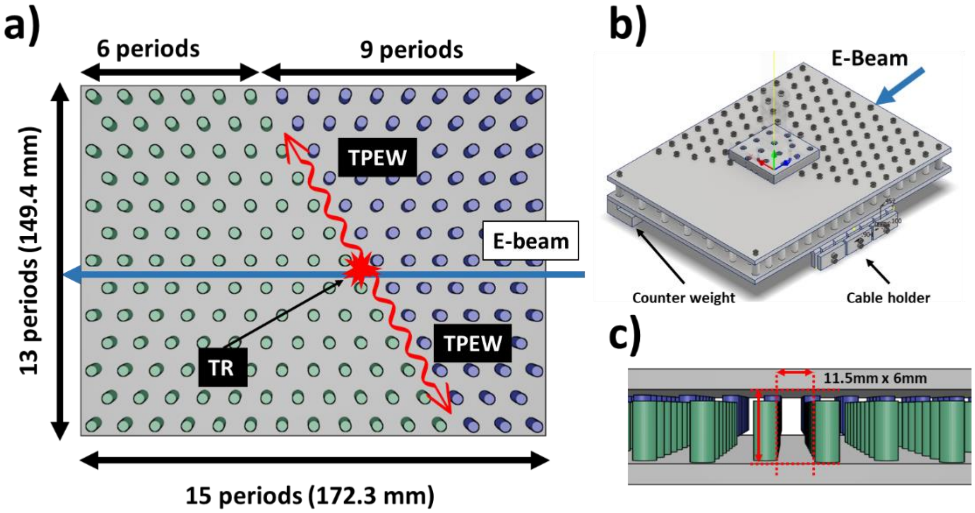

Figure 8.14 Schematic drawing of QSH PTI platform. a) The layout and the geometric parameters of the platform for testing transition radiation in PBG. Purple: rods attached to top plate, green: rods attached to bottom plate, blue arrow: electron beam, red arrow: TPEWs. b) The orientation of the assembled PTI accelerating structure with cable holder and counter weight. c) The aperture of the sample for electrons passage.

Working with finalized dimensions above, the proposed platform in the first experiment run in AWA is arranged as the same as the structure studied in Chapter 8.2 so that the theoretical predictions can be verified directly before moving forward to the realization of the TBA using QSH PTI. In Figure 8.14a, the layout consists of 15×13 photonic crystals with a straight topological interface in diagonal direction separating two domains of QSH with opposite topologies ($\Delta_{SOC} > 0, \Delta_{SOC} < 0$). The electron beam will pass through the structure along the longer axis of the structure and therefore posse an oblique incident to the domain wall (30° from the normal). The excited TPEWs exits the structure along the interface and then picked out by the loop antenna mounted on the cable holder on the outside of the structure. Four antennas are deployed to measure the EM radiation from the passage of electron bunch. Three of them are positioned at the topological interface while the last one is placed further away to show the contrast of spatial confinement of the TPEWs.

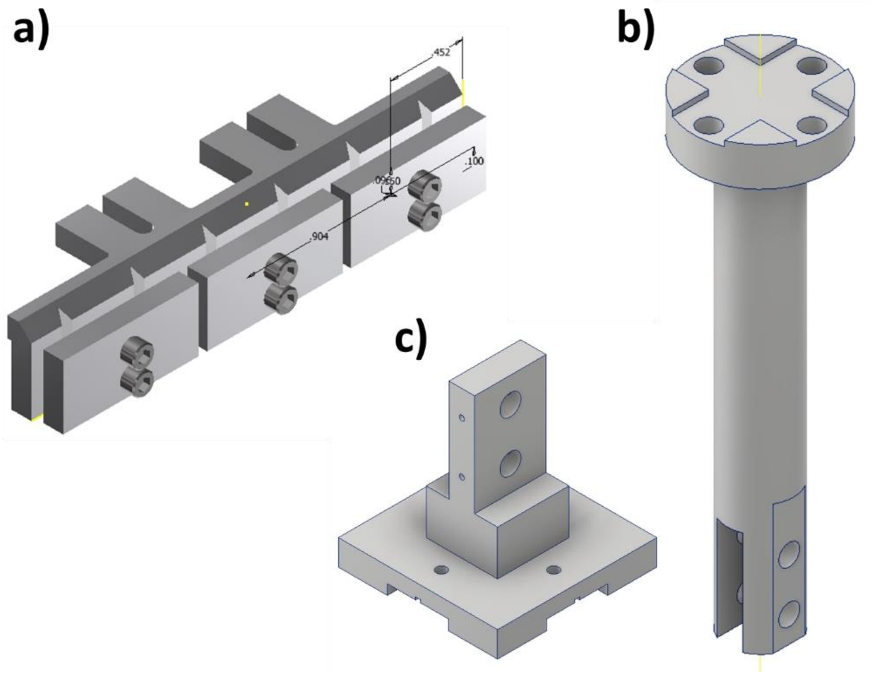

Figure 8.15 Technical drawings of fixture parts. a) Cable holder. b) Fixture extension. c) Fixture joint. Note that the sketches are not to the real scale.

One important designing factor, as advised by AWA staffs, is to balance the structure assembly so that the assembly exerts no torque to the actuator during the insert/retraction movement which might cause malfunctioning of the actuator or smash the structure into the chamber wall due to the tilted orientation. To meet this requirement and to keep the beam passing through the aperture at the same time, a counter weight is included in the assembly as shown in the Figure 8.14b. Although the weight of this counter weight is calculated by CAD software during design phase, the actual overshoots the designed weight to account for the overall fabrication imperfection. This way, the assembly can maintain in balance by shredding off the counter weight whereas adding weigh to the structure is difficult in this context.

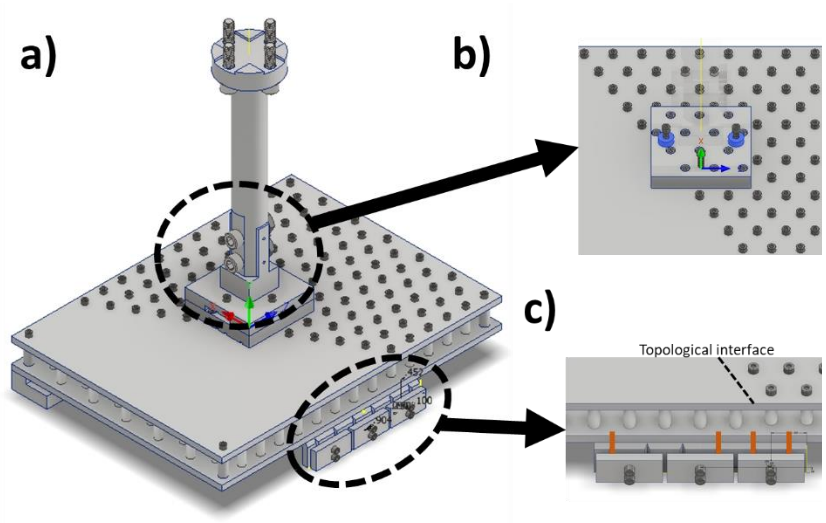

Figure 8.16 Schematic of parts assembling. a) fully-assembled PTI accelerating structure with fixture to the actuator. b) washers (highlighted blue) for tweaking the pitch alignment. c) probes held by the cable holder. Orange: loop antennas.

In Figure 8.15, a fixture joint designed to tweak the angular direction of the structure is composed of two pieces of parts that separated by several washers to align the channel to the beam axis. The pitch could be tuned $\pm 24\,\mathrm{mrad}$ by changing washer of various thickness as described in Figure 8.16b. Moreover, a long fixture extension, which could reduce the difficulty of directly accessing to the actuator, is included to bridge between the actuator and the fixture joint. Note that to eliminate the possible air pockets and thus speed up the chamber pumping, we choose vented screws as fasteners and add several trenches to the contacting surface to open up blind holes.

The parts are fabricated using different methods depending on the required precision and difficulty of the machining to reduce the cost and shorten the lead time. The top and bottom plates together with the fixture plate in Figure 8.16b are made by using water jet cutting since the features are all through holes. The fixture extension and fixture joint are relatively complicated and involve extra turning as well as milling process. Furthermore, these two parts are designed to mate to each other which requires high precision on both sides. Therefore, these two pieces are outsourced from the professional machine shop at LASSP in Cornell. On the other hand, the cable holder and counter weight pieces are manually machined by the author. Figure 8.17 shows the fabricated and fully assembled PTI accelerating structure hanged from the fixture joint by a twist-tie wire to show the well-balanced weight distribution.

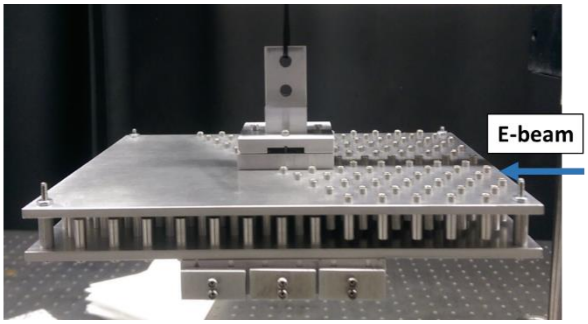

Figure 8.17 Fabricated PTI accelerating structure. The balance of is checked by hanging the assembly mid-air with a twist-tie wire (black wire in the through hole). Note that the fixture extension piece is neglected in this balance test since it is symmetric to the actuator axis thus it doesn’t shift the center of gravity.

After the confirming the sample is fabricated as designed and also weight balanced, the whole assembly is then dismantled into pieces and sent to Argonne National Laboratory for surface cleaning to meet the vacuum requirement of the facility. While preparing this thesis, the author has not received the confirmed schedule for the on-site experiment at AWA in ANL, but the hot test is expected to be carried out once the time slot is allocated.

8.3.4 Summary and Comment

To sum up, the topological structures will be selected for future collider applications based on the following criteria: (i) ease of fabrication and the possibility of scaling down to millimeter and sub-millimeter frequency ranges, (ii) the ability to propagate the beam through the structure without major obstructions, and (iii) the promise of these structures for developing two-beam accelerators capable of withstanding high peak microwave power without suffering from structural breakdown due to pulsed heating. The lack of cross-talk between individual delay structures due to topological protection against backscattering makes the investigation of topological accelerators highly desirable regardless whether they are driven by a second beam (the TBA configuration) or by an external power source.

Chapter 9 Summary and Outlook

9.1 DISSERTATION SUMMARY OF SCIENTIFIC RESULTS

This chapter summarizes the main scientific results of the proceeding chapters and wraps up the thesis with remarks and outlooks. Furthermore, several potential directions of the relevant projects are outlined for future researchers' information.

In Chapter 2 and 3, a specific application of surface wave, surface wave accelerator based on silicon carbide (SWABSiC), is proposed based on its all-dielectric design and commercially available high-power CO_2 laser. And a new method of exciting surface wave on the polar/non-polar interface with density modulated electron beam is used in the hot tests in Accelerator Test Facility in Brookhaven National Laboratory. The results deviates from the numerical simulation which is largely due to the wasuggests a future improvement of switching the wavelength of the CO_2 laser.

Chapter 4, 5, 6, 7, and 8 cover a recently emerging field in photonic system, namely the topological photonics. Particularly, a specific design of PTI is investigated in the RF region. In Chapter 5, the TPEWs on the QSH PTI platform are investigated. The designing principles, sample fabrication, and instrumentation are provided in detail. The property of the robust and defect-immune wave transport is exhibited by comparing to EM wave on a topologically trivial system. In Chapter 6, the TPEWs on the QVN PTI platform are demonstrated to be robust and defect-immune using the similar arguments in Chapter 5. In addition, the topologically protected out-coupling refraction of the QVH PTI is demonstrated by spatially scanned transmission measurements. In Chapter 7, a simple methodology of preferential mode excitation is exhibited to provide high mode purity to both QSH PTI and QVN PTI platforms. In Chapter 8, three application examples based on TPEWs on the PTI platforms have been proposed and demonstrated theoretically as well as experimentally. First, a compact broadband RF delay line is realized on the QSH PTI platform which is shown to suppress cross-talking between components thanks to the topological protection of the TPEWs wave transport. Second, a hybrid platform implements two independent binary DOFs (spin and valley) is exhibited to sort the TPEWs according to their valley-polarization. In addition, a method of preferential mode excitation using a simple linear dipole antenna is also presented. Third, the platform of QSH PTI is conceived as a two-beam accelerator. The feasibility of using transition radiation of electron passing through a topological interface is verified by semi-analytical model. The process of sample design and fabrication of parts are covered.

9.2 OUTLOOK FOR FUTURE RESEARCH

The outlook of the SWABSiC largely depends on the wavelength switching of the CO_2 laser at ATF. With the correct source of excitation, the performance of the SWABSiC is expected to eliminate the discrepancy between numerical simulation and experimental outcomes. Also, the direct laser excitation of the SPhPs on silicon carbide with silicon prism as substrate is another possibility although the space in the chamber is extremely restrictive for necessary IR optical components, such as a normal copper mirror, a holed mirror, a parabolic mirror. In addition, a Germanium plate must be included on sample stage in order to perform electron-laser synchronization because the optical path is different for laser pulse and electron bunch in this excitation scheme.

In the context of the topological photonics, the existing platform in this dissertation is predicted to support another DOF which emulating quantum Hall effect, therefore QH PTI. Experimental realization of combining all three DOFs on a single platform is envisioned to substantiate many more functionalities beyond what has been covered Chapter 8. Future experiment is schedule to be conducted in the AWA facility in Argonne National Laboratory which could provide verification to the semi-analytical model and pave the way to realizing the PTI TBA. Following the development of the field of metamaterials, it is natural to scale down the operating frequency to infrared (IR) for telecommunication or even visible region. Aside from the specific system investigated in this thesis, one can engineer topological phase on the photonic system made of dielectric. Departing from the linear region, it is desired to explore the nonlinear photon-photon and photon-matter interaction on a topological platform. Other direction including the so-called "topolaritons" which are topological polaritonic excitation from strong light-matter interaction. Overall, this field is still in its infancy phase and thus granting enormous possibility to be explored.

References

1. Ritchie, R. H., Plasma Losses by Fast Electrons in Thin Films. *Phys. Rev.* **106**, 874 (1957).
2. Pines, D. & Bohm, D., A Collective Description of Electron Interactions: II. Collective vs Individual Particle Aspects of the Interactions. *Phys. Rev.* **85**, 338 (1952).
3. Pines, D., Collective Energy Losses in Solids. *Rev. Mod. Phys.* **28**, 184 (1956).
4. Ruthemann, G. 1. A. P. . L. 2. 1., Diskrete Energieverluste mittelschneller Elektronen beim Durchgang durch dünne Folien. *Annalen der Physik* **437**, 113 (1948).
5. Joannopoulos, J. D., Steven, G. J., Winn, J. N. & Meade, R. D., *Photonic Crystals: Molding the Flow of Light* (Princeton University Press, 2008).
6. Zenneck, J., Über die Fortpflanzung ebener elektromagnetischer Wellen längs einer ebenen Leiterfläche und ihre Beziehung zur drahtlosen Telegraphie. *Ann. Physik* **4** (23), 846 (1907).
7. Norton, K. A., Propagation of Radio Waves Over a Plane Earth. *Nature*, 934-935 (1935).
8. D'yakonov, M. I., Newtype of electromagneticwave propagatingat an interface. *Zh. Eksp. Teor. Fiz.* **94**, 119-123 (1988).
9. Takayama, O., Crasovan, L., Artigas, D. & Torner, L., Observation of Dyakonov Surface Waves. *Phys. Rev. Lett. 102* **102**, 043903 (2009).
10. Engheta, N. & Pelet, P., Surface waves in chiral layers. *Optics Letters* **16** (10), 723-725 (1991).
11. Shadrivov, I. V. *et al.*, Nonlinear surface waves in left-handed materials. *Phys. Rev. E 69* **69**, 016617 (2004).
12. Mihalache, D., Bertolotti, M. & Sibilia, C., IV Nonlinear Wave Propagation in Planar Structures. *Progress in Optics* **27**, 227-313 (1989).
13. Prade, B., Vinet, J. Y. & Mysyrowicz, A., Guided optical waves in planar heterostructures with negative dielectric constant. *Phys. Rev. B* **44**, 13556 (1991).
14. Shvets, G., Photonic Approach to Making a Surface Wave Accelerator. *AIP Conference Proceedings* **647**, 371 (2002).
15. Neuner, B., Korobkin, D., Ferro, G. & Shvets, G., Prism-coupled surface wave accelerator based on silicon carbide. *Phys. Rev. ST Accel. Beams* **15**, 031302 (2012).
16. Palik, E. D., *Handbook of optical constants of solids* (Academic Press, 1998).
17. Wang, T., Lai, K., Khudik, V. N. & Shvets, G., Cherenkov radiation in a surface wave accelerator based on silicon carbide (SWABSiC). *AIP Conference Proceedings* **1812**, 070004 (2017).

18. Cherenkov, P. A., Visible emission of clean liquids by action of γ radiation. *Dokl. Akad. Nauk SSSR* **2**, 451 (1934).
19. Vavilov, S. I., O vozmozhnykh prichinakh sinego γ-svecheniya zhidkostei. *Dokl. Akad. Nauk SSSR* **2**, 457 (1934).
20. Frank, I. & Tamm, I., Coherent visible radiation of fast electrons passing through matter. *C. R. Acad. Sci. USSR* **14**, 109 (1937).
21. Duris, J. *et al.*, High-quality electron beams from a helical inverse free-electron laser accelerator. *Nat. Comm.* **5**, 4928 (2014).
22. Sudar, N. *et al.*, High Efficiency Energy Extraction from a Relativistic Electron Beam in a Strongly Tapered Undulator. *Phys. Rev. Lett.* **117**, 174801 (2016).
23. Sudar, N. *et al.*, Demonstration of Cascaded Modulator-Chicane Microbunching of a Relativistic Electron Beam. *Phys. Rev. Lett.* **120**, 114802 (2018).
24. Fedurin, M., Babzien, M. & Yakimenko, V., GENERATION AND CHARACTERIZATION OF 5-MICRON ELECTRON BEAM FOR PROBING OPTICAL SCALE STRUCTURES. *Proceedings of IPAC2012* (2012).
25. Kavokin, A. V., Shelykh, I. A. & Malpuech, G., Lossless interface modes at the boundary between two periodic dielectric structures. *Phys. Rev. B* **72**, 233102 (2005).
26. Tamm, I., Über eine mögliche Art der Elektronenbindung an Kristalloberflächen. *Z. Physik* **76**, 849 (1932).
27. Thouless, D. J., Kohmoto, M., Nightingale, M. P. & Nijs, M. D., Quantized Hall Conductance in a Two-Dimensional Periodic Potential. *Phys. Rev. Lett.* **49**, 405 (1982).
28. Klitzing, K. v., Dorda, G. & Pepper, M., New Method for High-Accuracy Determination of the Fine-Structure Constant Based on Quantized Hall Resistance. *Physical Review Letters* **45** (6), 494 (1980).
29. Bernevig, B. A., Hughes, T. L. & Zhang, S.-C., Quantum spin Hall effect and topological phase transition in HgTe quantum wells. *Science* **314**, 1757--1761 (2006).
30. Bernevig, B. A. & Zhang, S.-C., Quantum Spin Hall Effect. *Phys. Rev. Lett.* **96**, 106802 (2006).
31. Aoki, H. & Ando, T., Effect of localization on the hall conductivity in the two-dimensional system in strong magnetic fields. *Solid State Communications* **38** (11), 1079 (1981).
32. Kane, C. L. & Mele, E. J., Quantum Spin Hall Effect in Graphene. *Physical Review Letters* **95**, 226801 (2005).
33. Hsieh, D. *et al.*, A topological Dirac insulator in a quantum spin Hall phase. *Nature* **452** (7190), 970-974 (2008).

34. König, M. *et al.*, Quantum spin Hall insulator state in HgTe quantum wells. *Science* **318** (5851), 766-770 (2007).
35. Khanikaev, A. B. *et al.*, Photonic topological insulators. *Nature Materials* **12** (3), 233-239 (2013).
36. Ma, T., Khanikaev, A. B., Mousavi, S. H. & Shvets, G., Guiding Electromagnetic Waves around Sharp Corners: Topologically Protected Photonic Transport in Metawaveguides. *Physical Review Letters* **114** (12), 127401 (2015).
37. Ma, T. & Shvets, G., Scattering-free edge states between heterogeneous photonic topological insulators. *Physical Review B* **95** (16), 165102 (2017).
38. Peleg, O. *et al.*, Conical Diffraction and Gap Solitons in Honeycomb Photonic Lattices. *Phys. Rev. Lett.* **98**, 103901 (2007).
39. Sepkhanov, R. A., Bazaliy, Y. B. & Beenakker, C. W. J., Extremal transmission at the Dirac point of a photonic band structure. *Phys. Rev. A* **75**, 063813 (2007).
40. Sakoda, K., *Optical Properties of Photonic Crystals* (Springer, Berlin, 2001).
41. Slater, J. C., Microwave Electronics. *Rev. Mod. Phys.* **18**, 441 (1946).
42. Raghu, S. & Haldane, F., Analogs of quantum-Hall-effect edge states in photonic crystals. *Physical Review A* **78** (3), 033834 (2008).
43. Wang, Z. & Fan, S., Optical circulators in two-dimensional magneto-optical photonic crystals. *Opt. Lett.* **30**, 1989 (2005).
44. Qiu, W., Wang, Z. & Soljačić, M., Broadband circulators based on directional coupling of one-way waveguides. *Opt. Express* **19**, 22248 (2011).
45. Wallace, J. W. & Jensen, M. A., Mutual Coupling in MIMO Wireless Systems: A Rigorous Network Theory Analysis. *IEEE TRANSACTIONS ON WIRELESS COMMUNICATIONS* **3**, 1317 (2004).
46. Xia, F., Sekaric, L. & Vlasov, Y. *Nature Photonics* **1**, 65 (2007).
47. Bogaerts, W. *et al.*, Silicon microring resonators. *Laser Photonics Rev.* **1**, 47 (2012).
48. Hafezi, M., Mittal, S., Fan, J., Migdall, A. & Taylor, J. M., Imaging topological edge states in silicon photonics. *Nature Photonics* **7**, 1001–1005 (2013).
49. Mittal, S. *et al.*, Topologically Robust Transport of Photons in a Synthetic Gauge Field. *Physical Review Letters* **113**, 087403 (2014).
50. Lai, K., Ma, T., Bo, X., Anlage, S. & Shvets, G., Experimental Realization of a Reflections-Free Compact Delay Line Based on a Photonic Topological Insulator. *Scientific Reports* **6**, 28453 (2016).
51. Ma, T. & Shvets, G., All-Si valley-Hall photonic topological insulator. *New Journal of Physics* **18** (2), 025012 (2016).
52. Gao, F. *et al.*, Topologically protected refraction of robust kink states in valley photonic crystals. *Nat. Phys.* **14**, 140-144 (2018).

53. Xiao, D., Yao, W. & Niu, Q., Valley-Contrasting Physics in Graphene: Magnetic Moment and Topological Transport. *Physical Review Letters* **99** (23), 236809 (2007).
54. Mong, R. S. K. & Shivamoggi, V., Edge states and the bulk-boundary correspondence in Dirac Hamiltonians. *Phys. Rev. B 83* **83**, 125109 (2011).
55. Xiao, B. *et al.*, Exciting reflectionless unidirectional edge modes in a reciprocal photonic topological insulator medium. *Phys. Rev. B* **94**, 195427 (2016).
56. Ye, L., Yang, Y., Hang, Z. H., Qiu, C. & Liu, Z., Observation of valley-selective microwave transport in photonic crystals. *Appl. Phys. Lett.* **111**, 251107 (2017).
57. Chabanov, A. A. & Genack, A. Z., Statistics of Dynamics of Localized Waves. *Phys. Rev. Lett.* **87**, 233903 (2001).
58. Sessler, A. M. & Yu, S. S., Relativistic klystron two-beam accelerator. *Phys. Rev. Lett.* **58**, 2439 (1987).
59. Kazakov, S. Y., Kuzikov, S. V., Jiang, Y. & Hirshfield, J. L., High-gradient two-beam accelerator structure. *Phys. Rev. ST Accel. Beams* **13**, 071303 (2010).
60. Aicheler, M. *et al.*, *A Multi-TeV Linear Collider Based on CLIC Technology* (CERN, Geneva, 2012).
61. Elmer, J. W., Klingmann, J. & Van Bibber, K., Diffusion bonding and brazing of high purity copper for linear collider accelerator structures. *Phys. Rev. ST Accel. Beams* **4**, 053502 (2001).
62. Wang, J. W. *et al.*, Fabrication Technologies of the High Gradient Accelerator Structures at 100MV/m Range. *SLAC-PUB-15146* (2012).
63. Ginzburg, V. L. & T͡Sytovich, V. N., *Transition radiation and transition scattering* (CRC Press, 1990).
64. Luo, C., Ibanescu, M., Johnson, S. G. & Joannopoulos, J. D., Cerenkov Radiation in Photonic Crystals. *Science* **299** (5605), 368-371 (2003).
65. Kremers, C., Chigrin, D. N. & J., K., Theory of Cherenkov radiation in periodic dielectric media: Emission spectrum. *Phys. Rev. A* **79**, 013829 (2009).
66. Boardman, A., King, N., Rapoport, Y. V. & L., Gyrotropic impact upon negatively refracting surfaces. *New J. of Phys.* **7**, 191 (2005).

Vita

Kueifu Lai was born and raised in Taipei, Taiwan. He is the second son of Chin-Yi Lai and Jui-Shiang Kuo. He stayed in his hometown until graduation from the Taipei Municipal Jianguo High School. He chose physics as his undergraduate major in the National Tsing Hua University in HsinChu and studied electromagnetic experiments as his topic of master thesis under the guidance of Professor Din-Ping Tsai in National Taiwan University in Taipei. He attended SUNY Stony Brook University in New York for his M. A. degree. He started his Ph. D. under the guidance of Professor Gennady Shvets at The University of Texas at Austin in August 2011. During his time in Austin, he met his wife Chia-Lin Chou.

Permanent address (or email): kueifulai@utexas.edu

This dissertation was typed by the author.